Electronic Thesis and Dissertation Repository

9-15-2017 1:30 PM

Time-lapse Electrical Resistivity Tomography for mapping in situ smouldering remediation (STAR)

Lais Muchatte Trento, *The University of Western Ontario*

Supervisor: Dr. Jason Gerhard, *The University of Western Ontario*
Co-Supervisor: Dr. Panagiotis Tsourlos, *The University of Western Ontario*
A thesis submitted in partial fulfillment of the requirements for the Master of Engineering
Science degree in Civil and Environmental Engineering
© Lais Muchatte Trento 2017

Follow this and additional works at: https://ir.lib.uwo.ca/etd

Part of the Environmental Engineering Commons

Abstract

Time-lapse Electrical Resistivity Tomography (ERT), a surface geophysical technique, was applied for the first time to monitor the first full-scale application of Self-sustaining Treatment for Active Remediation (STAR) at a coal tar contaminated site. STAR is a self-sustaining smouldering technology that destroys contaminants in situ by combustion, generating heat, water, and combustion gases. ERT is used as a complementary source of information to support conventional temperature and gas concentration data collected during STAR operations. A shallow (2.4 mbgs) and a deep (7.8 mbgs) treatment cell were monitored, with 2D surface resistivity surveys conducted before, during and after treatment. Two 36 electrodes lines were installed in each cell, with 21 meters of extension in the shallow and 42 meters in the deep cell. In the shallow cell, ERT identified a specific electrical resistivity signal based on temperature and water saturation changes to map the suspected coal tar treatment zones. In both cells, air/gas distribution was observed, as was the capture zone of the vapor extraction system and the re-infiltration of groundwater after treatment. The average subsurface resistivity presented the same trends as other measures of treatment, such as the total amount of combustion gases collected. Overall, the resistivity surveys provided continuous mapping of the subsurface, and showed that ERT is promising for evaluating thermal remediation field applications such as in situ STAR. This study represents the first time that in situ DNAPL remediation was mapped with ERT.

Keywords

Co-Authorship Statement

This thesis was written in accordance with regulations and guidelines for integrated-article format by the Faculty of Graduate and Postdoctoral Studies at the University of Western Ontario. All data was collected, analyzed and interpreted by the candidate under the supervision and guidance of Dr. Jason I. Gerhard and co-supervision of Dr. Panagiotis Tsourlos.

Chapter 3: Time-lapse Electrical Resistivity Tomography for mapping in situ smouldering remediation (STAR)

By Laís M. Trento, Jason I. Gerhard, Panagiotis Tsourlos

Contributions:

Laís M. Trento:	planned and conducted laboratory and field experiments, analysis and interpretation of results, and wrote the draft chapter.
Jason I. Gerhard:	initiated the research topic, assisted in design and supervised field experiments, assisted in data interpretation, and reviewed the draft chapter.
Panagiotis Tsourlos:	assisted in design, data collection and interpretation of laboratory and field experiments, and reviewed the draft chapter.

Acknowledgments

Table of Contents

List of Tables

List of Figures

Chapter 1

1. Introduction

1.1. Problem overview

DNAPLs (dense non-aqueous phase liquids) are contaminants denser than water, such as coal tar, creosote, PCBs (polychlorinated biphenyl), and chlorinated solvents, that migrate below the water table and are considered recalcitrant sources of soil and groundwater contamination presenting risks to human health and the environment (Gaylor et al., 2000; Gerhard et al., 2007; Kueper & Davies, 2009; Kueper et al., 2014). In situ remediation technologies (i.e., bioremediation, chemical oxidation, pumping and treat, thermal desorption) that destroy, mobilize or degrade contaminants have been used to remove DNAPLs source zones, but treatments revealed technical, economical and sustainable challenges; particularly with coal tar, as it is not easily degradable and requires high energy input for mobilization of heavier compounds within the coal tar mixture (Kueper & Davies, 2009). Recently, an innovative smouldering remediation called Self-sustaining Treatment for Active Remediation (STAR) has been tested in situ to destroy coal tar, as well as other DNAPLs (Pironi et al., 2009; Switzer et al., 2009).

Smoldering combustion is a moving oxidation reaction that is oxidant-limited, flameless and exothermic (400-1200 °C). Smouldering occurs in the surface of contaminants within a porous medium, controlled by oxygen, heat losses and fuel concentration (Pironi et al., 2009; Switzer et al., 2009; Pironi et al., 2011). A full-scale STAR system was implemented at an industry site contaminated with coal tar. The operation consists of injecting hot air (> 500°C) to initiate the reaction (Scholes et al., 2015). Once ignited, the heat source is tuned off, while maintaining air injection. With oxidant injection (i.e., oxygen in air) and initial energy input, the oxidation burns the contaminants as fuel generating heat, water and combustion gases (CO_2 and CO) (Scholes et al., 2015). Heat produced by the reaction is transferred and sustained through the porous medium, propagating the front of reaction (Pironi et al., 2011). Treated areas grow with the moving propagation front and are considered clean and dry due to high temperatures

(Scholes et al., 2015). Once the reaction terminates and air stops being injected, groundwater re-infiltrates into the treated zone.

In situ STAR is monitored through: (i) temperature data to identify ignition of the smouldering reaction, (ii) captured combustion gases concentration, and (iii) pre- and post-treatment coring (Scholes et al., 2015). Although comprehensive data collection was acquired during laboratory experiments (Pironi et al., 2009; Switzer et al., 2009; Pironi et al., 2011) and pilot scale (Scholes et al., 2015), a limited number of data points is collected when translated to the field scale. These data are collected intrusively and are sparse and discrete both in space and time, and cannot detect the spatial extent of the treated zone, the extent or propagation of air injected in the subsurface, nor the movement of water and contaminants in response to air injected. Complementary monitoring methods, such as geophysical methods, can provide non-intrusive and spatially continuous information that supports monitoring remediation.

A geoelectrical method, Electrical Resistivity Tomography (ERT), has been broadly used in environmental and hydrogeological characterization (e.g., Lekmine et al., 2017), for its response to groundwater and geological properties (i.e., salinity, water saturation, temperature and porosity) (Samouëlian et al., 2005). Recently, with developments in data collection and interpretation, time-lapse ERT has also been used for remediation monitoring, as it can distinguish the geological background and static interferences from the changes happening in the subsurface due to remedial activities, even though interpretations are non-unique. Time-lapse ERT has been used, for example, in bioremediation (e.g., Johnson et al., 2015) and in situ chemical oxidation (e.g., Mao et al., 2015). Its use in DNAPL thermal remediation is limited and focused on groundwater plume treatment (Newmark et al. 1994; Ramirez et al., 1993; LaBrecque et al., 1996), However, ERT exhibits potential to monitor STAR as electrical resistivity varies with temperature (e.g., Ramirez et al., 1993; Hermans et al., 2015) and water saturation (i.e., boiling of water, combustion gases) (e.g., Wang et al., 2010).

1.2.   Research objectives

The main objective of this research is to provide a proof-of-concept that time-lapse ERT can be used as a complementary source of information to monitor full-scale in situ STAR applications. To achieve this, a shallow STAR treatment and a deep STAR treatment were

monitored in Newark, New Jersey where the first full-scale application of STAR was underway. Two 2D ERT lines were installed in each treatment to obtain electrical resistivity tomograms and these were compared to conventional monitoring acquired by the site (i.e., temperature and combustion gas concentration). This approach is novel as it is the first study to demonstrate the applicability of ERT in DNAPL smouldering remediation. Moreover, this study represents the first time DNAPL source zone remediation was directly mapped in a field setting. Other geoelectrical measurements were obtained, such as Self-potential and Induced Polarization, but analysis of those data is not included in this study. Although the analysis provided here is particular to the site in question, the approaches and conclusions are expected to be useful for other smouldering remediation sites and for the non-intrusive monitoring of other thermal remediation approaches.

1.3. Thesis outline

This thesis is written in as an integrated article format in accordance with the guidelines and regulations stipulated by the Faculty of Graduate Studies at the University of Western Ontario. Each of the chapters in the thesis is described below.

Chapter 1: provides an overview of the project and research objectives.

Chapter 2: summarizes the scientific literature relevant to monitoring STAR with time-lapse ERT.

Chapter 3: presents the full results from the proof-of-concept in situ application of ERT in the first full-scale STAR system in Newark, New Jersey. This chapter is written in a manuscript format for future submission to a peer reviewed journal.

Chapter 4: summarizes the key findings of this research and provides recommendations for future work on ERT applied to smouldering remediation.

Appendices: provide supplemental information that was not included in the scope of the Chapter 3, such as details on STAR operation and ERT installation, normalization tests for inversion, inversions conducted, sensitivity analysis and more examples on focused analysis.

1.4. References

Gaylor, D. W., Culp, S. J., Goldstein, L. S., & Beland, F. A. (2000). Cancer Risk Estimation for Mixtures of Coal Tars and Benzo(a)pyrene. *Risk Anal., 20*(1), 81.

Gerhard, J. I., Pang, T., & Kueper, B. H. (2007). Time Scales of DNAPL Migration in Sandy Aquifers Examined via Numerical Simulation. *Groundwater, 45*(2), 147.

Hermans, T., Wildemeersch, S., Jamin, P., Orban, P., Brouyère, S., Dassargues, A., & Nguyen, F. (2015). Quantitative temperature monitoring of a heat tracing experiment using cross-borehole ERT. *Geothermics, 53*(Complete), 14-26. doi: 10.1016/j.geothermics.2014.03.013

Johnson, T. C., Versteeg, R. J., Day-Lewis, F. D., Major, W., & Lane, J. W. (2015). Time-Lapse Electrical Geophysical Monitoring of Amendment-Based Biostimulation. *Groundwater, 53*(6), 920-932. doi: 10.1111/gwat.12291

Kueper, B. H., & Davies, K. (2009). *Assessment and Delineation of DNAPL Source Zones at Hazardous Waste Sites*.

Kueper, B. H., Stroo, H. F., Vogel, C. M., & Ward, C. H. (2014). *Chlorinated solvent source zone remediation*: Springer.

LaBrecque, D. J., Ramirez, A. L., Daily, W. D., Binley, A. M., & Schima, S. A. (1996). ERT monitoring of environmental remediation processes. *Measurement Science and Technology, 7*(3), 375-383. doi: 10.1088/0957-0233/7/3/019

Lekmine, G., Auradou, H., Pessel, M., & Rayner, J. L. (2017). Quantification of tracer plume transport parameters in 2D saturated porous media by cross-borehole ERT imaging. *Journal of Applied Geophysics, 139*(Complete), 291-305. doi: 10.1016/j.jappgeo.2017.02.024

Mao, D., Revil, A., Hort, R. D., Munakata-Marr, J., Atekwana, E. A., & Kulessa, B. (2015). Resistivity and self-potential tomography applied to groundwater remediation and contaminant plumes: Sandbox and field experiments. *Journal of Hydrology, 530*, 1-14.

Newmark, R. L., Boyd, S., Daily, W., Goldman, R., Hunter, R., Kayes, D., Kenneally, K., Ramirez, A., Udell, K., & Wilt, M. (1994). *Using geophysical techniques to control in situ thermal remediation*.

Pironi, P., Switzer, C., Gerhard, J. I., Rein, G., & Torero, J. L. (2011). Self-Sustaining Smoldering Combustion for NAPL Remediation: Laboratory Evaluation of Process Sensitivity to Key Parameters. *Environ. Sci. Technol., 45*(7), 2980.

Pironi, P., Switzer, C., Gerhard, J. I., Rein, G., Torero, J. L., & Fuentes, A. (2009). Small-Scale Forward Smouldering Experiments for Remediation of Coal Tar in Inert Media. *Proc. Combust. Inst., 32*(2), 1957.

Ramirez, A., Daily, W., LaBrecque, D., Owen, E., & Chesnut, D. (1993). Monitoring an underground steam injection process using electrical resistance tomography. *Water Resources Research, 29*(1), 73-87.

Samouëlian, A., Cousin, I., Tabbagh, A., Bruand, A., & Richard, G. (2005). Electrical resistivity survey in soil science: a review. *Soil and Tillage research, 83*(2), 173-193.

Scholes, G. C., Gerhard, J. I., Grant, G. P., Major, D. W., Vidumsky, J. E., Switzer, C., & Torero, J. L. (2015). Smoldering Remediation of Coal-Tar-Contaminated Soil: Pilot Field Tests of STAR. *Environmental Science & Technology, 49*(24), 14334-14342. doi: 10.1021/acs.est.5b03177

Switzer, C., Pironi, P., Gerhard, J. I., Rein, G., & Torero, J. L. (2009). Self-Sustaining Smoldering Combustion: A Novel Remediation Process for Non-Aqueous-Phase Liquids in Porous Media. *Environ. Sci. Technol., 43*, 5871.

Wang, S., Lee, M., Park, M. K., & Kim, J.-M. (2010). Box experiments on monitoring the CO 2 migration in a homogeneous medium using electrical resistivity survey. *Geosciences Journal, 14*(1), 77-85.

Chapter 2

2. Literature Review

This chapter will review the use of geophysics in the context of contaminated sites and focus on the Electrical Resistivity Tomography (ERT) method and how its hydraulic-electric relationship can support the in situ monitoring of smouldering remediation. This chapter will describe the mechanisms of Self-sustaining Treatment for Active Remediation (STAR), and its applications in the field. It will describe traditional monitoring methods for contaminated site remediation and geophysical techniques. The use of ERT is reviewed and the four dimensions (4D) time-lapse approach is described. Finally, the gaps in the literature and research opportunities are summarized.

2.1. Introduction

Thousands of industrialized areas around the world present subsurface contamination from releases that have been occurring since the middle of the 20th century due to industrial development and poor waste management, as well as commercial and agricultural activities. (Kueper et al., 2014). Even though waste management practices have significantly improved over the past 20 years, accidents still occur. Free phase contaminants that migrate in the subsurface can be denser or lighter than water: dense non-aqueous phase liquids (DNAPLs) and light non-aqueous phase liquids (LNAPLs). LNAPLs, such as gasoline and diesel, spread on top of the water table, and slowly dissolve into the groundwater. Unlike LNAPLs, DNAPLs migrate below the water table and, being relatively immiscible with water, are considered recalcitrant sources of groundwater contamination, causing consequences to human health and the environment (Gaylor et al., 2000; Kueper & Davies, 2009; Kueper et al., 2014). Common DNAPLs released to the environment include coal tar, creosote, chlorinated solvents, and PCB (polychlorinated biphenyl) oils.

Remediation approaches for DNAPLs are commonly separated between source zone remediation (i.e., free phase) and plume remediation (Kueper et al., 2014). Source zone

remediation technologies for DNAPLs are limited (ITRC, 2011). Common technologies for extraction of DNAPL are focused on either using chemicals to enhance dissolution of contaminants for removal (i.e., in situ flushing), or using heat to enhance mobilization and vaporization of contaminants due to reduced viscosity with heat for removal (i.e., steam injection and electrical resistance heating) (Heron et al., 2005; Heron et al., 2009; ITRC, 2011). Common destruction techniques for DNAPL are in situ chemical oxidation, that reacts with the contaminants. All these remedial technologies have limiting economical and technical challenges, when dealing with coal tar.

Coal tar, the focused contaminant of this study, is a complex mixture of contaminants, historically produced at gas operations as a byproduct. Properties of coal tar, such as relatively high viscosity (20-100 centipoise) and low density for a DNAPL (1010 kg/m^3), make it a challenging contaminant to be remediated in situ (Kueper et al., 2014). Coal tar tends to require long-term energy input for extraction, increasing the time and cost of the treatment (Birak & Miller, 2009; Kueper & Davies, 2009). Because of these limitations, the common solution for coal tar source zones is ex-situ removal by excavation and disposal of contaminated soil to a hazardous waste landfill or incinerator, and further treatment of groundwater and residuals (Scholes et al., 2015). Recently, an innovative in situ smouldering remediation called Self-sustaining Treatment for Active Remediation (STAR) has been developed as an alternative remediation treatment to destroy complex DNAPL mixtures, such as coal tar (Pironi et al., 2009).

2.2. Self-sustaining Treatment for Active Remediation (STAR)

STAR is a remediation treatment available for complex NAPL (non-aqueous phase liquids) mixtures that uses the principle of smouldering combustion to destroy contaminants in the subsurface. Smouldering is the process that occurs in the char for a barbecue (Figure 2-1). Smoldering combustion is an exothermic, flameless reaction that occurs on the surface of a solid or liquid fuel in a porous medium, providing the surface area necessary for the oxidation to occur (Pironi et al., 2009; Switzer et al., 2009; Pironi et al., 2011; Scholes et al., 2015). The smouldering rate of reaction is generally limited by the rate that oxidant (i.e. oxygen in air) is supplied via convective and/or diffusive means to the porous medium (e.g., soil, polyurethane

foam). The reaction also requires the presence of fuel (e.g., contaminants, such as coal tar) and heat provided by an igniter (Ohlemiller, 1985; Rashwan, 2015; Rashwan et al., 2016).

Figure 2-1. Smouldering combustion in char coal, where coal acts as both fuel and porous medium.

When achieving ignition temperature, the main reaction occurring in the surface of the fuel is (Rashwan et al., 2016):

Pyrolysis:
$$Fuel + Heat \rightarrow Pyrolysate\ (gas) + Char(solid) + Ash(solid) \qquad \textbf{(1)}$$

Approximately 350°C represents the ignition temperature of coal tar (Switzer et al., 2009). Beyond this, the main reaction is (Rashwan et al., 2016):

Char Oxidation
$$Char\ (solid) + O_2 \rightarrow Heat + CO_2 + H_2O + Ash(solid) + Other\ compounds \quad \textbf{(2)}$$
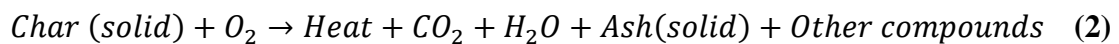
Pyrolysis in an endothermic reaction that thermally breaks down the hydrocarbons in the fuel and generates char (Rashwan et al., 2016; Kinsman et al., 2017). Char is the fuel for exothermic oxidation, liberating heat and converting it to carbon dioxide (CO_2, complete oxidation), carbon monoxide (CO and other volatile compounds, incomplete oxidation), water vapour (H_2O), and ash (Switzer et al., 2009). Because smouldering overall is exothermic the heat

released is transferred through the porous medium, preheating the fuel ahead as long as oxidant is continuously supplied (Switzer et al., 2009). Therefore, the reaction is self-sustained, and no further external energy input is necessary once the smouldering reaction starts (i.e. ignition), establishing STAR as a relatively cost-effective solution for heavy hydrocarbons (i.e. coal tar, creosote) remediation and removal (Pironi et al., 2009).

2.2.1. STAR Laboratory tests

Laboratory tests were conducted to determine optimum conditions for the smouldering reaction to propagate and destroy different types of contaminants (Pironi et al., 2009; Switzer et al., 2009; Pironi et al., 2011). These tests were conducted in a one-dimensional column to simulate an upward forward smouldering. Forward smouldering indicates that the oxidant and the reaction propagate in the same direction; furthermore, upward forward smouldering means that the combustion gases move upwards in the column, transferring the heat ahead of the reaction, increasing the propagation velocity and initiating preheating (Torero & Fernandez-Pello, 1996; Pironi et al., 2009; Switzer et al., 2009; Drysdale, 2011; Pironi et al., 2011). See Figure 2-2 (left) for a common experimental design, where the igniter and the air flow are applied in the bottom of the column and thermocouples are used to measure temperature profiles, positioned in different locations of the column. The column is also commonly based on top of a scale to determine mass losses in the system (Switzer et al., 2009; Rashwan et al., 2016), while combustion gases (CO and CO_2) are monitored.
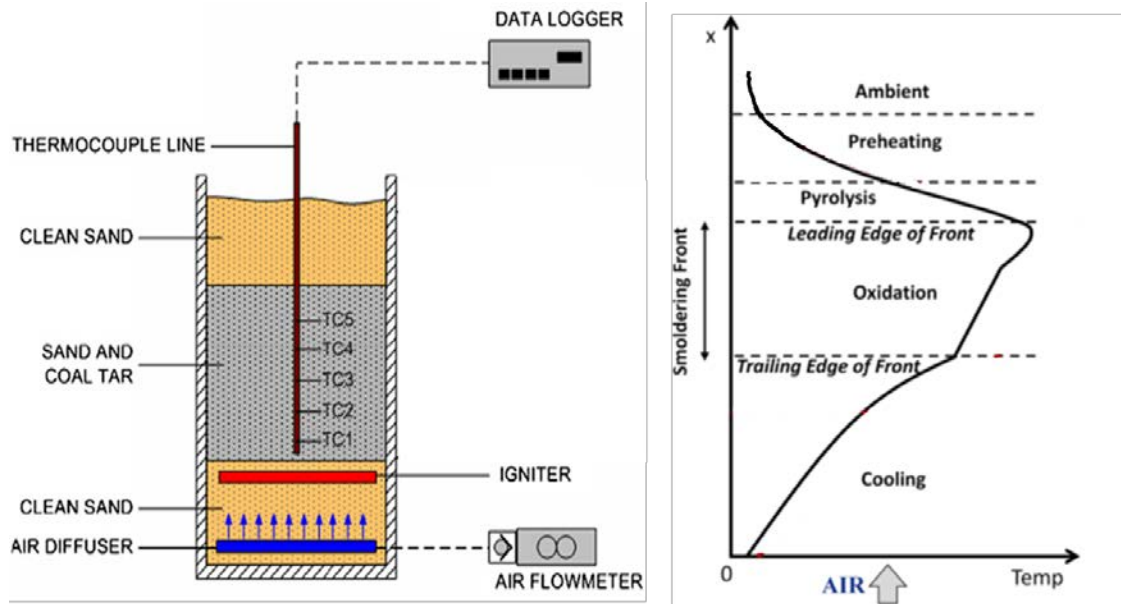
Figure 2-2. (Left) Example of column experiment with upward air injection (modified from Pironi et al., 2009). (Right) Conceptual model of the distribution of temperature in a column experiencing upward air injection. The key regions are named (modified from Kinsman et al., 2017).

The smouldering process in a column experiment is represented in Figure 2-2 (right) (Kinsman et al., 2017). The reaction zone is characterized by pyrolysis and oxidation. The leading edge of the oxidation relates to the smouldering front, that consists of a thin propagation front (thickness of centimeters to tens of centimeters). The smouldering trailing edge front leaves treated soil behind that slowly cools off (Kinsman et al., 2017). Therefore, forward smouldering combustion for these experiments can be characterized by three zones, which thickness depends on heat losses and oxygen supply: preheating, reaction zone, and cooling (Figure 2-2b) (Ohlemiller & Lucca, 1983; Rein, 2009; Hadden et al., 2013; Rashwan et al., 2016).

Initial laboratory experiments were conducted at a bench scale (150 mm diameter column) (Pironi et al., 2009) and in smaller scales (50 mm diameter beaker) (Switzer et al., 2009) and showed that several contaminants, including coal tar, dodecane, DCA mixed with grease, TCE mixed with oil, vegetable oil, crude oil, and mineral oil, with different saturations (10% to 100%) in different porous medium (soil types) can initiate self-sustained smouldering combustion (Pironi et al., 2009; Switzer et al., 2009; Pironi et al., 2011). Most experiments

10

were conducted in dewatered situations. Chlorinated solvents, combined with emulsifiers, and biosolids (not dewatered) were also successfully smouldered (Salman et al., 2015; Rashwan et al., 2016). Limiting conditions observed were heat losses, fuel saturation and type, oxygen availability (i.e. air flux/velocity), moisture content and porous medium grain size and type (Pironi et al., 2011).

A few observations can be made about the smouldering reaction: (i) the reaction velocity is observed to increase linearly with increasing airflow (Ohlemiller & Lucca, 1983; Ohlemiller, 1985; Pironi et al., 2009; Switzer et al., 2009), and (ii) smouldering combustion is confirmed when temperature profiles show self-sustained propagation, and combustion gases are observed (CO_2 and CO), as identified in Figure 2-3 (Switzer et al., 2009).
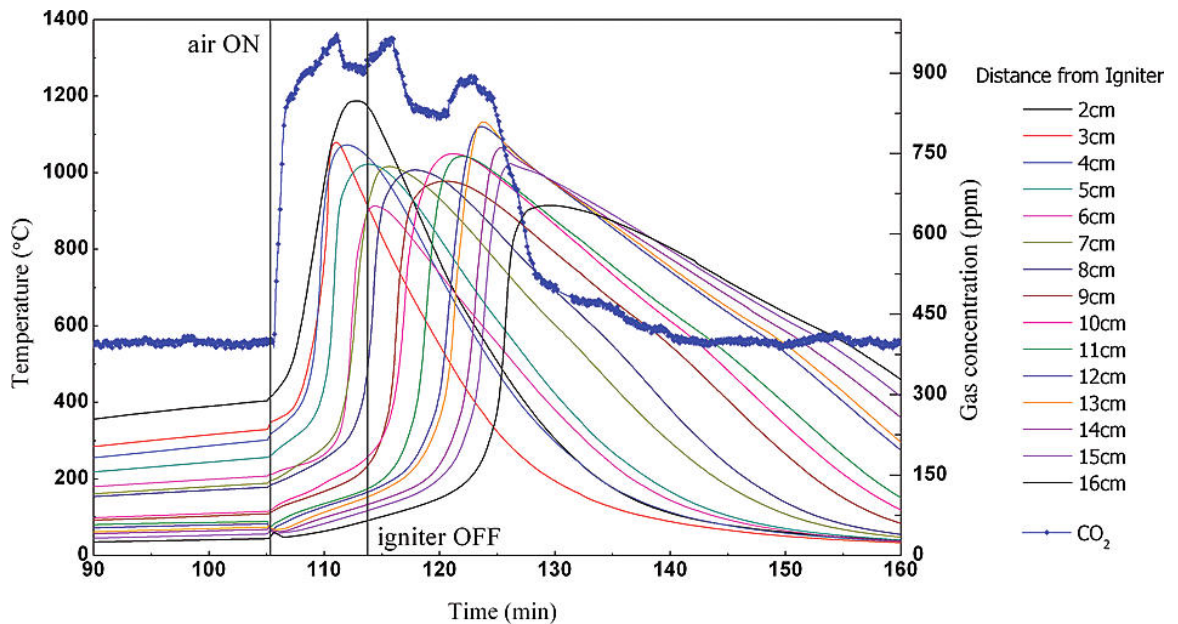
Figure 2-3. Typical temperature versus time data for a STAR column experiment, with gas data. Stages of preheating (90-105 min), ignition (105 min), combustion (105-115 min), self-sustaining combustion (115-125 min) and cooling (Switzer et al., 2009).

Experiments also showed that water/moisture in the column experiments reduce the peak temperatures of the smouldering reactions (Figure 2-4) and, at a minimum 25% NAPL saturation (75% water saturation), self-sustaining smouldering reaction still occurs (Pironi et al., 2011). In addition, with high temperatures, the water evaporates to further condensate in

the cooler zones of the column ahead of the propagation front, limiting the extent of propagation (Ohlemiller, 1985).
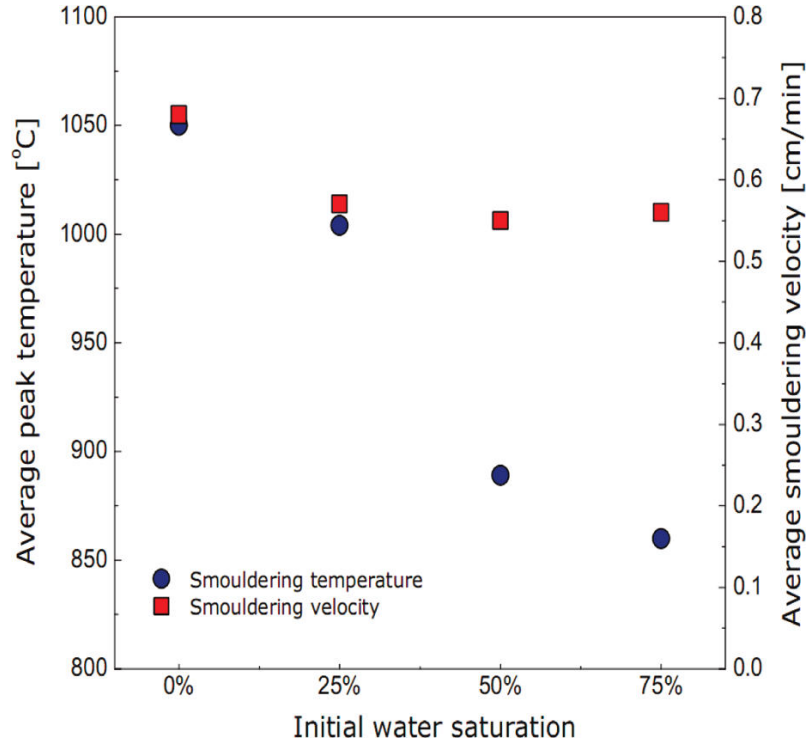
Figure 2-4. Average peak temperature (blue circles, left vertical axis) compared to average smoldering velocity (red squares, right vertical axis), against initial water saturation. Initial coal tar concentration was constant (Pironi et al., 2011).

2.2.2. Full scale application of STAR

The potential of smoldering combustion as a remedial action has been recently examined in a pilot scale by conducting tests at a site contaminated by coal tar, in Newark, New Jersey (Scholes et al., 2015). As mentioned previously, heat losses in column experiments were one of the limiting conditions to terminate self-sustaining smouldering reactions (Switzer et al., 2009; Pironi et al., 2011). In field scale, for in situ applications of STAR, the boundaries are expanded (i.e., no column walls, more porous medium) and heat losses are expected to be reduced, increasing the amount of NAPL destroyed per unit energy added to the system (efficiency of smouldering) (Pironi et al., 2011; Scholes et al., 2015). At in situ applications, it is also expected that STAR will be applied below the water table, which absorbs the energy from the smouldering reaction, acting as a heat sink, decreasing the peak temperature of the

reaction and adding another step in the smouldering process: a plateau at boiling temperatures until water is evaporated in the reaction zone before smouldering can start (Pironi et al., 2011).

The field site, previously a chemical manufacturing plant, is approximately 15 hectares (0.15 km^2). Two tests were conducted using ignition points (IP, a 5-cm carbon steel well with a unique grout mixture to maintain a seal at high temperatures) that were installed at the desired treatment depth to start the smouldering reaction. The IP served as heat and air injection point, and the preheating period is characterized as a hot air being injected (~500 ºC), heating the subsurface (i.e., surrounding of the IP, including DNAPL and soil) until boiling and ignition temperatures are reached. As observed in the laboratory experiments, the heater is turned off while air injection is maintained, once ignition occurs (Scholes et al., 2015). The propagation reaction occurs mostly laterally, spreading in outwards from the IP, with a thin reaction zone (tens of centimeters). The clean soil behind the front slowly cools and is later re-infiltrated by groundwater (Scholes et al., 2015; Kinsman et al., 2017), typically after the air injection is terminated (Scholes et al., 2015). For the pilot studies, horizontal vapor extraction points (VEPs) extract the gases and treat them on site (Scholes et al., 2015).

The pilot scale tests were conducted in two coal tar contaminated soil layers: shallow fill (approximately 3 meters below ground surface, mbgs) and deep Alluvium (approximately 7.9 mbgs), separated by a clay layer (Meadow Mat) (Figure 2-5). For each treatment zone, one IP was installed and the smoldering combustion propagation front was monitored using temperature data obtained by a network of thermocouples, which were installed in different depth and locations in a dense grid, being 166 monitoring points for shallow test and 99 monitoring points for deep test (Scholes et al., 2015). Because of the dense grid of thermocouples, propagation front velocities and treatment radius of influence (ROI) were identified. The median propagation front velocities obtained from the pilot scale were 1.04 m/day for the shallow test and 0.67 m/day for the deep test. A radius of influence (ROI) was possible to be obtained for the deep test, as 3.7 m ROI and 1.9 m treatment zone thickness. The shallow test had lateral channeling of the reaction due to the heterogeneity of the layer where the IP was installed, therefore, lateral spread of the reaction (ROI) was not obtained. However, the treatment zone thickness was possible to be observed (1.1 m) (Scholes et al., 2015). Combustion gases (CO_2 and CO) were also monitored using the VEPs (Scholes et al., 2015).
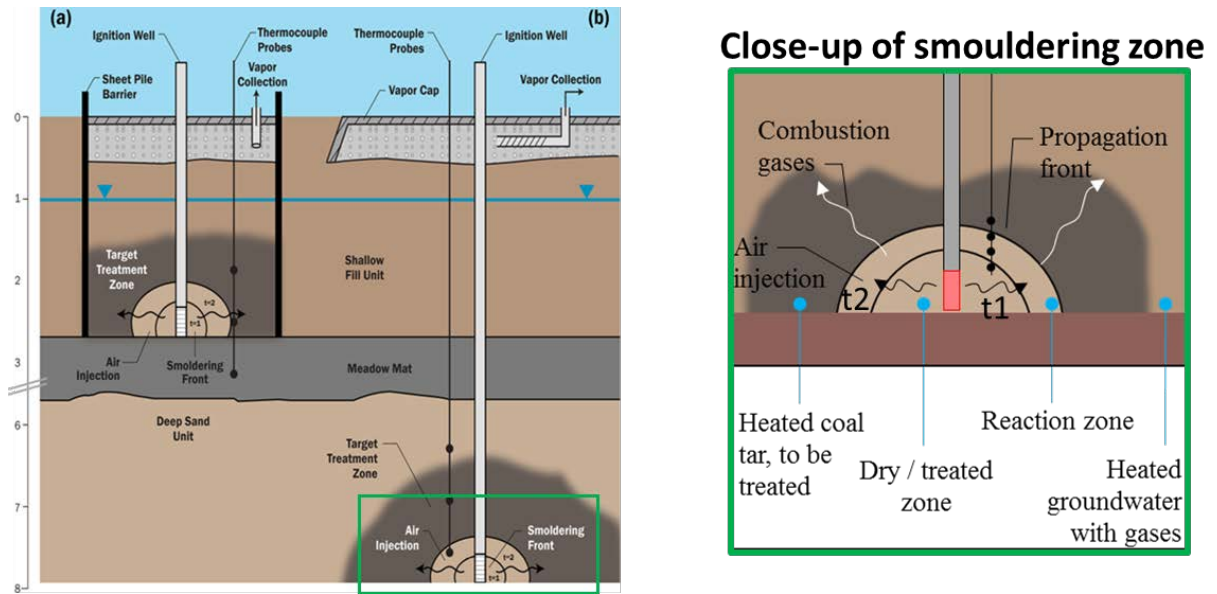
Figure 2-5. (Left) Schematic cross-section of (a) shallow and (b) deep field-test cells. The shallow field test unit was contained by a sheet pile barrier, while the deep was not. Both field tests were initiated below the water table. Propagation of the smoldering front is shown outside the ignition well screens: t = 1 coincides with the preheated zone and onset of smoldering, while the front location at t = 2 represents self-sustained smoldering with only air injection (modified from Scholes et al., 2015). (Right) Close-up of smouldering zone with treatment steps as shown in Figure 2-2b.

After the successful pilot scale was conducted, the first full-scale STAR system was implemented at the same contaminated site for both treatment units. STAR is being applied in a series of treatment cells in shallow fill and deep Alluvium layer. Each cell consists of (i) 5 to 10 ignition points with screens installed at the desired depth of treatment; (ii) multilevel thermocouples bundles installed 0.3 m from each IP, each multilevel thermocouple consists of four thermocouples installed near the screen of the IPs, 0.2 meters apart from each other (0.8 meters of total horizontal coverage); and (iii) 6 to 8 vertical VEPs that collect vapors produced during combustion, as well as groundwater collected mainly in the shallow unit.

2.2.3. STAR monitoring

Although comprehensive data collection was acquired during a pilot scale of in situ STAR (for example, temperature measurements points were 166 for shallow tests and 99 for deep tests

for each IP) (Scholes et al., 2015), data collected from full-scale are limited to (i) four temperature measurements points for each IP to identify ignition of a burn/smouldering reaction, (ii) captured CO and CO_2 to estimate the mass of contaminant destroyed by smouldering, and (iii) pre- and post-treatment coring. Collecting these data is not only invasive and expensive, but mostly sparse and discrete both in space and time (Kavanaugh et al., 2003) and provides information on ignition of IPs and duration of burn, however complementary information is desirable considering that temporal monitoring is an essential component to determine the efficiency, performance and success of remediation (Kavanaugh et al., 2003; Power et al., 2014; Power et al., 2015).

2.3. Geophysical monitoring

The area of hydrogeophysics has been used for characterizing contaminated sites and monitoring remediation, in particular, geoelectrical methods (Slater & Lesmes, 2002; Revil et al., 2012; Loke, 2013). Geoelectrical methods, such as self-potential (SP), electrical resistivity tomography (ERT), and induced polarization (IP), are non-intrusive or minimally intrusive methods and have been used across a wide range of hydrogeological investigations, and to complement aspects of environmental assessment, characterization and remediation of contaminated sites (Revil et al., 2012). Self-potential is a passive method, meaning that no current is injected in the ground, therefore natural current generated is measured being directly correlated to flow of groundwater, temperature and chemistry soil variations (Revil et al., 2012; Mao et al., 2015). A recent study that monitored STAR laboratory experiments using the SP method showed promising results (Ebrahimzadeh et al., 2017).

Induced polarization and ERT are both active geophysical methods, where current is injected in the ground. ERT images the resistance of the subsurface to the applied current flow, translated into electrical resistivity, while induced polarization is an extension of resistivity methods, with time varying current. Therefore, in addition to resistivity, IP method can measure the ability of porous materials to store electrical energy, as if the subsurface was a capacitor, providing the chargeability of the materials – which is an indicative of clay minerals or metallic particles (Revil et al., 2012; Sparrenbom et al., 2017).

Electrical Resistivity Tomography (ERT) has a wide range of applications from environmental assessment and hydrogeological characterization (Daily et al., 1992; Daily & Ramirez, 1995; Atekwana et al., 2000; Slater et al., 2000; Miller et al., 2008; Lekmine et al., 2017) to mapping contaminant distribution (Newmark et al., 1998; Clément et al., 2011; Power et al., 2014; Deng et al., 2017), groundwater quality (Nguyen et al., 2009), and distribution of injected amendment fluids (Lane et al., 2006).

Time-lapse ERT is a method that collects several images over time to focus in monitoring subsurface changes (natural or induced), by collecting a background reference image and removing it from next images, separating static interferences and geological information from the analysis. It has shown significant potential with advances in time-lapse data collection (Wilkinson et al., 2010) and inversion algorithms (Kim et al., 2009; Karaoulis et al., 2011; Power et al., 2014). Time-lapse ERT has been used to monitor aqueous contaminant plumes (Daily et al., 1992; Daily & Ramirez, 1995), and several remediation technologies, such as permanganate injections for in situ chemical oxidation (Mao et al., 2015; Tildy et al., 2017), bioremediation (Johnson et al., 2015; Masy et al., 2016; Sparrenbom et al., 2017), iron permeable reactive barriers (PRB) (Slater & Binley, 2003), zero valent iron oxidation (Slater & Binley, 2006), thermal remediation using Joule (ohmic) heating, in which the subsurface is heated electrically, and steam injection (Ramirez et al., 1993; LaBrecque et al., 1996) with research covering laboratory, pilot and field scales.

2.3.1. Electrical Resistivity Tomography (ERT) basic principles

DC electrical resistivity is based on Ohm's Law and, since 1883, the idea of applying electrical resistivity to identify mineral deposits has been investigated (Revil et al., 2012), Ohm's Law equation for a simple body, defines the resistance as (Samouëlian et al., 2005):

$$R = \Phi / I \text{ (Ohms Law)} \qquad\qquad (\textbf{Equation 1})$$

Where R is the electrical resistance (ohms, Ω), Φ represents the potential (volts, V) and I is the current (Amperes, A). Electrical current is defined as the flux of charge carriers (i.e., electrons, cations and anions) through a given cross-sectional area (Revil et al., 2012). Therefore,

electrical resistivity ρ (ohm · meters, Ω · m) for a simple body, such as a cylinder, with length (L, in m) and cross-section (S, in m^2) receiving current, is defined by (Samouëlian et al., 2005):

$$\rho = R\left(\frac{S}{L}\right) \qquad \text{(Equation 2)}$$

Electrical resistivity is a property of the material where current is flowing through, and can also be converted to electrical conductivity σ (Siemens per meter, S/m), the reciprocal of resistivity (σ=1/ρ), which measures how current flows in a certain volume of porous media (Revil et al., 2012).

At the macroscopic scale at continuous medium, it is possible to relate the electric field intensity (**E,** V/m) to the conduction current density (**J,** A/m^2) using Ohm's Law in the vector form (Tsourlos, 1995; Revil et al., 2012).

$$\boldsymbol{J} = \sigma\boldsymbol{E} \qquad \text{(Equation 3)}$$

The electric field potential (Φ, V) is the property measured during electrical surveys. The relationship of the electrical field intensity and the electric field potential is described as (Revil et al., 2012):

$$\boldsymbol{E} = -\nabla\Phi \qquad \text{(Equation 4)}$$

By combining Equation 3 and 4, we obtain (Revil et al., 2012; Power, 2014; Power et al., 2015)

$$\boldsymbol{J} = -\sigma\nabla\Phi \qquad \text{(Equation 5)}$$

which represents the source current density in relation to the electric field potential, for a point source. Assuming that ∇V is an elemental volume near current source $\boldsymbol{I}$, located at (x_s, y_s, z_s), the point source form that is used for most surveys is described by (Dey & Morrison, 1979; Power, 2014; Hermans et al., 2015):

$$\nabla J = \frac{1}{\nabla V} \delta(x - x_s)\delta(y - y_s)\delta(z - z_s)$$ (**Equation 6**)

Where δ is the Dirac delta function, a unit impulse symbol. To obtain the forward modelling problem for ERT, which describes the potential observed by a determined subsurface structure in three dimensions (3D), Equation 5 is combined with Equation 6, and described as the partial differential equation (Loke, 2013):

$$-\nabla \cdot [\sigma(x, y, z)\nabla\Phi(x, y, z)] = \frac{1}{\nabla V} \delta(x - x_s)\delta(y - y_s)\delta(z - z_s)$$ (**Equation 7**)

Note that this equation is defined for the potential distribution due to a point current source of a non-uniform, isotropic and homogenous medium, as shown in Figure 2-6 below.

2.3.2. Data acquisition

The current flow line distribution depends on the medium under investigation; they are concentrated in conductive volumes and avoid resistive units (Samouëlian et al., 2005). In a homogeneous and isotropic half-space, equipotential lines have the form of a semi-sphere; this is observed when only one current electrode is positioned in the ground (Figure 2-6).

2.
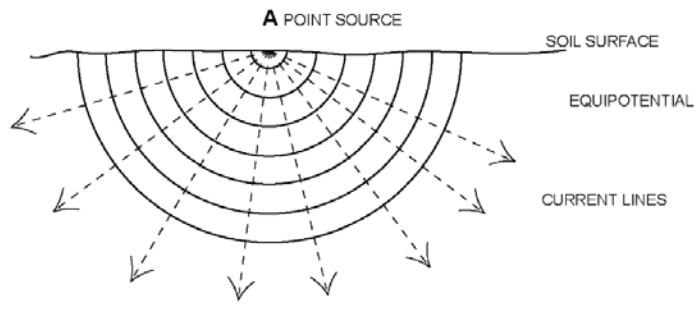
Figure 2-6. Distribution of the current flow in a homogeneous soil (Samouëlian et al., 2005).

Consider Figure 2-6, where a point-source current is being injected in a homogeneous subsurface with resistivity ρ. The semi-sphere at a point r, has $2\pi r^2$ as its surface area, therefore, the electrical potential is (Tsourlos, 1995; Samouëlian et al., 2005; Revil et al., 2012):

$$\Phi = {\rho I}/{2\pi r}$$ (**Equation 8**)

In reality, Figure 2-6 is not feasible, as no potential electrode is receiving the signals and the return electrode is moved in an infinite distance to act as a current sink (Mussett & Khan, 2000). Standard surface electrical resistivity measurements consist of four electrodes (metal rods) installed in the surface (6 inches- into the ground), two current electrodes normally denominated as electrodes A and B, that will inject the current, and the potential electrodes, that measures the resulting potential difference, denominated M and N, as shown in Figure 2-7 (Revil et al., 2012). The potential equations in potential electrodes M and N are also shown in Figure 2-7. The current electrodes cannot be used at the same time to measure the associated drop of the electrical potential, due to the contact impedance across the electrodes, especially at low frequencies (Samouëlian et al., 2005; Revil et al., 2012).

$$\Phi_N = \frac{\rho I}{2\pi}\left[\frac{1}{AN} - \frac{1}{BN}\right]$$

$$\Phi_M = \frac{\rho I}{2\pi}\left[\frac{1}{AM} - \frac{1}{BM}\right]$$
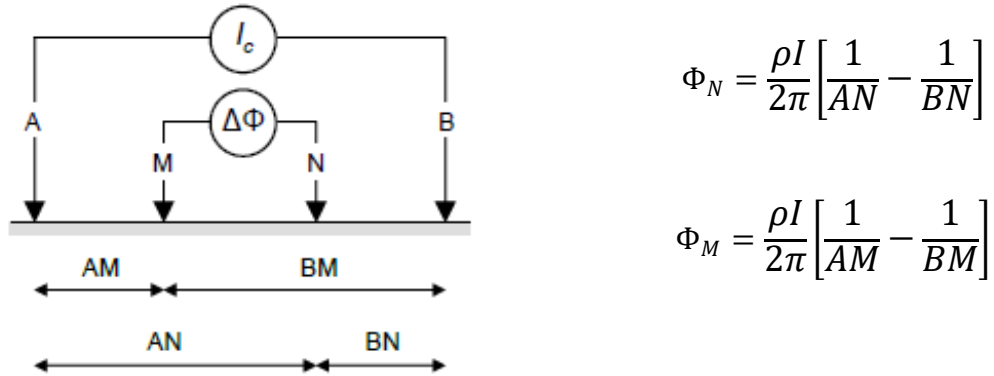
Figure 2-7. Illustration of a four-electrode station containing current and potential electrodes, with equations for potential in N and M (modified from Power et al., 2014).

Therefore, the potential difference **ΔΦ** is measured between the electrodes M and N and is given by Equation 9:

$$\Delta\Phi = \frac{\rho I}{2\pi}\left[\frac{1}{AM} - \frac{1}{BM} - \frac{1}{AN} + \frac{1}{BN}\right]$$ (**Equation 9**)

Where AM, BM, AN and BN represent the geometrical distance between the electrodes. Considering different electrode configurations, the geometrical components of Equation 9 is called K (geometrical factor). The electrical resistivity is then calculated using Equation 10:

$$\rho_a = \frac{\Delta\Phi}{I}\left[\frac{2\pi}{\frac{1}{AM}-\frac{1}{BM}-\frac{1}{AN}+\frac{1}{BN}}\right] = K\left(\frac{\Delta\Phi}{I}\right) \qquad\qquad (\textbf{Equation 10})$$

When collecting electrical resistivity data, the measured value is the apparent electrical resistivity ρ_a (ohm·m). The apparent resistivity is equal to the true resistivity when the medium that the current is applied to is homogenous and isotropic. To collect the apparent resistivity data, different electrode arrays and configurations have been suggested in the literature, each one with an intrinsic geometrical factor (Dahlin & Zhou, 2004; Samouëlian et al., 2005). Only a few configurations are extensively used, such as Wenner, dipole-dipole, pole-dipole, and Schlumberger (Loke, 2013; Power, 2014). Some arrays, like the dipole-dipole array, are more suitable for vertical imaging (Loke, 2013). Electrodes can also be placed inside boreholes to increase the resolution at depth, typically using dipole-dipole and pole-dipole arrays (Danielsen & Dahlin, 2010; Hermans et al., 2015; Commer et al., 2016). Optimized arrays, that focus on a known target, are being more commonly used (Wilkinson et al., 2006; Loke et al., 2015). The choice of a particular resistivity array for a survey is based upon considerations regarding theoretical advantages and its signal-to-noise ratio (Loke, 2013).

The standard resistivity measurements, using only four electrodes as described above is designed for one dimensional (1D) vertical sounding profiling (Revil et al., 2012). This method is the basis for 2D and 3D approaches more commonly used, recently, when automatization of the monitoring has made the surveys less work-intensive. The multichannel automatic systems allow surveys to be conducted with many electrodes (e.g., 96 electrodes for Iris systems), with different separations and distribution. For 2D surveys, the resistivity is assumed to change in depth and laterally, but not perpendicular to the survey lines, which is often not the case for hydrogeological characterization in heterogenous locations or environmental remediation (Power, 2014; Hermans et al., 2015). For that reason, 3D surveys are more common, and the most practical method to obtain 3D data involves collecting apparent resistivity measurements along sets of parallel and/or orthogonal 2D lines (Bentley & Gharibi, 2004).

For time-lapse ERT, the process involves repeating the conventional procedure of an ERT survey through time, collecting multiple images of the same target (Power et al., 2014; Power et al., 2015). Time-lapse monitoring inversion algorithms is a new and growing field of research that tries to improve the inversion stability and reduce inversion artifacts (Kim et al., 2009; Karaoulis et al., 2011; Power et al., 2015). Artifacts are false anomalies generated due to noise that mask or add changes in the subsurface. Even though inversions algorithms are improving over the years, non-uniqueness of geophysical interpretation, due to inversion or inherent geological ambiguities, is still a challenge in the field of hydrogeophysics, therefore, ERT is commonly used as a complementary line of evidence to the conventional methods of monitoring.

2.3.3. Inversion of ERT data

As discussed previously, electrical resistivity measurements provide the apparent resistivity that is calculated using the current, potential difference and geometrical factor (to convert electrical resistance) of the array used in the field. The measured apparent resistivity is a volume-averaged value affected by all the geologic formation through which the induced electric current flows. An inversion procedure is the standard processing tool applied to geoelectrical data to "transform" the measured apparent resistivity data into a model of the "true" subsurface resistivity. The overall purpose of the inversion algorithm is to iteratively find a subsurface resistivity model that will produce observations (calculated data) which are as close as possible to the actual ones measured in the field (i.e. the apparent resistivity) (Hermans et al., 2015). A measure of the quality of the produced model is the % misfit between the actual and the calculated observations. Inversion for electrical resistivity data is a continuously improving field of research that is focused on generating a more accurate and fast algorithms to model the subsurface.

Typically, in geoelectrical prospecting a smoothness based inversion scheme is used (Binley & Kemna, 2005; Hermans et al., 2014) as otherwise inversion procedure can be unstable. So effectively the solution that is obtained is the smoothest model which at the same time minimizes the misfit between the observed and modelled data (Tikhonov et al., 2013; Hermans et al., 2014). The objection function which seeks for a solution to minimizes both the data misfit and the model roughness has the following form (Hermans et al., 2015):

$$S = \Phi_d + \lambda\Phi_m = \|D - G(X)\|^2 + \lambda^2\|CX\|^2 \qquad \textbf{(Equation 11)}$$

where S is the objective function to be minimized, Φ_d is the data misfit vector (recorded data minus modeled data), Φ_m is a regularization function and λ is the Lagrangian multiplier used for controlling the regularization function Φ_m, X denotes inversion model generated after iteration of the bulk resistivity data collected, D denotes the acquired ERT data, G is the forward operator, and C is the spatial second-derivative operator (Power, 2014; Power et al., 2015). Equation 11 is better explained when considering that the first term of the right-hand side ensures that the inverted model generated converges well with the resistivity recorded data; and the second term stabilizes the inversion to produce smoother inverted models with every iteration (Constable et al., 1987; Power, 2014). To solve the minimization of *S*, the iterative Gauss-Newton algorithm is typically used in geoelectrical problems (Hermans, et al., 2014) and involves using a sensitivity matrix (i.e., Jacobian) (Power et al., 2014).

This inversion algorithm is the basis for independent inversions, where only one image in time is inverted and the true resistivity is imaged. Time-lapse ERT processing and interpretation gas also developed over the years, as geoelectrical monitoring is increasingly used. There are three ways of performing time-lapse ERT inversions: (i) independent inversion, (ii) differential inversion and (iii) 4D time-lapse inversions (Hermans et al., 2014).

The independent inversion consists in inverting the images separately, and simply performing ratios or subtractions from one inversion result to the other (Tsourlos et al., 2003). This process should eliminate systematic errors, but amplify uncertainties in the data (Kim et al., 2009; Hermans et al., 2015; Power et al., 2015). The independent inversion was used in initial time-lapse research (Ramirez et al., 1993; LaBrecque et al., 1996), but to minimize the artifacts that were generated by independently inverting and subtracting the images, a difference inversion algorithm (LaBrecque & Yang, 2001; Miller et al., 2008; De Franco et al., 2009) was developed. This consisted of inverting the differences of images between a selected a priori background reference and all the further images collected. Even though this method provides a good first guess for the algorithm and make it converge faster, while cancelling of systematic

errors (Power, 2014), the difference inversion was too dependent of the background reference model (Kim et al., 2009).

Therefore, 4D time-lapse inversion algorithms have been the focus of research in recent years (e.g., Kim et al., 2009; Karaoulis et al., 2014; Loke et al., 2014). In this method, the entire collected data set is defined in a space-time domain and simultaneously inverted (Kim et al., 2009; Power, 2014; Power et al., 2014; Power et al., 2015). As opposed to independent inversions, which use regularizations only in the space domain, a second regularization is introduced in the time domain to stabilize and reduce inversion artifacts (Kim et al., 2009, Kim et al., 2011, Power et al., 2014, Power et al., 2015). As mentioned, the 4D approach inverts all images simultaneously, therefore a subsurface model X for all monitoring steps is identified as $X=[X_i…,X_t]^T$, and the entire collected monitoring data for all monitoring steps is defined as the vector $D=[D_i…,D_t]^T$. Xi and Di are the generated inverted model and the data collected, respectively, for the *i*th monitoring step and *t* is the number of monitoring steps performed (Power et al., 2014). Following the same process as the independent inversion, the objective function S to be minimized is (Kim et al., 2009):

$$S = \Phi_d + \lambda\Phi_m + \alpha\Phi_t$$ (**Equation 12)**

where Φ_m and Φ_t are the two regularization functions, as mentioned previously, for the space and time, respectively. The parameters λ and α are the Lagrangian multiplier for controlling the regularization in space and in time, respectively. This function is also minimizing in an iterative process (see Karaoulis et al., 2011, Power et al., 2015), using the Jacobian or sensitivity matrix.

The space-domain Lagrangian can be optimized with several schemes such as active constraint balancing (ACB) (Yi et al., 2003) and 4D active time constraint (4D-ATC) method introduced by Karaoulis et al. (2011). The regularizations can be performed in an L2-norm, as showed previously, or in an L1-norm. This is also applied in the 4D time-lapse inversions, where L1- and L2-norms can be use in either λ (space domain) or α (time domain). A third regularization (either L1- or L2-norm) can also be applied to the model roughness (see Kim et al., 2013). L1-

norm minimization helps overcome problems with too smoothly varying and diminished model changes, characteristics of the L2-norm (Kim et al., 2013).

2.3.4. Hydrological and resistivity properties

The electrical resistivity depends on the nature and arrangement of solid constituents (textural properties, porosity, pore shape, particle size distribution), pore fluid composition (water content, contaminants, saturation, salinity), presence of clay (mineralogy), and temperature (Samouëlian et al., 2005; Hermans et al., 2014; Hermans et al., 2015). In terms of soil types, Figure 2-8 presents a wide range of resistivity and conductivity for different soil and groundwater, that happens due to the particle size of each soil type and their surface charge (i.e., clays have a larger density of charge and surface area than coarse sand) (Samouëlian et al., 2005; Revil et al., 2012; Hermans et al., 2014) and the chemistry within the water, where electrical flow changes due to ionic or electrolytic composition of pore fluid, salinity, temperature and pressure (Haslam et al., 2014).
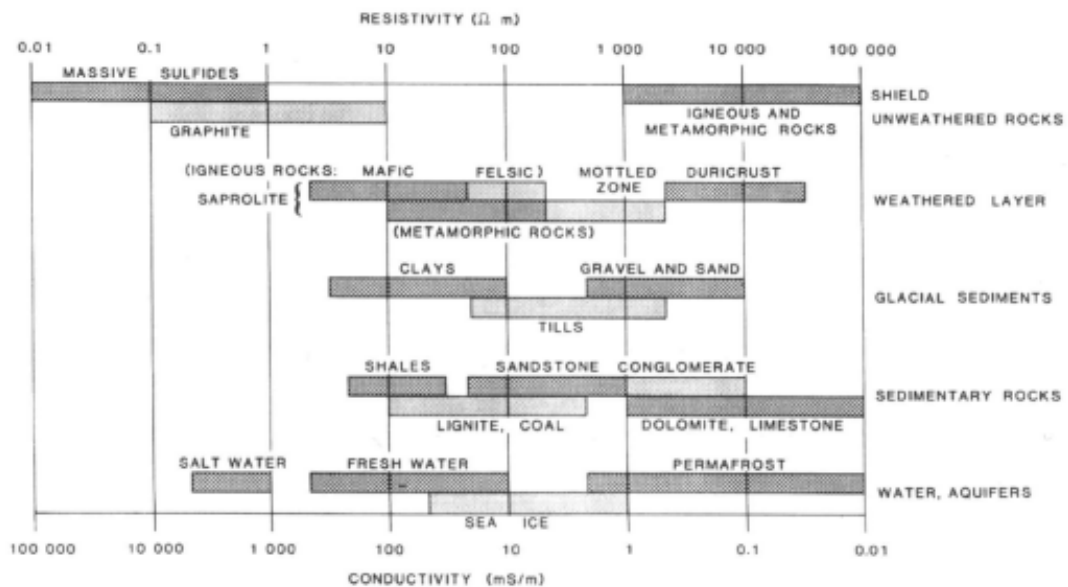
Figure 2-8. Resistivity (and conductivities) of common rocks and water in aquifers (Samouëlian et al., 2005).

The geometry of the pores also interferes as it controls the proportion of fluids present in the pore space, and is described as the main dependent parameter for the electrical conductivity in

porous media. Porosity and water saturation can be related to electrical resistivity through a modified version of Archie's Law, for coarse grains without clay (Samouëlian et al., 2005):

$$\rho = a\rho_w \phi^{-m} S_w^{-n}$$ (**Equation 13**)

where ρ is the electrical resistivity of the rock (bulk resistivity), ρ_w is the resistivity of the conducting fluid (most commonly saline water or an aqueous solution), ϕ is the porosity of the rock and S_w is the saturation (or proportion of pore space) occupied by the conducting fluid (water). The values of "a, m and n" are determined by laboratory experiments or numerical modeling, and refer to the saturation coefficient, cementation factor, and saturation degree, respectively, being normally constant and dependent on the pore morphology (Samouëlian et al., 2005; Haslam et al., 2014).

As observed in Equation 13, decreasing water saturation in the porous medium causes an increase in resistivity. This characteristic of resistivity has been demonstrated in several ERT surveys, including mapping air sparging remediation (Lundegard & LaBrecque, 1995; LaBrecque et al., 1996) and CO_2 sequestration in brine mines (Wang et al., 2010; Carrigan et al., 2013; Commer et al., 2016; Schmidt-Hattenberger et al., 2016), where air or gases are removing water from the porous medium by displacement or dissolution. The same can occur with other fluids, that are also more resistive than water, such as DNAPLs in general. When DNAPLs displaces water or, the reverse happens, when DNAPLs are remediated and water is once again occupying the majority of the porous medium, time-lapse ERT has potential to evaluate and monitor DNAPL movement and remediation, as shown with numerical modeling and laboratory experiments (Power et al., 2014; Power et al., 2015). However, to the authors knowledge, no field study has employed ERT for directly evaluating the loss of DNAPL mass during remediation applications.

As well as saturation changes, temperature changes also present an influence in resistivity. In most of the studies, resistivity changes with temperature are seen as noise, and a simple correlation (e.g., conductivity increases 2.02% per °C between 15 and 35 °C) is used to correct the resistivity data (Hermans et al., 2014). However, the effect of temperature on resistivity has also been evaluated to map geothermal sources (Hermans et al., 2014) and track

groundwater flow via seasonal temperature variations (Hermans et al., 2015; Giordano et al., 2017). These studies represent low temperatures variations, where boiling temperatures are not reached. However, as water heats (decreasing resistivity) reaching boiling temperature, water saturation decreases simultaneously (increasing resistivity), and this relationship is described in another modified version of Archie's Law, up to boiling temperatures (Ramirez et al., 1993):

$$\frac{\rho_{(T_2)}}{\rho_{(T_1)}} = \left(\frac{S_{w2}}{S_{w1}}\right)^{-2} \times \left(\frac{T_1}{T_2}\right)$$
(**Equation 14**)

where T_1 and T_2 are temperatures in time 1 and temperatures in time 2, respectively. Sw_1 and Sw_2 are water saturation for time 1 and time 2. Equation 14 describes the effect of temperature in water saturation compared with resistivity changes. As shown by Ramirez et al. (1993), for temperature ratio of boiling temperature to room temperature, resistivity decreases ($\rho_{(T2)}$) until saturation reaches 0.55, after that, the resistivity starts to increase. These temperature and saturation changes are shown in studies where temperature increases above boiling temperature, such as steam injection to volatilize organic contaminants (Ramirez et al., 1993). It is important to notice that this equation does not consider the effect of contaminants in the pore, and how they are influenced by temperature changes.

DNAPLs are considered more resistive than water (Power et al., 2014). However, with temperature increases, their resistivity decreases. In this way, DNAPLs in the pores space will behave similarly as water in Equation 14. At the same time, some DNAPLs, such as chlorinated solvents, exhibit boiling temperature below that of water. In this case, it is expected that Equation 14 is still valid, however the increase in resistivity associated with increasing air saturation will happen at temperatures below that for boiling water.

2.4. Summary and key gaps in the literature

In this chapter, scientific literature of the smouldering technology STAR in the laboratory and field scales are reviewed, as well as how the use of time-lapse ERT, data collection, inversion, and its responses to water saturation and temperature changes. Examples of ERT applied to remediation technologies are indicated. From this review, the following observations can be made:

- DNAPLs, such as coal tar, migrate below the water table and are challenging to remediate in situ, being that tentative technologies to treat them are expensive and energy-intensive. Common solution is to excavate the contaminants and dispose in hazardous landfills or incinerate them.

- A novel solution to remediate DNAPLs, such as coal tar, was developed based on smouldering remediation. Self-sustaining Treatment for Active Remediation (STAR), was studied in laboratory and applied to the field in Newark, New Jersey to remediate coal tar.

- STAR application in the field is different than laboratory experiments, as it presents less heat losses. At the same time, STAR field application is installed under the water table, acting as a heat sink.

- Full-scale application of STAR has limited conventional monitoring, as the treatment is monitored with a simple grid of thermocouples that track ignition and combustion gases concentration data. Pre- and post- coring is also collected.

- Geophysical techniques, such as time-lapse ERT, an inexpensive method compared to conventional monitoring, that compares images taken overtime with a background image to monitor changes in the subsurface. ERT is non-intrusive and responds to the resistance of current flow of the subsurface.

- Electrical resistivity, a property of materials, changes due to temperature, water saturation, porosity and soil type. When a more resistive fluid is added to the subsurface and water saturation changes (e.g., CO_2 generation and sequestration to the subsurface, air injection, DNAPL migrating into the subsurface), resistivity increases. When a more conductive fluid is added to the subsurface (e.g., hot or warm water, DNAPL being displaced or removed giving space to water), resistivity decreases.

- In complicated settings, where water saturation and temperatures are changing over time, simultaneously (i.e., steam injection, thermal remediation), there is a limit to the saturation value where above the limit, resistivity decreases due to temperature effects. Passing the saturation limit, resistivity starts to increase, due to water saturation decreases.

Based on available literature, there are gaps in the applicability of ERT to monitor environmental remediation:

- More recently, time-lapse ERT has been applied to monitor remediation sites, such as bioremediation, air sparging, in situ chemical oxidation. However, most of the studies are focused on the groundwater plume remediation.

- There are limited studies on the application of time-lapse ERT to monitor thermal remediation. To the knowledge of the authors, no studies were conducted to monitor DNAPL source zone remediation in situ. ERT was never applied to a STAR remediation.

2.5. References

Atekwana, E. A., Sauck, W. A., & Werkema, D. D. (2000). Investigations of geoelectrical signatures at a hydrocarbon contaminated site. *Journal of Applied Geophysics, 44*(2), 167-180.

Bentley, L. R., & Gharibi, M. (2004). Two-and three-dimensional electrical resistivity imaging at a heterogeneous remediation site. *Geophysics, 69*(3), 674-680.

Binley, A., & Kemna, A. (2005). DC resistivity and induced polarization methods *Hydrogeophysics* (pp. 129-156): Springer.

Birak, P. S., & Miller, C. T. (2009). Dense non-aqueous phase liquids at former manufactured gas plants: Challenges to modeling and remediation. *J. Contam. Hydrol., 105*, 81.

Carrigan, C. R., Yang, X., LaBrecque, D. J., Larsen, D., Freeman, D., Ramirez, A. L., Daily, W., Aines, R., Newmark, R., & Friedmann, J. (2013). Electrical resistance tomographic monitoring of CO 2 movement in deep geologic reservoirs. *International Journal of Greenhouse Gas Control, 18*, 401-408.

Clément, R., Oxarango, L., & Descloitres, M. (2011). Contribution of 3-D time-lapse ERT to the study of leachate recirculation in a landfill. *Waste Management, 31*(3), 457-467.

Commer, M., Doetsch, J., Dafflon, B., Wu, Y., Daley, T. M., & Hubbard, S. S. (2016). Time-lapse 3-D electrical resistance tomography inversion for crosswell monitoring of dissolved and supercritical CO2 flow at two field sites: Escatawpa and Cranfield, Mississippi, USA. *International Journal of Greenhouse Gas Control, 49*(Complete), 297-311. doi: 10.1016/j.ijggc.2016.03.020

Constable, S. C., Parker, R. L., & Constable, C. G. (1987). Occam's inversion: A practical algorithm for generating smooth models from electromagnetic sounding data. *Geophysics, 52*(3), 289-300.

Dahlin, T., & Zhou, B. (2004). A numerical comparison of 2D resistivity imaging with 10 electrode arrays. *Geophysical Prospecting, 52*(5), 379-398.

Daily, W., & Ramirez, A. (1995). Electrical resistance tomography during in-situ trichloroethylene remediation at the Savannah River Site. *Journal of Applied Geophysics, 33*(4), 239-249.

Daily, W., Ramirez, A., LaBrecque, D., & Nitao, J. (1992). Electrical resistivity tomography of vadose water movement. *Water Resources Research, 28*(5), 1429-1442.

Danielsen, B. E., & Dahlin, T. (2010). Numerical modelling of resolution and sensitivity of ERT in horizontal boreholes. *Journal of Applied Geophysics, 70*(3), 245-254. doi: 10.1016/j.jappgeo.2010.01.005

De Franco, R., Biella, G., Tosi, L., Teatini, P., Lozej, A., Chiozzotto, B., Giada, M., Rizzetto, F., Claude, C., & Mayer, A. (2009). Monitoring the saltwater intrusion by time lapse electrical resistivity tomography: The Chioggia test site (Venice Lagoon, Italy). *Journal of Applied Geophysics, 69*(3), 117-130.

Deng, Y., Shi, X., Xu, H., Sun, Y., Wu, J., & Revil, A. (2017). Quantitative assessment of electrical resistivity tomography for monitoring DNAPLs migration–Comparison with high-resolution light transmission visualization in laboratory sandbox. *Journal of Hydrology, 544*, 254-266.

Dey, A., & Morrison, H. F. (1979). Resistivity modeling for arbitrarily shaped three-dimensional structures. *Geophysics, 44*(4), 753-780.

Drysdale, D. (2011). Spontaneous Ignition within Solids and Smouldering Combustion. *An Introduction to Fire Dynamics, Third Edition*, 317-348.

Ebrahimzadeh, M., Tsourlos, P., & Gerhard, J.I. (2017). Self-potential for monitoring soil remediation by smoldering: proof of concept. *Near Surface Geophysics*, In press.

Gaylor, D. W., Culp, S. J., Goldstein, L. S., & Beland, F. A. (2000). Cancer Risk Estimation for Mixtures of Coal Tars and Benzo(a)pyrene. *Risk Anal., 20*(1), 81.

Giordano, N., Arato, A., Comina, C., & Mandrone, G. (2017). Time-lapse electrical resistivity imaging of the thermally affected zone of a Borehole Thermal Energy Storage system near Torino (Northern Italy). *Journal of Applied Geophysics, 140*(Complete), 123-134. doi: 10.1016/j.jappgeo.2017.03.015

Hadden, R. M., Rein, G., & Belcher, C. M. (2013). Study of the competing chemical reactions in the initiation and spread of smouldering combustion in peat. *Proceedings of the Combustion Institute, 34*(2), 2547-2553.

Haslam, E. P., Gunn, D. A., Jackson, P. D., Lovell, M. A., Aydin, A., Prance, R. J., & Watson, P. (2014). Novel laboratory methods for determining the fine scale electrical resistivity structure of core. *Journal of Applied Geophysics, 111*, 384-392.

Hermans, T., Nguyen, F., Robert, T., & Revil, A. (2014). Geophysical Methods for Monitoring Temperature Changes in Shallow Low Enthalpy Geothermal Systems, Energies, 7, 5083–5118.

Hermans, T., Wildemeersch, S., Jamin, P., Orban, P., Brouyère, S., Dassargues, A., & Nguyen, F. (2015). Quantitative temperature monitoring of a heat tracing experiment using cross-borehole ERT. *Geothermics, 53*(Complete), 14-26.

Heron, G., Carroll, S., & Nielsen, S. G. (2005). Full-Scale Removal of DNAPL Constituents Using Steam-Enhanced Extraction and Electrical Resistance Heating. *Groundwater Monit. Rem., 25*(4), 92.

Heron, G., Parker, K., Galligan, J., & Holmes, T. C. (2009). Thermal Treatment of Eight CVOC Source Zones to Near Nondetect Concentrations. *Groundwater Monit. Rem., 29*(3), 56.

ITRC. (2011). Integrated DNAPL Site Strategy. *Interstate Technology & Regulatory Council, Integrated DNAPL, IDSS-1*(Washington, DC: Site Strategy Team).

Johnson, T. C., Versteeg, R. J., Day-Lewis, F. D., Major, W., & Lane, J. W. (2015). Time-Lapse Electrical Geophysical Monitoring of Amendment-Based Biostimulation. *Groundwater, 53*(6), 920-932.

Karaoulis, M., Kim, J.-H., & Tsourlos, P. (2011). 4D active time constrained resistivity inversion. *Journal of Applied Geophysics, 73*(1), 25-34.

Karaoulis, M., Tsourlos, P, Kim, J.-H., & Revil, A.. (2014). 4D time-lapse ERT inversion: introducing combined time and space constraints. *Near Surface Geophysics*, 12, 25-34

Kavanaugh, M. C., Rao, P. S., & Wood, A. L. (2003). The DNAPL remediation challenge: is there a case for source depletion? *U.S. Environmental Protection Agency, Washington, DC, EPA/600/R-03/143*.

Kim, J.-H., Supper, R., Tsourlos, P., & Yi, M.-J. (2013). Four-dimensional inversion of resistivity monitoring data through Lp norm minimizations. *Geophysical Journal International, 195*(3), 1640-1656.

Kim, J.-H., Yi, M.-J., Park, S.-G., & Kim, J. G. (2009). 4-D inversion of DC resistivity monitoring data acquired over a dynamically changing earth model. *Journal of Applied Geophysics, 68*(4), 522-532.

Kim, K.-J., & Cho, I.-K. (2011). Time-lapse inversion of 2D resistivity monitoring data with a spatially varying cross-model constraint. *Journal of Applied Geophysics, 74*(2), 114-122.

Kinsman, L., Torero, J. L., & Gerhard, J. I. (2017). Organic liquid mobility induced by smoldering remediation. *J Hazard Mater, 325*, 101-112.

Kueper, B. H., & Davies, K. (2009). *Assessment and Delineation of DNAPL Source Zones at Hazardous Waste Sites*.

Kueper, B. H., Stroo, H. F., Vogel, C. M., & Ward, C. H. (2014). *Chlorinated solvent source zone remediation*: Springer.

LaBrecque, D. J., Ramirez, A. L., Daily, W. D., Binley, A. M., & Schima, S. A. (1996). ERT monitoring of environmental remediation processes. *Measurement Science and Technology, 7*(3), 375-383.

LaBrecque, D. J., & Yang, X. (2001). Difference inversion of ERT data: A fast inversion method for 3-D in situ monitoring. *Journal of Environmental & Engineering Geophysics, 6*(2), 83-89.

Lane, J. W., Day-Lewis, F. D., & Casey, C. C. (2006). Geophysical monitoring of a field-scale biostimulation pilot project. *Groundwater, 44*(3), 430-443.

Lekmine, G., Auradou, H., Pessel, M., & Rayner, J. L. (2017). Quantification of tracer plume transport parameters in 2D saturated porous media by cross-borehole ERT imaging. *Journal of Applied Geophysics, 139*(Complete), 291-305.

Loke, M. H. (2013). Tutorial: 2-D and 3-D electrical imaging surveys.

Loke, M.H., T. Dahlin, and D.F. Rucker. 2014. Smoothness-constrained time-lapse inversion of data from 3-D resistivity surveys. *Near Surface Geophysics*, 12(1): 5-24.

Loke, M. H., Wilkinson, P. B., Chambers, J. E., Uhlemann, S. S., & Sorensen, J. P. R. (2015). Optimized arrays for 2-D resistivity survey lines with a large number of electrodes. *Journal of Applied Geophysics, 112*, 136-146.

Lundegard, P. D., & LaBrecque, D. (1995). Air sparging in a sandy aquifer (Florence, Oregon, USA): Actual and apparent radius of influence. *Journal of Contaminant Hydrology, 19*(1), 1-27.

Mao, D., Revil, A., Hort, R. D., Munakata-Marr, J., Atekwana, E. A., & Kulessa, B. (2015). Resistivity and self-potential tomography applied to groundwater remediation and contaminant plumes: Sandbox and field experiments. *Journal of Hydrology, 530*, 1-14.

Masy, T., Caterina, D., Tromme, O., Lavigne, B., Thonart, P., Hiligsmann, S., & Nguyen, F. (2016). Electrical resistivity tomography to monitor enhanced biodegradation of hydrocarbons with Rhodococcus erythropolis T902. 1 at a pilot scale. *Journal of Contaminant Hydrology, 184*, 1-13.

Miller, C. R., Routh, P. S., Brosten, T. R., & McNamara, J. P. (2008). Application of time-lapse ERT imaging to watershed characterization. *Geophysics, 73*(3), G7-G17.

Mussett, A. E., & Khan, M. A. (2000). *Looking into the earth: an introduction to geological geophysics*: Cambridge University Press.

Newmark, R. L., Daily, W. D., Kyle, K. R., & Ramirez, A. L. (1998). Monitoring DNAPL pumping using integrated geophysical techniques. *Journal of Environmental and Engineering Geophysics, 3*(1), 7-13.

Nguyen, F., Kemna, A., Antonsson, A., Engesgaard, P., Kuras, O., Ogilvy, R., Gisbert, J., Jorreto, S., & Pulido-Bosch, A. (2009). Characterization of seawater intrusion using 2D electrical imaging. *Near Surface Geophysics, 7*(5-6), 377-390.

Ohlemiller, T. J. (1985). Modeling of smoldering combustion propagation. *Progress in Energy and Combustion Science, 11*(4), 277-310.

Ohlemiller, T. J., & Lucca, D. A. (1983). An experimental comparison of forward and reverse smolder propagation in permeable fuel beds. *Combustion and Flame, 54*(1-3), 131-147.

Pironi, P., Switzer, C., Gerhard, J. I., Rein, G., & Torero, J. L. (2011). Self-Sustaining Smoldering Combustion for NAPL Remediation: Laboratory Evaluation of Process Sensitivity to Key Parameters. *Environ. Sci. Technol., 45*(7), 2980.

Pironi, P., Switzer, C., Gerhard, J. I., Rein, G., Torero, J. L., & Fuentes, A. (2009). Small-Scale Forward Smouldering Experiments for Remediation of Coal Tar in Inert Media. *Proc. Combust. Inst., 32*(2), 1957.

Power, C. (2014). Electrical resistivity tomography for mapping subsurface remediation.

Power, C., Gerhard, J. I., Karaoulis, M., Tsourlos, P., & Giannopoulos, A. (2014). Evaluating four-dimensional time-lapse electrical resistivity tomography for monitoring DNAPL source zone remediation. *J Contam Hydrol, 162-163*, 27-46.

Power, C., Gerhard, J. I., Tsourlos, P., Soupios, P., Simyrdanis, K., & Karaoulis, M. (2015). Improved time-lapse electrical resistivity tomography monitoring of dense non-aqueous phase liquids with surface-to-horizontal borehole arrays. *Journal of Applied Geophysics, 112*, 1-13.

Ramirez, A., Daily, W., LaBrecque, D., Owen, E., & Chesnut, D. (1993). Monitoring an underground steam injection process using electrical resistance tomography. *Water Resources Research, 29*(1), 73-87.

Rashwan, T. L. (2015). Self-Sustaining Smouldering Combustion as a Novel Disposal Destruction Method for Waste Water Biosolids.

Rashwan, T. L., Gerhard, J. I., & Grant, G. P. (2016). Application of self-sustaining smouldering combustion for the destruction of wastewater biosolids. *Waste Management, 50*, 201-212.

Rein, G. (2009). Smouldering Combustion Phenomena in Science and Technology. *International Review of Chemical Engineering, 106*(1–2), 1957.

Revil, A., Karaoulis, M., Johnson, T., & Kemna, A. (2012). Some low-frequency electrical methods for subsurface characterization and monitoring in hydrogeology. *Hydrogeology Journal, 20*(4), 617-658.

Salman, M., Gerhard, J. I., Major, D. W., Pironi, P., & Hadden, R. (2015). Remediation of trichloroethylene-contaminated soils by star technology using vegetable oil smoldering. *J Hazard Mater, 285*, 346-355.

Samouëlian, A., Cousin, I., Tabbagh, A., Bruand, A., & Richard, G. (2005). Electrical resistivity survey in soil science: a review. *Soil and Tillage research, 83*(2), 173-193.

Schmidt-Hattenberger, C., Bergmann, P., Labitzke, T., Wagner, F., & Rippe, D. (2016). Permanent crosshole electrical resistivity tomography (ERT) as an established method for the long-term CO2 monitoring at the Ketzin pilot site. *International Journal of Greenhouse Gas Control, 52*(Complete), 432-448.

Scholes, G. C., Gerhard, J. I., Grant, G. P., Major, D. W., Vidumsky, J. E., Switzer, C., & Torero, J. L. (2015). Smoldering Remediation of Coal-Tar-Contaminated Soil: Pilot Field Tests of STAR. *Environmental Science & Technology, 49*(24), 14334-14342.

Slater, L., & Binley, A. (2003). Evaluation of permeable reactive barrier (PRB) integrity using electrical imaging methods. *Geophysics, 68*(3), 911-921.

Slater, L., & Binley, A. (2006). Synthetic and field-based electrical imaging of a zerovalent iron barrier: Implications for monitoring long-term barrier performance. *Geophysics, 71*(5), B129-B137.

Slater, L., Binley, A. M., Daily, W., & Johnson, R. (2000). Cross-hole electrical imaging of a controlled saline tracer injection. *Journal of Applied Geophysics, 44*(2), 85-102.

Slater, L. D., & Lesmes, D. (2002). IP interpretation in environmental investigations. *Geophysics, 67*(1), 77-88.

Sparrenbom, C. J., Åkesson, S., Johansson, S., Hagerberg, D., & Dahlin, T. (2017). Investigation of chlorinated solvent pollution with resistivity and induced polarization. *Science of the Total Environment, 575*, 767-778.

Switzer, C., Pironi, P., Gerhard, J. I., Rein, G., & Torero, J. L. (2009). Self-Sustaining Smoldering Combustion: A Novel Remediation Process for Non-Aqueous-Phase Liquids in Porous Media. *Environ. Sci. Technol., 43*, 5871.

Tikhonov, A. N., Goncharsky, A. V., Stepanov, V. V., & Yagola, A. G. (2013). *Numerical methods for the solution of ill-posed problems* (Vol. 328): Springer Science & Business Media.

Tildy, P., Neducza, B., Nagy, P., Kanli, A. I., & Hegymegi, C. (2017). Time lapse 3D geoelectric measurements for monitoring of in-situ remediation. *Journal of Applied Geophysics, 136*, 99-113.

Torero, J. L., & Fernandez-Pello, A. C. (1996). Forward smolder of polyurethane foam in a forced air flow. *Combust. Flame, 106*(1–2), 89.

Tsourlos, P. (1995). Modelling, interpretation and inversion of multielectrode resistivity survey data.

Tsourlos, P., Ogilvy, R., Meldrum, P., & Williams, G. (2003). Time-lapse monitoring in single boreholes using electrical resistivity tomography. *Journal of Environmental & Engineering Geophysics, 8*(1), 1-14.

Wang, S., Lee, M., Park, M. K., & Kim, J.-M. (2010). Box experiments on monitoring the CO 2 migration in a homogeneous medium using electrical resistivity survey. *Geosciences Journal, 14*(1), 77-85.

Wilkinson, P. B., Meldrum, P. I., Kuras, O., Chambers, J. E., Holyoake, S. J., & Ogilvy, R. D. (2010). High-resolution Electrical Resistivity Tomography monitoring of a tracer test in a confined aquifer. *Journal of Applied Geophysics, 70*(4), 268-276.

Wilkinson, P. B., Uhlemann, S. S., Chambers, J. E., Meldrum, P. I., Oxby, L. S., & Kuras, O. (2006, 2013). *Optimised sequential experimental design for geoelectrical resistivity monitoring surveys*.

Yi, M.-J., Kim, J.-H., & Chung, S.-H. (2003). Enhancing the resolving power of least-squares inversion with active constraint balancing. *Geophysics, 68*(3), 931-941.

Chapter 3

3. Time-lapse Electrical Resistivity Tomography for mapping in situ smouldering remediation (STAR)

3.1. Introduction

Historically, industrial contaminants have been released into the subsurface due to poor waste management and industrial practices. Even though waste management practices have significantly improved, accidents still occur. Dense non-aqueous phase liquids (DNAPLs) are contaminants that are immiscible with and denser than water, such as coal tar, creosote and chlorinated solvents. When released into the subsurface, DNAPLs often migrate below the water table, acting as persistent sources of groundwater contamination that impose consequences to human health and the environment (Gaylor et al., 2000; Kueper & Davies, 2009; Kueper et al., 2014). Coal tar is a complex mixture of long-chain hydrocarbons, such as aliphatic and aromatic compounds, with relatively high viscosity (20-100 centipoises) and density (1010 kg/m^3); these properties make coal tar a challenging contaminant to be remediated in situ (Kueper et al., 2014). As a result, the common approach for coal tar source zones is excavation and ex-situ disposal of contaminated soil to a hazardous waste landfill or incinerator (Scholes et al., 2015). An innovative technology called Self-sustaining Treatment for Active Remediation (STAR) has been developed as an in situ treatment for DNAPLs, such as coal tar (Pironi et al., 2009).

STAR employs smoldering combustion, which is an oxygen-limited, exothermic (400-1200ºC), flameless oxidation reaction on the surface of a fuel (i.e., coal tar) in a porous medium (i.e., soil) (Pironi et al., 2009; Switzer et al., 2009; Pironi et al., 2011; Scholes et al., 2015). Figure 3-1 (bottom) illustrates the field application of in situ STAR. An ignition point (IP, a 5-cm carbon steel well) is employed to start the smoldering reaction. The IP is screened across a 0.3 m interval known to coincide with DNAPL. During the heating period, hot (~500ºC) air is injected through the screened interval, boiling off water and heating the DNAPL and soil immediately adjacent to the IP. Once ignition occurs, as evidenced by a spike in temperature

and production of combustion gases, the heater is turned off while air injection is maintained (Scholes et al., 2015). Then, the thin (tens of centimeters) propagation front moves outwards from the IP; the reaction is typically self-sustaining due to the exothermic reaction and convective transfer of heat to adjacent DNAPL (Pironi et al., 2009; Scholes et al., 2015). The reaction converts the DNAPL to primarily CO_2, CO, water, and heat (Pironi et al., 2009; Switzer et al., 2009; Kinsman et al., 2017). The clean soil behind the front slowly cools and is later re-infiltrated by groundwater typically after the air injection is terminated (Kinsman et al., 2017). Vapor extraction points (VEPs) extract the gases and treat them on site (Scholes et al., 2015). The heating period is typically on the order of a few hours, while the self-sustained smouldering phase is on the order of days to weeks (Scholes et al., 2015). The front velocity is typically on the order of tens of centimeters per day and the radius of influence of a single well is on the order of several meters (Scholes et al., 2015).

A full-scale STAR system was implemented at an industrial site contaminated with coal tar in Newark, New Jersey (Figure 3-1, top). Two pilot tests, one shallow and one deep, were previously conducted and are fully documented in Scholes et al. (2015). For both the pilot (Scholes et al., 2015) and the full-scale application, system performance is assessed by (i) temperatures obtained from multi-point thermocouple bundles, (ii) cumulative mass of coal tar destroyed estimated from continuously monitored CO and CO_2 in the vapour capture system, and (iii) pre- and post-treatment coring for soil sampling. As with all DNAPL remediation assessments, collecting such data is not only expensive, but mostly sparse and discrete both in space and time (Kavanaugh et al., 2003). Non-invasive monitoring that provides information on the removal of DNAPL over time would be a valuable component to determine the efficiency, performance and success of any remediation (Kavanaugh et al., 2003; Halihan et al., 2005; Power et al., 2014; Power et al., 2015).
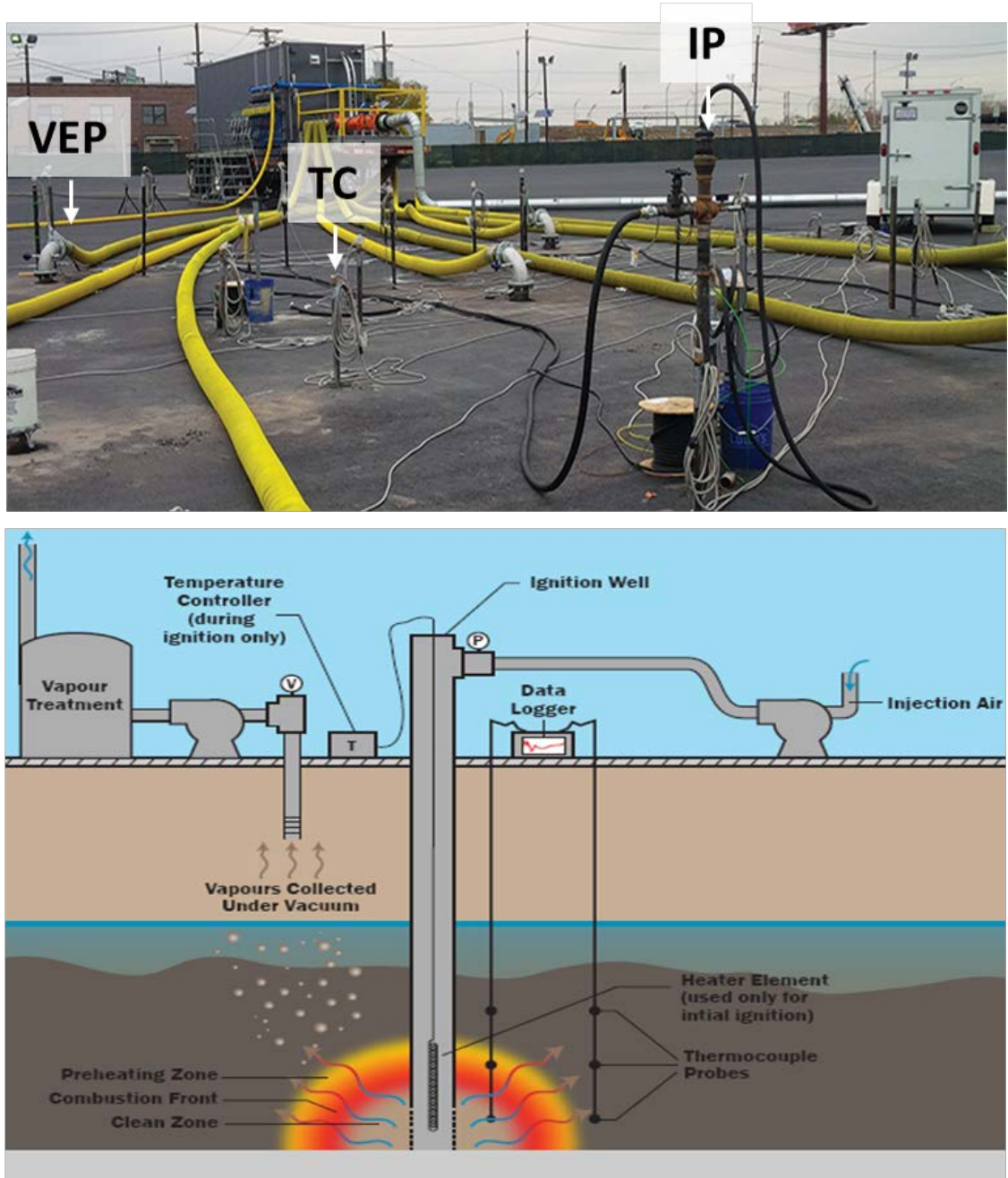
Figure 3-1. (Top) STAR installation in the field, showing vapor extraction points (VEPs), ignition points (IPs) and thermocouples (TC) installed. (Bottom) Conceptual design of a STAR treatment. Main processes of a smouldering treatment are named (clean dry zone, combustion front, preheating zone), as well as main installations (IPs, VEPs and thermocouples) (Scholes et al., 2015).

Geophysical methods have been recently used to complement aspects of environmental assessment, characterization and remediation of contaminated sites. Electrical Resistivity

Tomography (ERT), a geoelectrical method, has a wide range of applications from environmental assessment and hydrogeological characterization (Daily et al., 1992; Daily & Ramirez, 1995; Atekwana et al., 2000; Slater et al., 2000; Miller et al., 2008; Lekmine et al., 2017) to mapping contaminant distribution in soil and groundwater (Newmark et al., 1998; Clément et al., 2011; Power et al., 2014; Deng et al., 2017). Time-lapse ERT has shown significant potential with advances in inversion algorithms (LaBrecque & Yang, 2001; Kim et al., 2009; Karaoulis et al., 2011; Power et al., 2014). Time-lapse ERT has been used to monitor aqueous contaminant plumes (Daily et al., 1992; Daily & Ramirez, 1995; Chandra et al., 2011), permanganate injections for in situ chemical oxidation (Mao et al., 2015; Tildy et al., 2017), bioremediation (Johnson et al., 2015; Masy et al., 2016; Sparrenbom et al., 2017), iron permeable reactive barriers (Slater & Binley, 2003), and zero valent iron oxidation (Slater & Binley, 2006) with research covering laboratory, pilot and field scales. Studies of ERT applied to thermal remediation are limited and focused on electrical resistance heating (Ramirez et al., 1993; LaBrecque et al., 1996). However, ERT applications to DNAPL remediation are very rare and, to the author's knowledge, no field study has employed ERT for directly evaluating the loss of DNAPL mass during remediation.

An ERT survey involves repeatedly injecting direct current through surface (or in-borehole) electrodes and measuring the potential differences at other electrodes, generating data that is inverted to estimate the spatial distribution of subsurface resistivity (Samouëlian et al., 2005; Revil et al., 2012). The setup of the survey line(s) determines the breadth and depth of the subsurface tomographic image(s). Time-lapse ERT involves collecting multiple images of the same target and isolating changes that occur over time, which is particularly useful for removing the influences of geology from the images.

Resistivity changes in the subsurface in both time and space are primarily caused by changes in groundwater and soil chemistry, water saturation, porosity and temperature. The relationship between electrical resistivity, water saturation, porosity and water and soil properties is described by a modified version of Archie's Law for coarse grains (Samouëlian et al., 2005):

$$\rho = a\rho_w\phi^{-m}S_w^{-n} \hspace{3cm} (\textbf{Equation 1})$$

where ρ (ohm·m) is the electrical resistivity of the formation (bulk resistivity), ρ_w (ohm·m) is the resistivity of the conducting fluid (most commonly groundwater, saline water or an aqueous solution), ϕ is the porosity of the rock and S_w is the saturation (or proportion of pore space) occupied by the conducting fluid (water). The values of empirical parameters *a*, *m* and *n* determined by experimental laboratory methods or through numerical modelling, and are related to pore morphology (Samouëlian et al., 2005; Haslam et al., 2014).

In remediation and environmental sciences, the increase in resistivity with decreasing water saturation (Equation 1) has been utilized in a number of subsurface investigations with ERT, including mapping air sparging remediation (Lundegard & LaBrecque, 1995; LaBrecque et al., 1996) and CO_2 sequestration monitoring (Wang et al., 2010; Carrigan et al., 2013; Commer et al., 2016; Schmidt-Hattenberger et al., 2016). For the same reason, but acting in reverse (i.e., conductive water replacing a non-conductive fluid), time-lapse ERT has been demonstrated, with numerical modelling, to exhibit high potential for mapping DNAPL remediation (Power et al., 2014; Power et al., 2015).

It is recognized that heating has a complicated impact on bulk resistivity. The effect of liquid (i.e., water, oils) temperature changes on resistivity has been used for ERT to map geothermal sources (Hermans et al., 2014), track groundwater flow via seasonal temperature variations (Hermans et al., 2015; Giordano et al., 2017), monitor steam flooding for oil recovering (Tøndel et al., 2014) and study heat/steam injection to volatilize organic contaminants (Ramirez et al., 1993). It is known that as water heats, resistance to current decreases. However, in cases in which water saturation changes simultaneously (i.e., saturation decreases due to boiling water or water displacement by air), the increased presence of air impedes current. A relationship for how the formation resistivity changes with saturation and temperature (up to and including boiling temperatures) changing simultaneously is (Ramirez et al., 1993):

$$r = \frac{\rho_{(T_2)}}{\rho_{(T_1)}} = \left(\frac{S_{w2}}{S_{w1}}\right)^{-2} \times \left(\frac{T_1}{T_2}\right) \qquad \text{(\textbf{Equation 2})}$$

where T_1 (°F) and T_2 (°F) are temperatures at time 1 and time 2, respectively, S_{w1} and S_{w2} are the water saturation at time 1 and time 2, respectively, and *r* is the ratio of the resistivity at

time=2, $\rho_{(T2)}$, to resistivity at time=1, $\rho_{(T1)}$. Figure 3-2 shows r as a function of S_{w2}, assuming S_{w1}=1 (i.e., initially water saturated subsurface); each curve represents a different amount of temperature change. The T_1/T_2=1 curve isolates the influence of saturation, illustrating a five-fold increase in resistivity ($r > 1$) with a 50% decrease in water saturation. Examining the S_{w2}=1 axis isolates the effect of temperature, showing that approximately 3-fold ($T_1/T2$=0.3) and then 30-fold ($T_1/T2$=3) heating causes resistivity to decrease by factors of 0.3 and 3 respectively. Note that T_1/T_2=0.3 represents the transition from ambient to water boiling temperatures (in degrees Fahrenheit). The figure illustrates that, in this case, the overall resistivity will decrease (i.e., heating effect dominates) when S_{w2}>0.55 and it will increase (i.e., saturation effect dominates) when S_{w2}<0.55. The T_1/T_2=0.03 case represents more extreme heating, although it is acknowledged that this may be out of the range of validity of Equation 2. In this case, heating dominates causing a decreased overall resistivity until S_{w2} decreases below 0.20 (i.e., the soil approaches residual water saturation).

These simultaneous temperature and saturation changes are relevant when interpreting ERT in the context of thermal remediation; for example, volatilization of organic contaminants with heat/steam injection causing both contaminants and water to evaporate (Ramirez et al., 1993). In addition, applicability of ERT in electrical resistance heating (Newmark et al., 1994; LaBrecque et al., 1996) demonstrated the use of time-lapse ERT to monitor decreases in resistivity of 40-60% as temperatures increased to water boiling with an increase in resistivity at higher temperatures. It is important to note that the influences on resistivity are more complex than Equation 2, for example, high resistivity could be observed by the presence of DNAPLs and aqueous contaminants (typically resistive, see Power et al., 2014) in the pore space filled with water (typically conductive). However, with increased temperatures, both DNAPLs and water become more conductive, creating decreased resistivity anomalies. When DNAPLs or water reach their boiling points, resistivity is expected to increase due to decreased saturations and generation of gases, which are resistive.
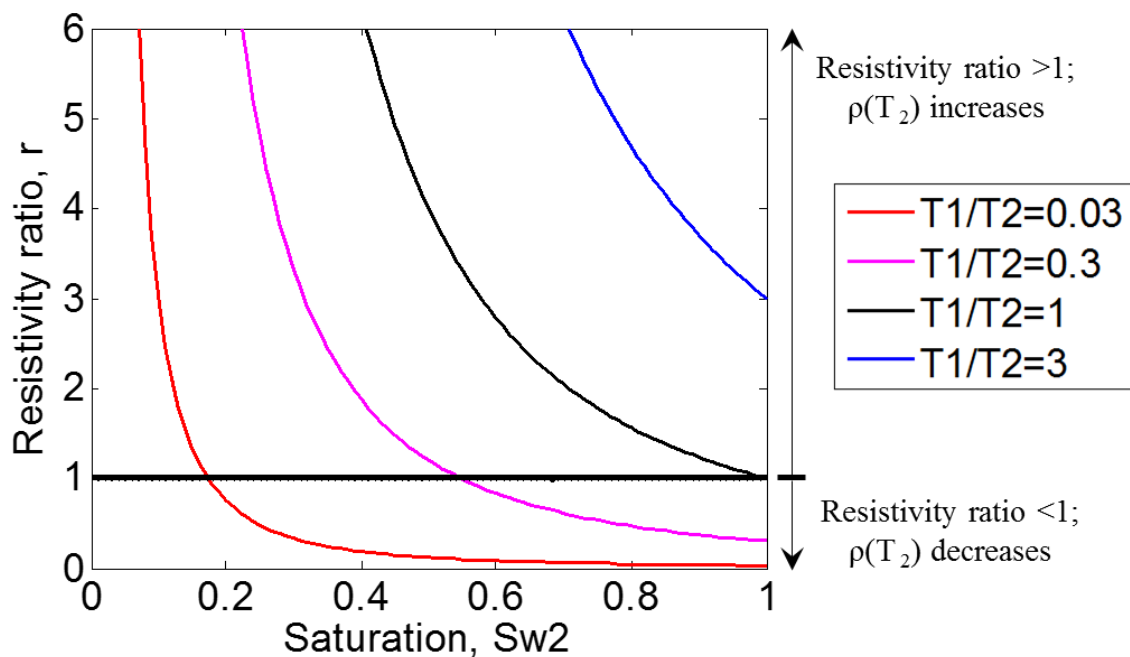
Figure 3-2. Theoretical changes in soil resistivity with simultaneous changes in temperature and water saturation. Specifically, resistivity ratio (r) at T_2 and S_{w2}, as defined in Equation 2, as a function of water saturation at time=2. All points are relative to $S_{w1}=1$ at time=1. Curves represent temperature ratios, where $T_1/T_2=1$ means no temperature change.

It is hypothesized that STAR can be tracked with time-lapse ERT. The main processes occurring during STAR (see Figure 3-1) which are expected to impact electrical resistivity include (i) increasing soil and soil moisture temperatures near the IP during the heating phase, (ii) boiling of water near the IP, (iii) changes in water saturation related to injected air physically displacing water near the IP and air migration above the treatment zone, (iv) changes in water saturation related to generation and upwards migration of combustion gases in and above the treatment zone, (v) a growing dry, treated region as the STAR front expands, and (vi) groundwater re-infiltrating the treated region after air injection is terminated. While STAR clearly represents a complicated target to monitor geoelectrically, it is hypothesized that the dominant influence will be increasing subsurface resistivity corresponding to the growing treated (i.e., dry, DNAPL-free) zone.

The goal of this research was to evaluate the effectiveness of monitoring STAR by using time-lapse ERT under real field conditions. This study conducted two pilot field tests of surface-

based, time-lapse ERT during full scale application of STAR at a coal tar contaminated site. One shallow and one deep STAR treatment zone was surveyed during remediation with "swiss cross" two-dimensional survey lines. 4D time-lapse inversion (Kim et al., 2009; Kim & Cho, 2011; Kim et al., 2013) was used to analyze local, slice, and global results of resistivity and resistivity ratios providing novel insights into the subsurface processes occurring during STAR. This geophysical data was correlated to in situ temperature and gas data as well as post-treatment direct evidence of remediation. This provides, for the first time, insight into ERT for complementary monitoring of an in situ DNAPL thermal remediation process.

3.2. Field site and STAR operation

The field site is a 15-hectare property in Newark, New Jersey that was previously a chemical manufacturing plant. The geology of the site important for this work consists of (i) an asphalt cover, (ii) a recently placed layer of gravel (0-3 meters; Columbia layer), (iii) the historical fill layer (less than 6 meters below ground surface; Fill) which is highly heterogeneous and consists of sand, gravel, rock, ash, brick, wood, metal, glass and trash, (iv) a semi-confining layer of silt, clay and peat (0 - 9.5 meters thick; Meadow Mat); and (v) a sand and silt layer (up to 10 meters thick, Alluvium). The site is heavily contaminated with coal tar, which source zones are located mainly in the Fill layer and the Alluvium. Coal tar layers are identified for treatment with coring and TarGOST® (Tar-specific Green Optical Screening Tool) profiling, a screening technique for coal tar. A number of adjacent IPs, grouped into a "cell", are ignited at once to treat a targeted portion of a treatment unit by STAR. Cells are subjected to STAR consecutively and concurrently, so that treatment progresses step-wise across the site. ERT was applied to a single cell targeting coal tar at an average depth of 2.8 meters below ground surface (mbgs) in the Fill, hereafter referred to as the "shallow cell", and to a single cell targeting coal tar at an average depth of 7.8 mbgs in the Alluvium, hereafter the "deep cell".

The deep cell was in the footprint of a former coal tar disposal lagoon, while the shallow cell was in the surroundings of the lagoon. Each cell consisted of (i) 5 to 10 ignition points with screens installed at the desired depth of treatment; (ii) multi-point thermocouple bundles installed 0.3 m from each IP (four temperature sensors installed at the depth of the IP screen with 0.2 m vertical spacing; and (iii) 6 to 8 VEPs that collect vapors produced during combustion. The operation of the shallow and deep cells is summarized below. More details

43

on the installation of each cell is in Appendix A. Smouldering combustion is expected when temperatures profiles at one IP exceed boiling temperatures and a sharp increase in temperature is observed, combined with increased concentration of combustion gases (CO_2 and CO) collected at the VEPs (Scholes et al., 2015).

3.2.1. Shallow cell STAR operation

Figure 3-3 shows the design of the shallow cell, with five IPs (IP1 to IP5), five thermocouples bundles (each located 0.3 meters, in plan-view, from an IP), and eight VEPs. The red circles represent the average expected treatment radius for each ignition (2 m in the shallow cell). None is shown for IP2 because this well was clogged and therefore abandoned. The two ERT lines are also shown in the figure. STAR was applied to the shallow cell from August 13 to 21, 2016. The main operational steps are listed in time steps *(a)-(f)* in Table 3-1. While many ERT images were generated (details below), only a select number are included for detailed discussion; these are also listed in Table 3-1. Time 0 (t_0) refers to the onset of collecting the reference ERT image, here taken as just after a test ignition at only IP1. By taking all time-lapse data relative to this reference, the influences caused by initial air injection and heating of IP1 are neglected. Note that the IP1heater had already been turned off and temperatures around IP1 had decreased to ambient levels when the reference image was taken. Air injection was consistent during this period, only increasing afterwards.
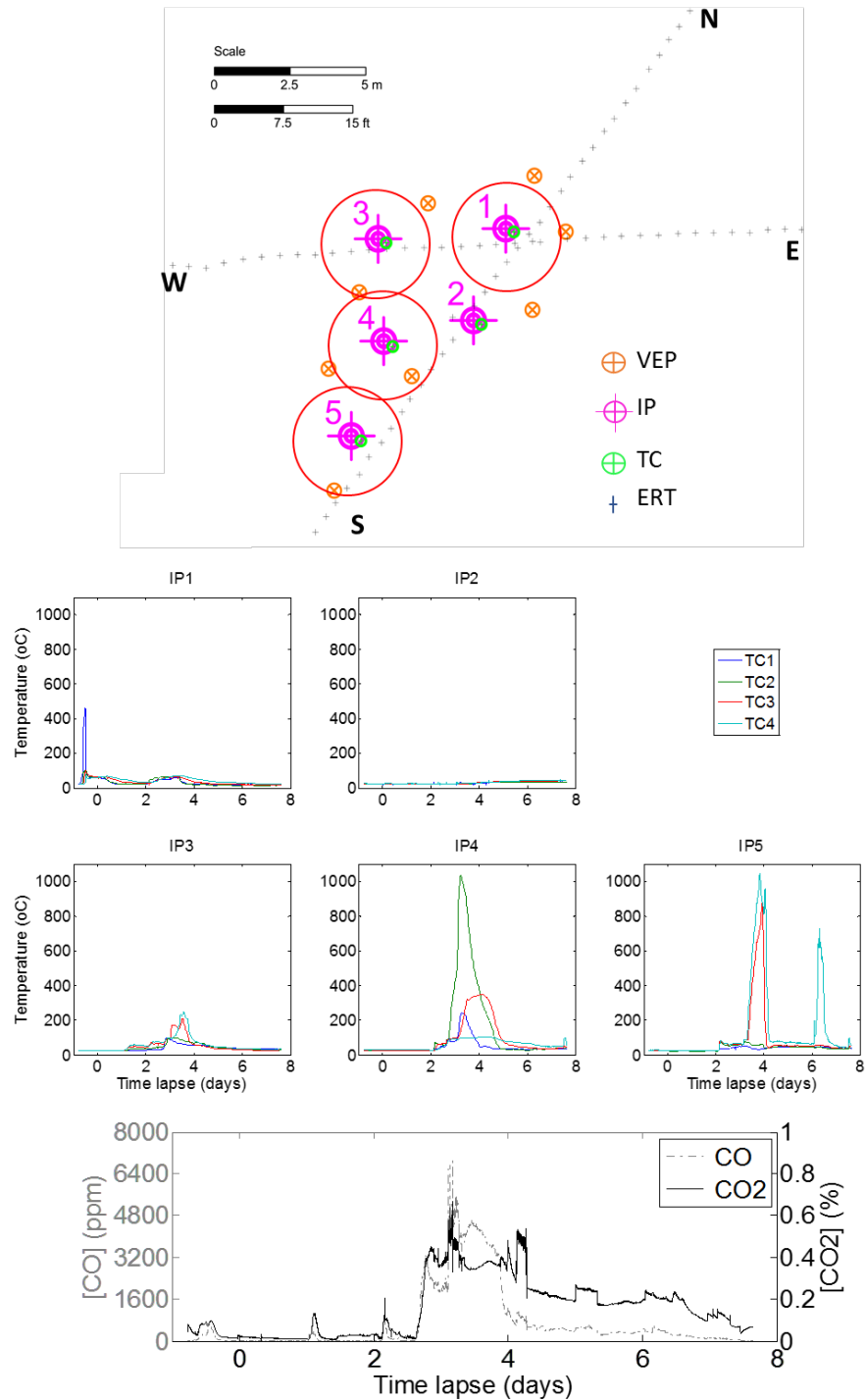
Figure 3-3. (Top) Shallow treatment cell design. Red circles indicate the average expected treatment radius. VEP=vapor extraction point; IP=ignition point; TC=thermocouples; ERT= electrodes. (Bottom) Temperature profiles for all IPs (4 points per IP) and CO_2 and CO data generated during treatment of the shallow cell for all VEPs. TC1 is in the bottom of the screen.

Table 3-1. Sequence of Events and ERT Images in Treatment of the Shallow Cell

Time-step	Description	Time relative to t_0 (days)
-	VEPs on	-
-	IP1 heater on	-
	Image t0 (ref)	*0.00*
(a)	IP1 heater off	0.28
(b)	IP3 heater on	1.02
	Image t1	*1.39*
(c)	Air and heaters off - VEPs on	1.44
	Image t2	*2.00*
(d)	All heaters on (except IP2)	2.04
	Image t3	*2.34*
	Image t4	*2.67*
	Image t5	*3.04*
(e)	All heaters off	3.36
	Image t6	*4.85*
	Image t7	*6.36*
(f)	Air off	7.46
	Image t8	*7.94*

3.2.2. Deep cell STAR operation

Figure 3-4 shows the design of the deep cell, with six IPs (IP1 to IP6), six adjacent thermocouple bundles, and six VEPs. The red circles illustrate the average expected 3 m radius of influence for each ignition in the deep cell (Scholes et al., 2015). The two ERT lines are also shown in the image. STAR was applied to the deep cell from August 24 to September 02, 2016. The main operational steps were conducted in steps(a)-(e) as shown in Table 3-2. The table also lists the time of key ERT images to be discussed. Time 0 (t_0) is taken just before ignition of IP4, thus neglecting the heating phase of this well in the time-lapse analysis. This was done because the influences of the heating phase were relatively small considering the entire changes in the subsurface after the ignition. Boiling temperatures were not reached yet, therefore changes in saturation due to boiling are still going to alter the images. Air injection was stabilized and low, however they increase overtime.
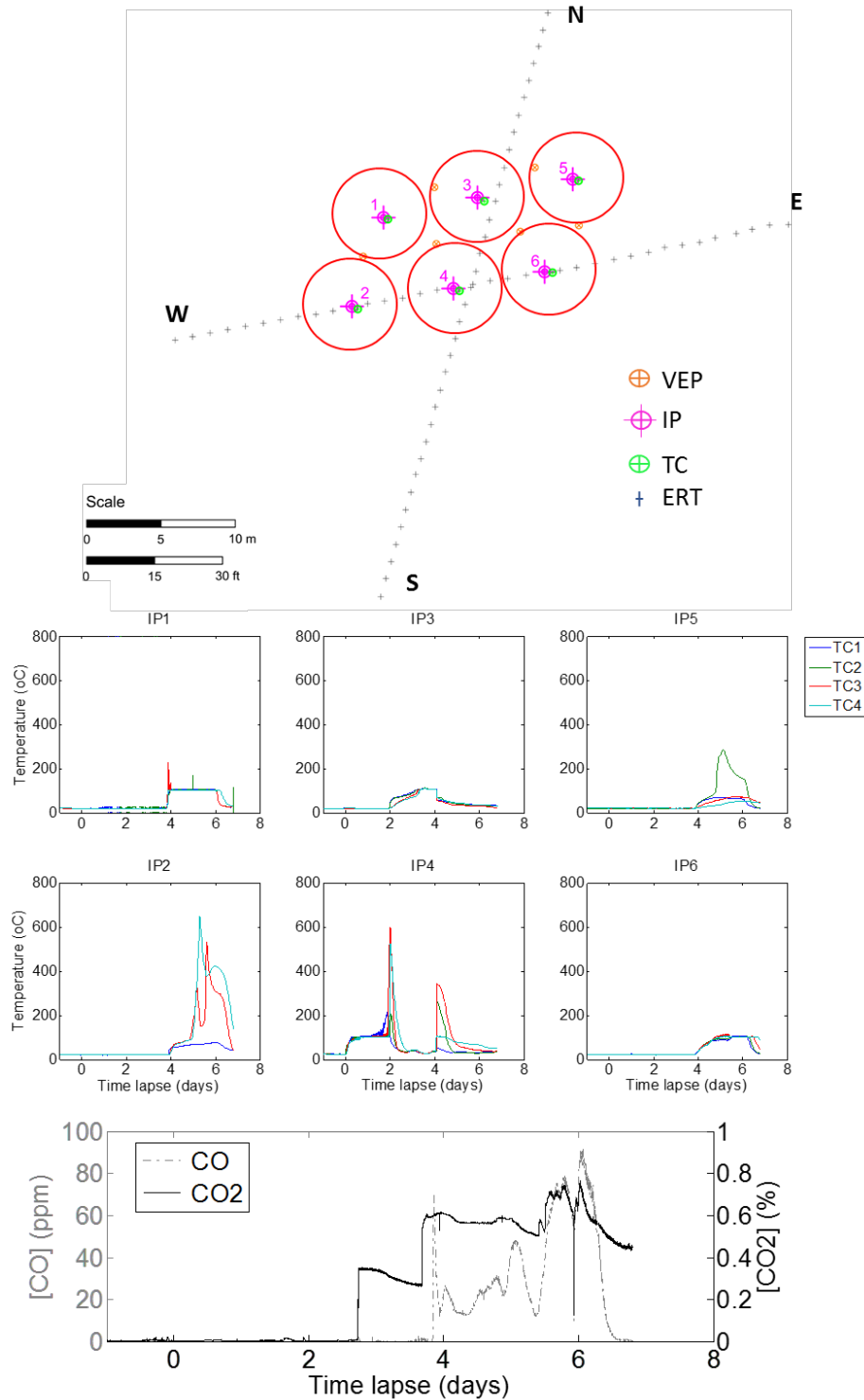
Figure 3-4. (Top) Deep cell design. Red circles indicate the average expected treatment radius of influence. VEP=vapor extraction point; IP=ignition point; TC=thermocouples; ERT= electrodes. (Bottom) Temperature profiles for all IPs and CO_2 and CO concentration generated for all VEPs during treatment of the deep cell. TC1 is in the bottom of the screen.

Table 3-2. Sequence of Events and ERT Images in Treatment of the Deep Cell

Time-step	Description	Time relative to t_0 (days)
-	VEPs on	-
-	Air on	-
-	IP-04 heater on	-
	Image t0 (ref)	*0.00*
	Image t1	*1.65*
(a)	IP-04 heater off	1.83
(b)	IP-03 heater on	1.85
	Image t2	*2.12*
	Image t3	*2.63*
	Image t4	*3.38*
(c)	All heaters on	3.77
	Image t5	*4.14*
	Image t6	*5.83*
(d)	All cell heaters off	6.04
	Image t7	*6.50*
(e)	Air off	6.80
	Image t8	*7.80*

3.3.   ERT field work

3.3.1. ERT Installation and Operation

Two approximately perpendicular surface lines of 36 stainless steel electrodes were installed in each cell. Each electrode (0.6 m long for shallow cell and 1.5 m long for deep cell) was hammered 15 cm into the top of the historical Fill after inserting it in a hole drilled through the Columbia Fill; afterwards these holes were filled with sand, water and bentonite and then sealed with tar at the asphalt surface. Contact resistance was measured to be approximately 0.5

Kohms in both cells, indicating good contact between the electrodes and the surrounding soil (more information on installation of electrodes in Appendix B). The ERT lines installed at the surface of the deep cell are shown in Figure 3-5.

In the shallow cell, the 21 m lines (Figure 3-3) used 0.6 m spacing, designed for a target 2.4 mbgs. In the deep cell, the 42 m lines used 1.2 m spacing aiming at a target 7.2 mbgs (Figure 3-4). The skew of the lines from perpendicular was intentional to best match the installation of the IPs (Figures 3-3 and 3-4). A resistivity meter (Syscal Pro, Iris Instruments) was used to collect resistivity measurements using self-made cables connected to a self-made switch box (details in Appendix B). The resistivity meter was connected to a laptop for remote data acquisition using *Comsys* software (Iris Instruments), which allowed for overnight monitoring. The set up was kept in a water and wind proof tent designed for daily and overnight measurements (details in Appendix B). During STAR, one dipole-dipole ERT (n=2a) data set was collected approximately every hour per line; each had 561 measurements that filled 315 inversion blocks. Approximately 250 data sets per line were collected over the treatment period. For the shallow cell, data collection for each line required 6-10 minutes; while for the deep cell, each line required 15-20 minutes.

Background resistivity surveys were conducted using independent inversion (i.e., not time-lapse) prior to STAR to evaluate geolgical units and to detect any interference from IPs, thermocouples and VEPs. The dipole-dipole array was selected because it decreased the data collection time, as well as provided better vertical to horizontal resolution compared to other arrays tested, such as multi-gradient.
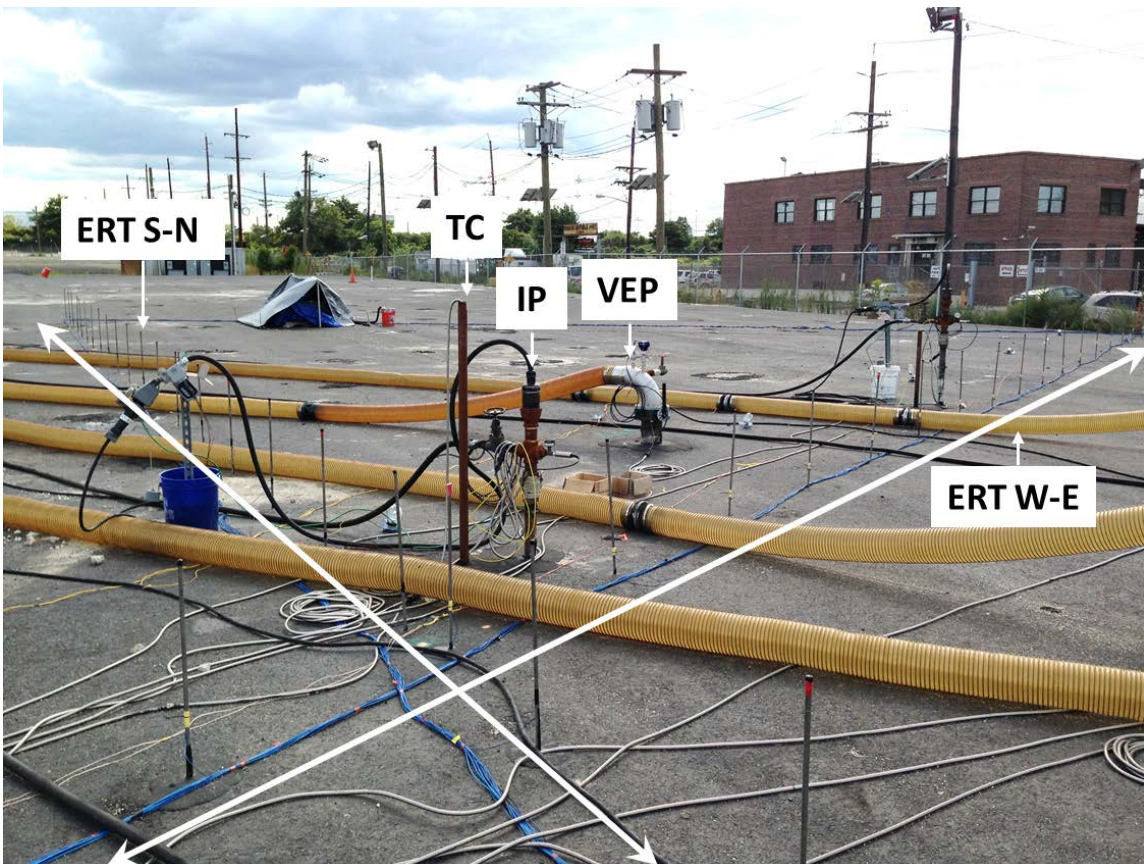
Figure 3-5. Photograph of the surface of the deep cell showing STAR operations equipment and ERT lines**.**

3.3.2. Inversion

To convert the raw apparent resistivity data into true resistivity values, an inversion algorithm specially developed for time lapse ERT data was used. The inversions were conducted using DC_2DPRO (Kim et al., 2009; Kim & Cho, 2011; Kim et al., 2013). The software's algorithm is known as 4D inversion (three spatial dimensions plus time) although, in this case, only two spatial dimensions were used, plus time. Compared to previous ERT monitoring approaches, this algorithm tends to produce less time-lapse inversion artifacts. The 4D inversion algorithm defines the entire resistivity data set in both space and time (space-time domain), allowing the data sets measured at different times to be inverted simultaneously, by introducing both space and time regularization constraints. The algorithm performs the inversion iteratively trying to find a spatial-temporal subsurface resistivity model which best fits the entire ERT monitoring data within the given constrains. In Kim et al. (2013), regularizations are introduced to the software to produce L_1 and L_2 norm minimizations for both space and time domains, as well

as in the inversion roughness. The L_1 norm minimization assumes a Laplace or exponential distribution, while L_2 norm minimization assumes a normal distribution. For more information on the inversion algorithm and regularization, see Kim et al. (2009), Kim & Cho (2011), and Kim et al. (2013).

3.3.3. Data analysis

The data analysis was performed in steps. First, all 250 images taken per line were inverted using the 4D inversion approach (2D plus time), simultaneously. By performing this step, it was observed that the changes through each image were continuous and smooth overtime, as well as repeatable between lines, therefore, from the 250 inversions per line, approximately 50 images per line (41 for the shallow cell and 56 for the deep cell) were chosen for time-lapse analysis. These 50 images per line were chosen to reduce the amount of processing, still considering the repeatability of the images in time (see Appendix D). All 50 images per line had relatively high quality and were selected to highlight changes over time, based on key STAR operation steps. Approximately 6% of the data were rejected (from 561 measurements points per image), to reduce the RMS (root mean square) error of the inversion images. The percentage of data rejection for the inversion results were chosen after tests were conducted with rejection of 6%, 8%, 10% and 15% of the data set. It was shown that after rejecting around 10% of the inversion points, the RMS stabilized within acceptable ranges (10-17%).

The individual data point rejection resulted in a smaller RMS error that was maintained in the range of 10-12% for the shallow cell and 13-17% for the deep cell. A full L2 norm minimization (for time and space domain and model roughness) was chosen, because it depicted smooth time-lapse changes which were compatible with STAR operations (temperature and gas concentration); see Appendix C for details of the tests evaluating how well the different regularization inversion results fit ground truth. The regularization parameters in space and time domain for the inversion are decided automatically by the program with every iteration (Kim et al., 2009; Kim et al., 2013, Yi et al., 2003) and for the initial limit values (minimum and maximum) of the regularization parameters the program defaults were used. Appendix C shows the parameters used for the regularizations. Finally, ratio images between each time-lapse image (t1, t2, …) and a reference image (t0) were produced (Kim et al., 2013; Power et al., 2014; Power et al., 2015) to highlight the actual

resistivity difference between the baseline (t0) and each successive monitoring step during remediation.

3.4. Results

3.4.1. ERT for Shallow Cell STAR treatment

First, it is useful to review the direct observations about STAR performance in the shallow cell. Figure 3-3 shows all four thermocouples for each IP. Apart from tests conducted in IP1, which resulted in a rapid temperature spike without CO_2 generation, smouldering is indicated at IP3, IP4, and IP5 with extended burns at the latter two. Note that these temperatures are adjacent to the well, and a decrease in temperature after ignition does not mean the reaction has ended, but more likely that it has propagated outwards. Evidence for this is in the combustion gas concentration data (Figure 3-3, bottom), lasting much longer than the peak temperatures.

The background survey was conducted with independent inversion. Background surveys are ideal for identifying subsurface geology, therefore, Figure 3-6 shows the background images plotted along with the core log information taken at each IP (more detailed core logs provided in Appendix A). Low contact resistance and RMS error for the S-N and W-E lines (13% and 14%, respectively) in these images are both indicators of good data quality; this is important considering the many sources of static interference (e.g., metal IPs, metal VEPs). Figure 3-6 reveals a shallow resistive layer (~190 ohm·m) up to 1.5 mbgs is observed to correlate to the historical Fill layer. A conductive region (4-50 ohm·m) from 1.5 to 6 mbgs is observed and can be attributed to three main layers and interferences: (i) it is known that the groundwater level is at 1.5 mbgs within the Fill layer (groundwater data available in Appendix A); (ii) the Meadow Mat layer (~20 ohm·m), which starts at 3.5 mbgs, as shown by the cores; and (iii) the metal IPs that correspond to static, vertical anomalies exhibiting low resistivity (~ 0-4 ohm·m). The high conductivity shown for metal IPs is not surprising since laboratory experiments with metal pipes revealed similar anomalies in ERT scans (Appendix E).
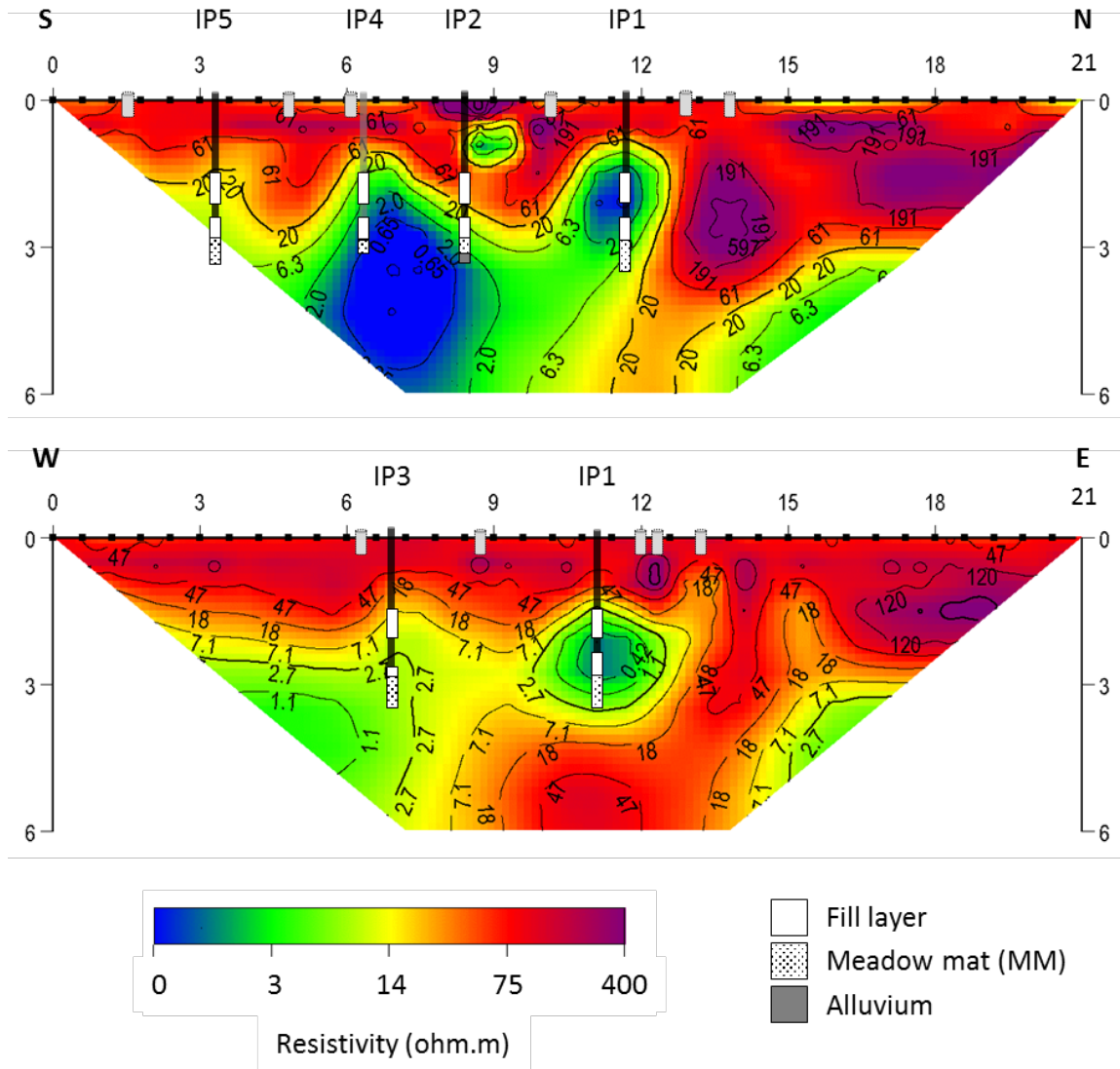
Figure 3-6. S-N and W-E cross sections of ERT background independent inversion (filtered). IP4 is in grey because it is offset ~2m from the ERT line. Smaller grey cylinders represent vapor extraction points (VEPs). Core logs for each IP were plotted in the inverted images.

3.4.1.1. 4D Time-lapse inversions and ratios

From the 41 inverted images selected for analysis (shown in Appendix D), nine are reproduced here and represent the main changes that occurred during STAR treatment. Although the images had smooth transition between each other in the data set of 41 images, these nine images are meant to represent different phases of STAR, as shown in Table 3-1. The generated images of subsurface resistivity are shown in Figure 3-7. Changes in resistivity during the treatment can be observed throughout the images in both S-N and W-E lines for the time-lapse

inversion images in Figure 3-7, and in the ratio images shown in Figure 3-8. Images shown in Figure 3-7 demonstrate consistent inversion results over time with limited inversion artifacts in comparison to the independent inversions, as expected. This provides confidence in the data and analysis methodology. Detailed changes in resistivity over time, however, are more obvious in the ratio images (Figure 3-8). It is important to notice that in the ratio images, the difference between each image seems to be drastic, however these images where picked from a set of 41 smoother inversion changes that depict a more continuous transition.
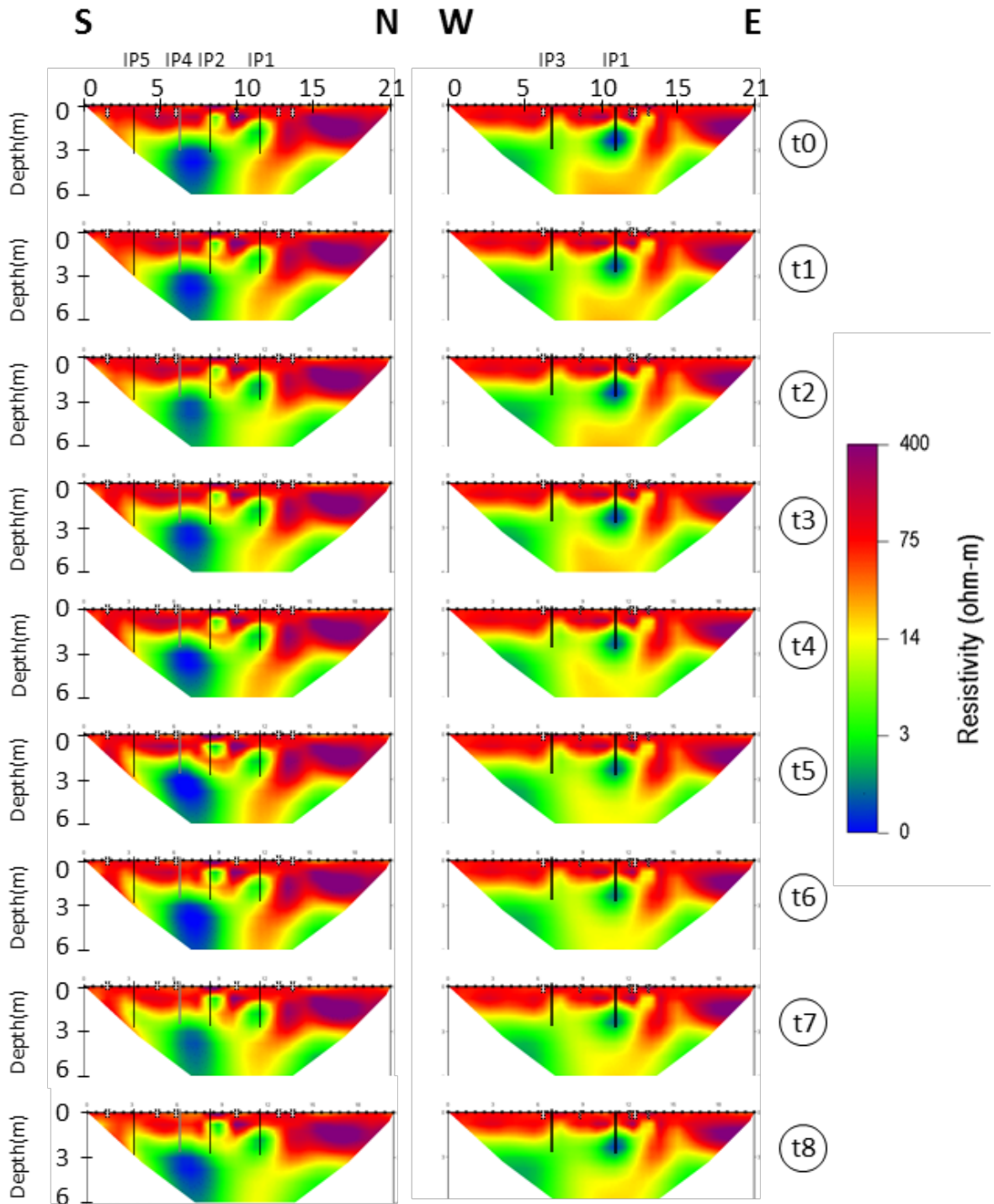
Figure 3-7. Selected 4D time-lapse images, using full L_2-norm minimization for the shallow cell for both lines S-N and W-E. IPs are shown in each image, as well as VEPs (gray cylinders). Time steps are t0 to t8 and specific times are shown in Table 3-1. Axes are in meters.

The ratio images, using t0 as a reference (Figure 3-7), are presented from t1-t8 in Figure 3-8a and 3-8b for line S-N and W-E, respectively. The figure reveals that localized changes can be as high as 2.3 times more or as low as 0.4 times less resistive than the reference image. Figures 3-8c-e provide other site measurements to compare with the resistivity changes over time. The time-varying average resistivity value over the entire cross-section is shown in Figure 3-8c for each line, considering 41 images obtained during the operation. Figure 3-8d provides the temperatures measured at one depth for the three IPs identified as exhibiting a smouldering reaction (IP3, IP4, and IP5). The CO_2 concentration (Figure 3-8e) collected by the VEPs installed in the study area indicates an indirect measurement of the coal tar destruction rate, as combustion gases can only be generated by combustion of organic contaminant. To further clarify the sequence of events, Figure 3-8c-e identifies when each image, t1-t8, occurred and uses coloured bars to indicate key steps in the operation (see figure caption and Table 3-1).

Figure 3-8 provides unique insights into the performance of STAR. Local increases in resistivity are initially observed around well screens when air injection is initiated. For example, at the screen elevation of IP1 and IP3 for Line W-E (t1, Figure 3-8b) and IP5 and IP1 in Line S-N (t1, Figure 3-8a). This is true whether the heaters are active or not; the IP5 heater was not on but a small air flux was active to prevent groundwater flooding the in-well heaters. This initial increase in resistivity is likely due to physical displacement (i.e., drainage) of water in the porous medium (Equation 1).

At the same time, for locations being preheated, a local decrease in resistivity corresponds to increasing temperature. For example, this is observed at IP3 (t2, Figure 3-8b) and IP4 (t2, Figure 3-8a). This behaviour is consistent with Equation 2. Preheating is not restricted to the vicinity of wells since a preheating region advances ahead of the smouldering reaction when it propagates; this is observed by the growing areas of decreased resistivity, for example around IP4 and IP5 (t2-t5, Figure 3-8a).

When boiling temperatures are reached (Figure 3-8d), resistivity increases are observed while water saturation changes due to water vapourization in the regions near the IPs. For example, IP1 and IP3 in Line W-E (t3-t4, Figure 3-8b) and IP5 in Line S-N (Figure 3-8a). This change

56

is expected, as seen in Equation 1. This effect is not apparent for IP4 despite its boiling temperatures, likely because this IP is 2 m offset from the S-N survey line.

After boiling, the temperatures for IP3, IP4, IP5 accelerate considerably (Figure 3-8d), indicating beginning of the smouldering reaction; this is confirmed by the CO_2 concentration increase (Figure 3-8e). An increase in resistivity is expected corresponding to the generation of combustion gases, air injection and the growth of dry, treated zones created when the smouldering reaction propagates outwards from the IPs. This is observed in the resistivity images; for example, in t5-t7, in both lines, the magnitude of the resistivity ratios increase as do the size of the resistive regions. During t6-t7 in both lines, it is clear from the gas data that the smouldering reactions continues to spread away from the IPs, showing temperature decreases in the areas where the smouldering reaction already occurred. The increased resistivity regions extend laterally in these images (t6-t7, Figure 3-8a-b), suggesting that the ERT data is helpful in visualizing this spread. Comparing the burns associated with IP4 and IP5 are helpful in this context. They ignited at approximately the same time (Figure 3-8d), but since IP4 is offset from the ERT survey it is observed that the decreased resistivity associated with preheating lasts longer (t3-t5), and the resistivity increase associated with boiling/smouldering arrives later (t6-t7).

It is expected that after termination of air injection and release of the air seal at the ignition well, groundwater rapidly re-infiltrates the Fill unit. This is confirmed by observed decreases in resistivity in the ratio images. For example, image t2 at Line S-N (Figure 3-8a) where a temporary shutdown turned off air injection in IP1 and IP3. More dramatically, it is observed in both lines at t8, confirming that the re-infiltration happens soon after shutdown.

Throughout the system operation, VEPs (grey cylinders, Figure 3-8a and 3-8b) are on, capturing gases generated by the smouldering reactions. It is observed that near the VEPs in the images, the resistivity is always increased, such as in Line S-N (Figure 3-8a) between 10.5 m and 15.75 m. Thus, the images give some indication of the vapour capture zones. It is also possible to observe increasing resistive regions where no reaction is expected, such as Line W-E from 15.75 m to 21.0 m (Figure 3-8b) and Line S-N in the region of the abandoned IP2

(Figure 3-8a). It is hypothesized that these regions have trapped gases that were not collected with the VEPs.

The evolution of the average resistivity in the entire ERT section is shown in Figure 3-8c. It illustrates that the magnitude of resistivity increases during combustion (i.e., after 2.5 days) are significantly greater than during unheated or heated air injection (days 1 to 2.5). In addition, it is found that changes in the average resistivity for line S-N parallels the CO_2 concentration (Figure 3-8e). However, the average resistivity is a bulk measurement that is sensitive to temperature changes, combustion gas generation, DNAPL removal and air displacement of fluids. In Figure 3-8c, an increase in resistivity is observed that coincides with the beginning of the smouldering reaction and generation of combustion gases (represented by temperature and CO_2 concentration). This increased resistivity is maintained throughout the time that combustion gases are being generated. This suggests that the DNAPL destruction rate by smouldering is related to the overall increase in resistivity. The same degree signals are not shown in line W-E (Figure 3-8c), likely because IP4 and IP5 (on the S-N line) are responsible for most of coal tar treatment and thus CO_2.

a)

b)

Resistivity ratio

0.4   0.7   1.0   1.6   2.3
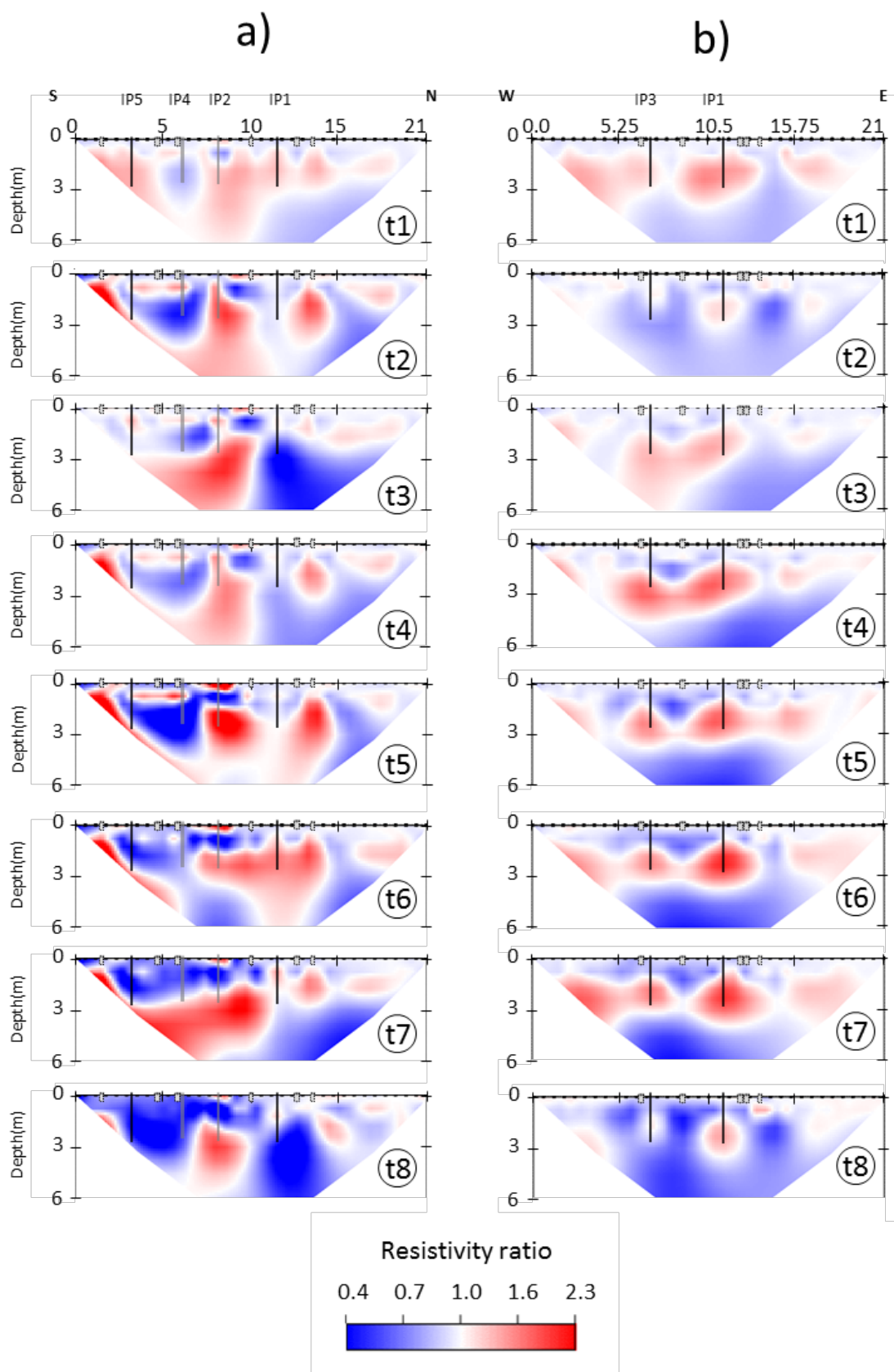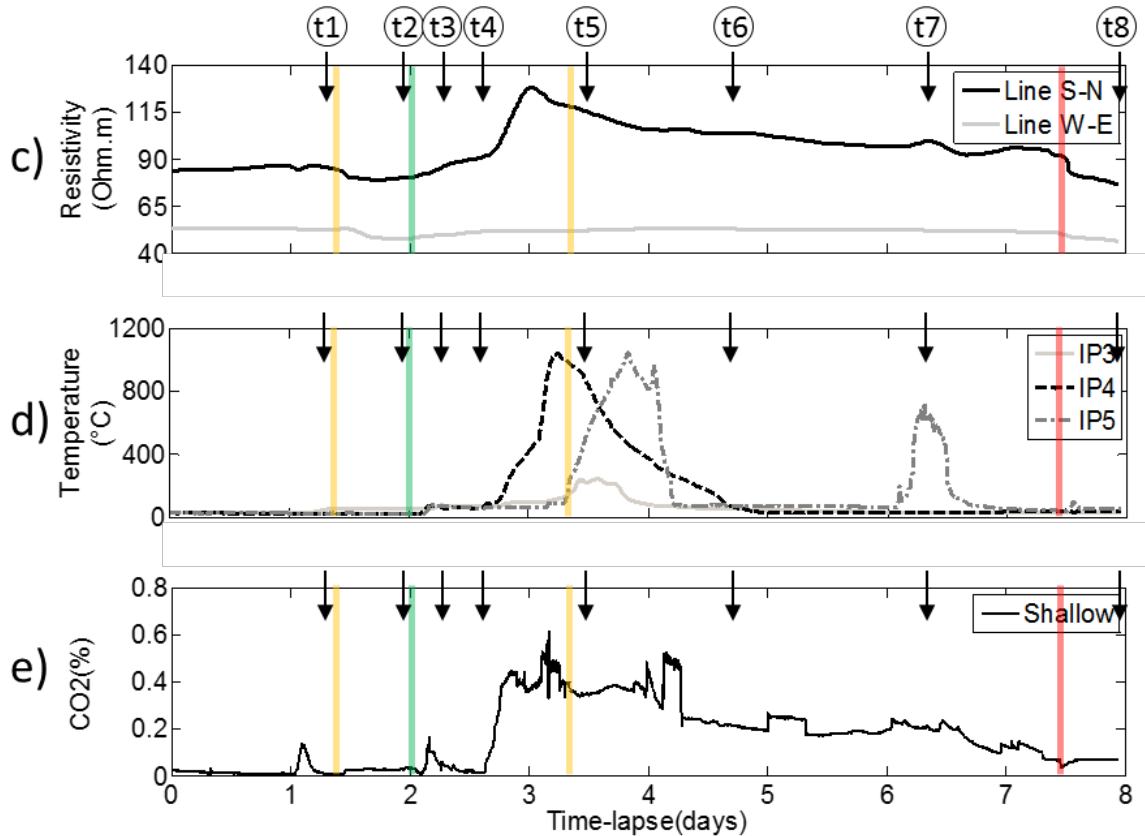
Figure 3-8. Selected resistivity ratio images for the shallow cell (axes are distances in m): a) S-N line, b) W-E line. In addition, (c) Average resistivity value of all images, d) temperature for a single depth (near bottom of IPs) if IP3, IP4 and IP5 (S-N); and e) CO_2 concentration for the vapor extraction system. Times of the ratio images indicated with black arrows. Colour bars represent system operation including: orange bars for temporary system shutdown, green bar for system restart, and red bar for system shutdown (details in Table 3-1).

3.4.1.2. Focused analysis of the shallow cell

A focused analysis was conducted to identify resistivity trends over time in individual nodes within the 41 images from the shallow cell. This was possible in the shallow cell only due to the higher resolution (close electrode spacing, shallow depth) of the survey (example of sensitivity analysis in Appendix F). This was accomplished by extracting 4D inversion results without interpolation between the inversion blocks obtained by DC2D_Pro, as seen in Figure 3-9a (Kim et al., 2009; Kim & Cho, 2011; Kim et al., 2013), within the expected radii of influence for each IP and analysing the resistivity trends in *MATLAB*. Analysing individual nodes for resistivity trends has been undertaken previously, but mostly in laboratory studies

(Masy et al., 2016; Lekmine et al., 2017). To the best of the author's knowledge, this is the first time this technique has been employed for analysing field data.

Figure 3-9 presents the focused analysis for IP4 and IP5 on the S-N line. It is important to notice that IP5 is in the limit of the image's resolution, therefore the examples are focused between IP4 and IP5. More graphical examples on IP3 (Line W-E) and IP1 (Line S-N and W-E) can be seen in Appendix G. Figure 3-9a presents the background (reference) independent inversion image shown in Figure 3-6, but without interpolation, allowing visualization of all 315 individual inversion blocks (i.e., nodes) collected. In Figure 3-9a, the expected radii of influence (red circles in plan-view in Figure 3-3) are represented here in cross-section as red rectangles. The expected radius of influence for each IP in the shallow cell is 2 m, and the expected treatment thickness is approximately 1 m (Scholes et al., 2015). Examples of the node-specific resistivity ratios within the radius of influence of IP4 (with some overlap from that of IP5) as a function of time (8 days of ERT monitoring) are shown by the five graphs in Figure 3-9b. These plots can be compared to temperature (Figure 3-9c) and CO_2 concentration data (Figure 3-9d) from the operation of the shallow cell.
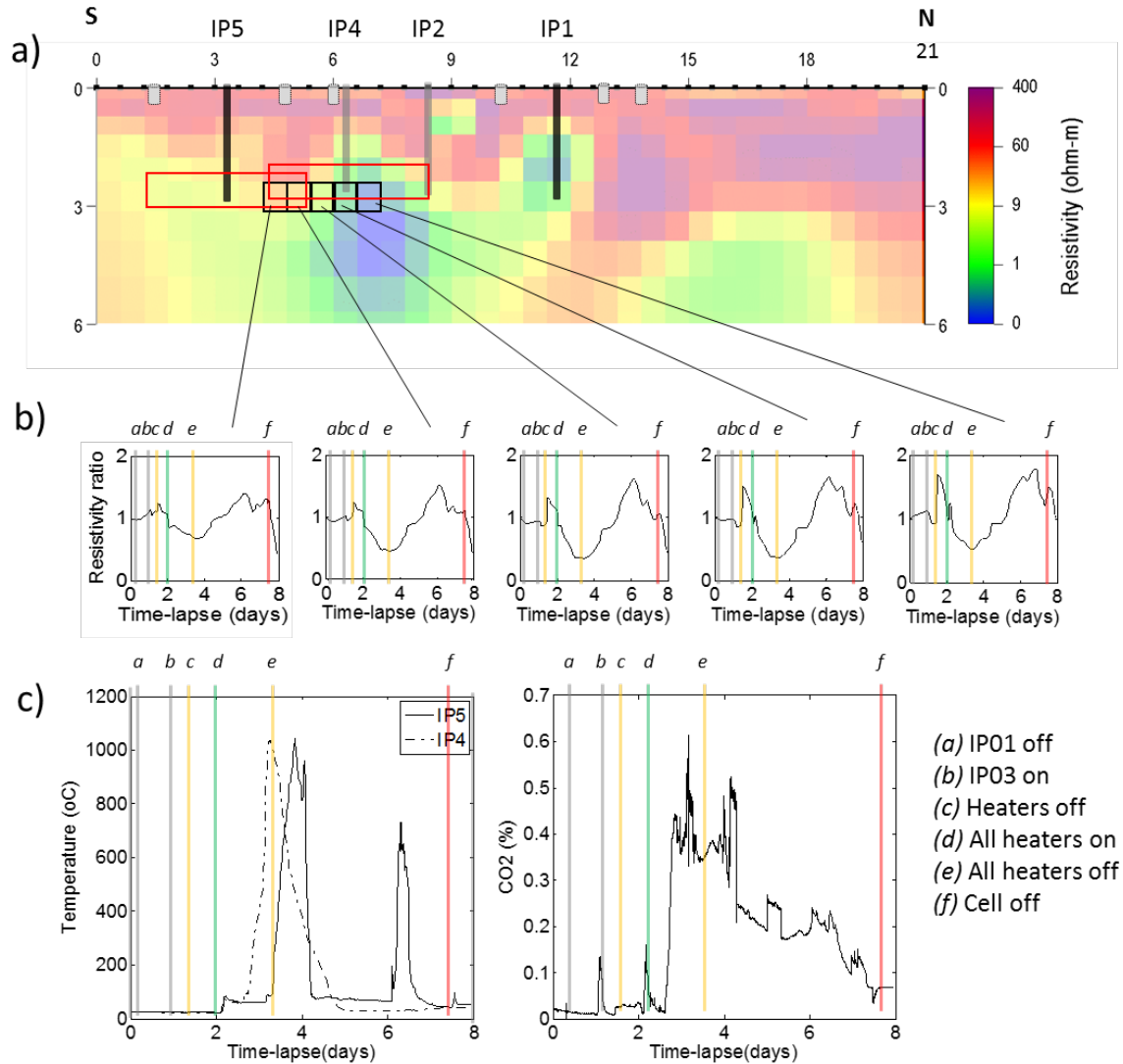
Figure 3-9. Example of focused analysis: resistivity over time in expected smouldering zone of IP4. a) Discrete values for each node in the resistivity inversions of S-N background image. Red rectangles are the expected reaction zones for IP4 and IP5. Black squares correspond to the location of each graph in b). b) Ratio resistivity values in time-lapse for nodes shown in a) compared to values in t0. *a)-f)* are time-steps as shown in legend and Table 3-1. c) Supporting graphs for temperature data for IP4 and IP5 and gas concentration.

From the discussion above, and consideration of Equation 2, it is expected that resistivity should decrease during preheating (temperature effects on water) and resistivity should increase during smouldering (decrease in water saturation). By looking at the CO_2 and temperature data (Figure 3-9c), the heating phase for IP4 and IP5 occurred in period *(d)-(e)*,

while smouldering occurred primarily during *(e)-(f)*. Indeed, the node-specific graphs confirm a negative slope in resistivity ratio during preheating, starting when the heaters are turned on, and a positive slope during combustion. This pattern is consistent throughout the nodes within the radius of influence for IP4. This suggests that this two-slope "valley" resistivity pattern may be a locally-specific indicator of smouldering.

This "valley" resistivity pattern was evaluated for all 315 nodes in the ERT images considering all times, with the results shown in Figure 3-10. If the period *(d)-(e)* exhibited a negative slope and the period *(e)-(f)* exhibited a positive slope, the node was coloured red. Overall, the red regions in Figure 3-10 attempt to identify regions where fluids (water, DNAPL) were first heated followed by an increase in air/gas saturation. The red regions were divided into three types. Type I in Figure 3-10 is the "postulated STAR treatment zone". It suggests that IP1 and IP2 exhibited no STAR treatment, which is consistent with ground truth (i.e., temperature and gas data that points to minimal combustion for IP1, and knowing IP2 was unusable). Furthermore, it supports the conclusion that IP3, IP4 and IP5 did exhibit significant treatment, which is also consistent with temperature and gas data. It further suggests that the treatment area is not necessarily uniform around the IP (e.g., IP3); this is not surprising given the heterogeneous nature of the historical Fill layer and the fact that STAR treatment follows the effective air permeability pathways (Scholes et al., 2015). Moreover, it suggests the most thorough treatment was in the space between two IPs that both exhibited a strong ignition (e.g., between IP4 and IP5). Note that treatment may exist to the south (left) of IP5, but the natural end of the ERT profile limits resolution in this area.

Regions that are red in Figure 3-10 may have other explanations. Type II areas are hypothesized to be areas that were heated and then contain injected air or gas not captured by vapour extraction system. They are likely not smouldered regions because they are distant from, or otherwise not connected to, ignition wells. Type III (Figure 3-10) areas exist within the part of the images (below 3 m) exhibiting the lowest confidence, in which node-specific analysis is likely unreliable. At such depths, such detail could be influenced by relatively low resolution and possible inversion artifacts (Sasaki, 1992; Danielsen & Dahlin, 2010). Post-treatment cores (near IP3) are available for this cell (Appendix A). However, parts of the coring

near IP3 was not recovered within the treatment region, making it difficult to identify a before and after scenario. Groundwater chemical analysis indicates treatment near IP3.
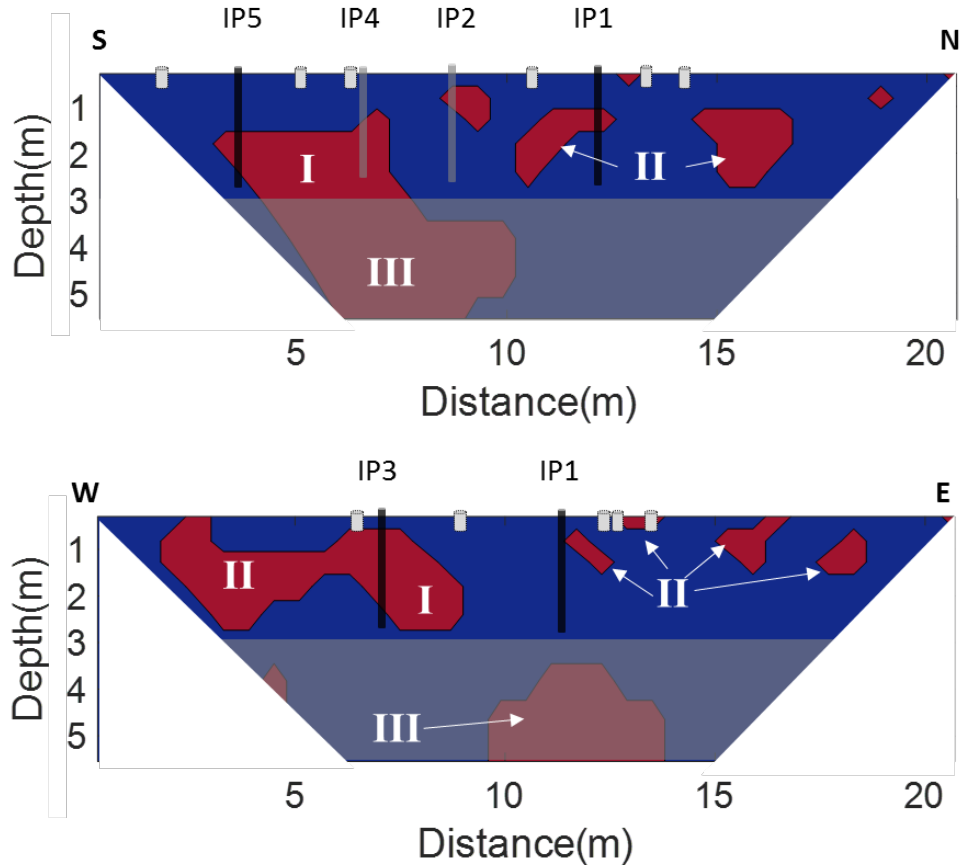
Figure 3-10. Focused analysis of lines S-N and W-E during the entire operation (8 days of time-lapse). Type I red areas indicate "postulated STAR treatment zones", while blue indicates no reaction. Type II and III red areas probably represent different types of reactions within the treatment area (see discussion in text). Grey shows low resolution regions.

3.4.2. ERT for Deep Cell STAR treatment

In the deep cell, same as with the shallow cell, not all IPs were ignited or have an influence in the ERT. In the deep cell, only IP2, IP4 and IP5 exhibited temperatures above boiling water and from those, only IP2 and IP4 were within the ranges of the ERT images (Figure 3-4), therefore, only these two IPs will be discussed in the deep cell. At almost the same time as ignition of IP4 occur, IP3 heater was turned on, followed two days after by all six heaters in the cell, as shown in Table 3-2.

The independent inversions for the background survey of the deep cell are shown in Figure 3-11. A resistive layer, observed at approximately 4.0 mbgs (~190 ohm·m), corresponds to the historical Fill layer, presenting reduced resistivity (~ 40 ohm·m) starting from 2.0 mbgs, possibly due to groundwater (Appendix A). The Meadow Mat (MM), a clay-rich layer, is identified as the less resistive layer between 4-6 mbgs. Interference generated by the metal IPs (Appendix E) is visible and may impact the apparent thickness of the MM, which is known to be around 1.2 m (between 3.6 and 4.8 mbgs, using TarGOST®, Appendix A). Below the clay layer (6 mbgs), the relatively homogeneous sand layer (Alluvium) is observed.
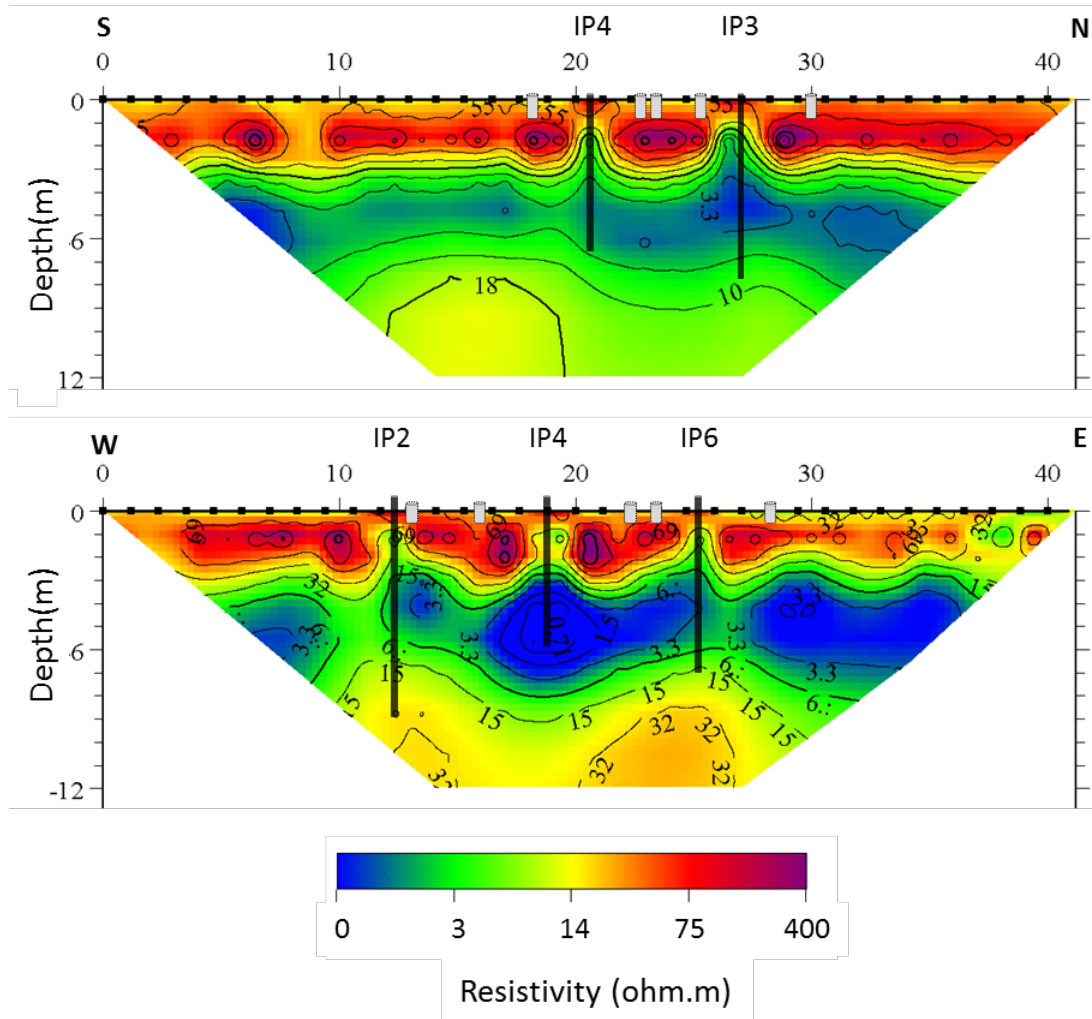
Figure 3-11. S-N and W-E cross-sections of the deep cell from ERT background independent inversion (filtered). Grey cylinders represent vapor extraction wells, black lines are ignition points, and black dots are electrode locations. Axes are distances in m.

3.4.2.1. 4D Time-lapse inversions and ratios

From the set of 50 images generated (Appendix D), nine images are presented in Figure 3-12, illustrating the main changes that occur during the deep cell STAR application. The nine images represented here identifies different phases of STAR. The time of each image compared to main events of the STAR operation were presented in Table 3-2. For both lines in the deep cell (S-N and W-E) slight changes can be detected. From t1 to t7 (Figure 3-12), both lines suggest an increase in resistivity in the Alluvium and in the historical Fill. For image t8, a decrease in resistivity is noticeable after system shutdown, similar to that observed in the shallow treatment. These images are not ideal for seeing differences, but rather demonstrate overall consistency and confidence in the ERT scans acquired.
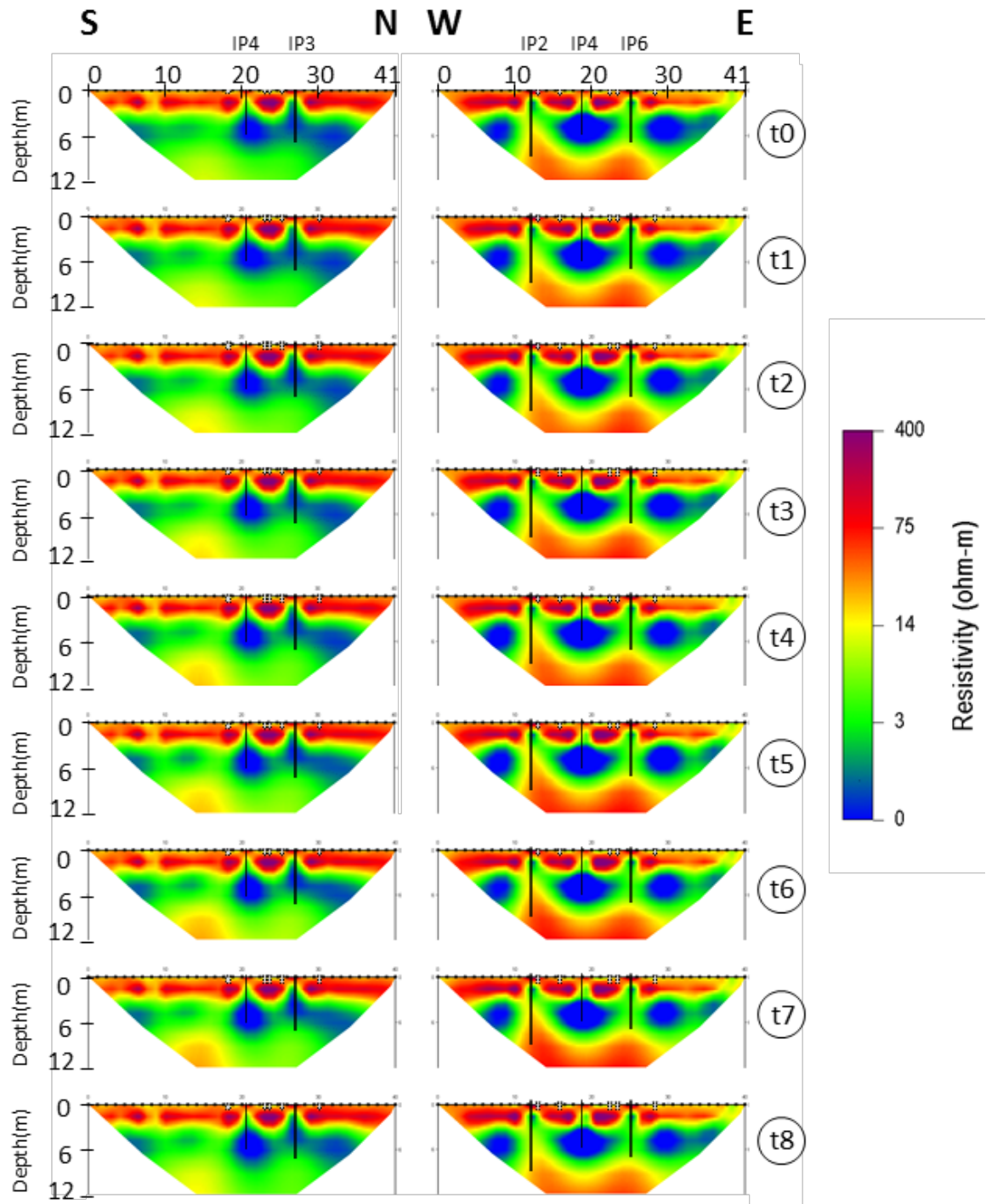
Figure 3-12. Selected images, using full L$_2$-norm minimization for the deep cell for both lines S-N and W-E. IPs are shown in each image, as well as VEPs (gray cylinders). Time steps are t0 to t8 and specific times are shown in Table 3-2. Axes are distances in m.

Figure 3-13 presents the information from Figure 3-12 as time-lapse ratios (relative to t0) for lines S-N (Figure 3-13a) and W-E (Figure 3-13b). An average of the resistivity values of 56 ratio images over time is shown in Figure 3-13c. Figures 3-13d and 3-13e provide ground truth data for temperatures and combustion gas concentration from the VEPs, respectively. The thermocouple near IP4 indicates smouldering ignition at around 1.8 days. Unfortunately, the CO_2 monitor was not functioning, therefore no corresponding gas data exists until 2.8 days. However, the ERT ratio images indicate a continuous increase in resistivity from images t1-t7 near IP4, particularly in Line W-E (Figure 3-13b), in Line S-N, the resistivity increase at IP4 is mostly focused on the right side of the IP and seems to increase after t3. In addition, the local resistivity around IP2 increases dramatically from t5-t7 when IP2 ignites (Figure 3-13b). Moreover, both lines exhibit a general increase in resistivity throughout the Alluvium from t1-t7. As observed in the shallow cell, the average resistivity in Figure 3-13c corresponds to air injection, treatment zones, temperature changes and combustion gases generation. However, the average increase in resistivity occurs when combustion gas concentration is at its highest collection rate, showing a parallel trend. Thus, despite the local drop in temperatures at the IPs and missing gas data, ERT suggests continuous reactions spreading outwards from IP4 and IP2, contributing further to the substantial resistivity of the Alluvium until t7.

In the shallow treatment cell, the high resistivity zone is localized, allowing visualization of the lateral spread of treatment. This is not the case in the deep cell, likely because (i) ERT resolution of the Alluvium is too low to distinguish specific treatment zones (sensitivity analysis in Appendix F), and (ii) some combustion gases generated are trapped below the MM, contributing to the resistivity increase. For the same reasons, the preheating (resistivity decrease) phase for each IP is not seen in these ratio images to the same degree as the shallow cell images. However, as seen in the shallow cell analysis, ERT clearly visualizes an overall resistivity decrease after shutdown of operations (red bar in Figure 3-13), indicating re-infiltration of groundwater (image t8, Figures 3-13a, b). Also, consistent between the shallow and deep analyses is the observation of increased vertical resistive pathways corresponding to the VEPs, suggesting visualization of the vapour capture zones.

a)

b)

Resistivity ratio

0.5   0.7   1.0   1.4   1.9
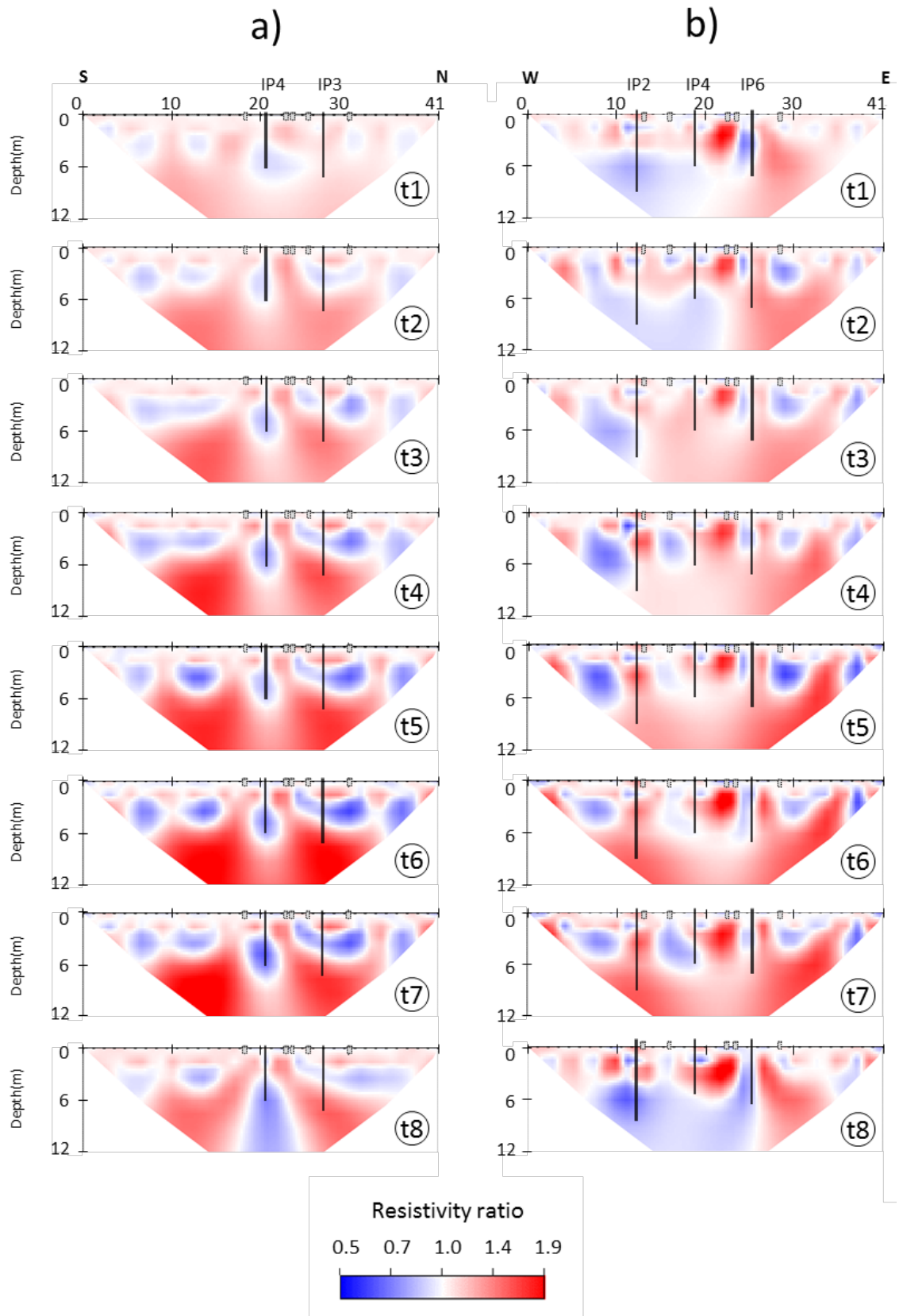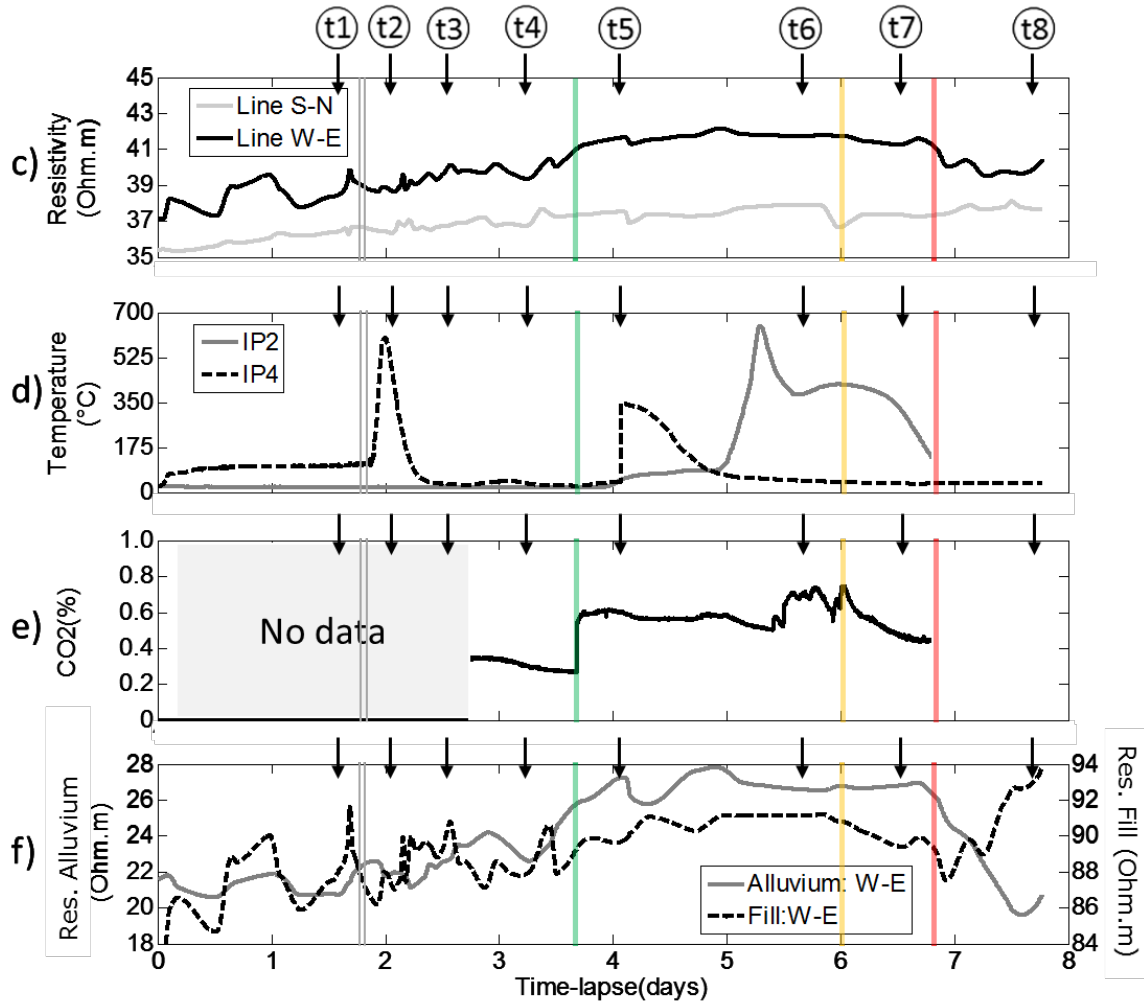
Figure 3-13. 4D resistivity ratio images for deep cell: (a) S-N line images from t1-t8, (b) W-E line images from t1-t8. In addition, (c) Average resistivity values from all such images. Also shown are (d) temperature graphs for selected thermocouples, and (e) CO_2 concentration for the vapor extraction system. Times t1-t8 shown by black arrows, while orange bars indicate temporary system shutdown (either heaters and air were off or just heaters off), green bar indicates system restart, and red bar is system shutdown. (f) Average resistivity for different layers in the subsurface for the deep cell: Fill layer (from 0 to 3.6 m), and Alluvium layer (from 7.65 to 11.1 m).

Figure 3-13f reveals that most of the resistivity changes occur in the Fill and the Alluvium for line W-E. The increase resistivity in the Fill is likely due to the VEPs collecting the smouldering gases. The MM exhibits effectively no change in resistivity over time, remaining 7-8 ohm·m throughout (shown in Appendix G), which is unsurprising since this low

permeability layer resists air and gas migration. The largest increases in resistivity are seen in the Alluvium, and primarily associated with STAR treatment given that combustion gases are still being collected (Figure 3-13c) and are most likely being generated in that region (treatment depth is in Alluvium). The resolution of ERT in the deep cell is insufficient for the same kind of focused analysis as performed for the shallow cell, however TarGOST data collected adjacent to IP4, shown in Figure 3-14 at the field site shows that, at the target depth of IP4, remediation occurred (difference in signal).
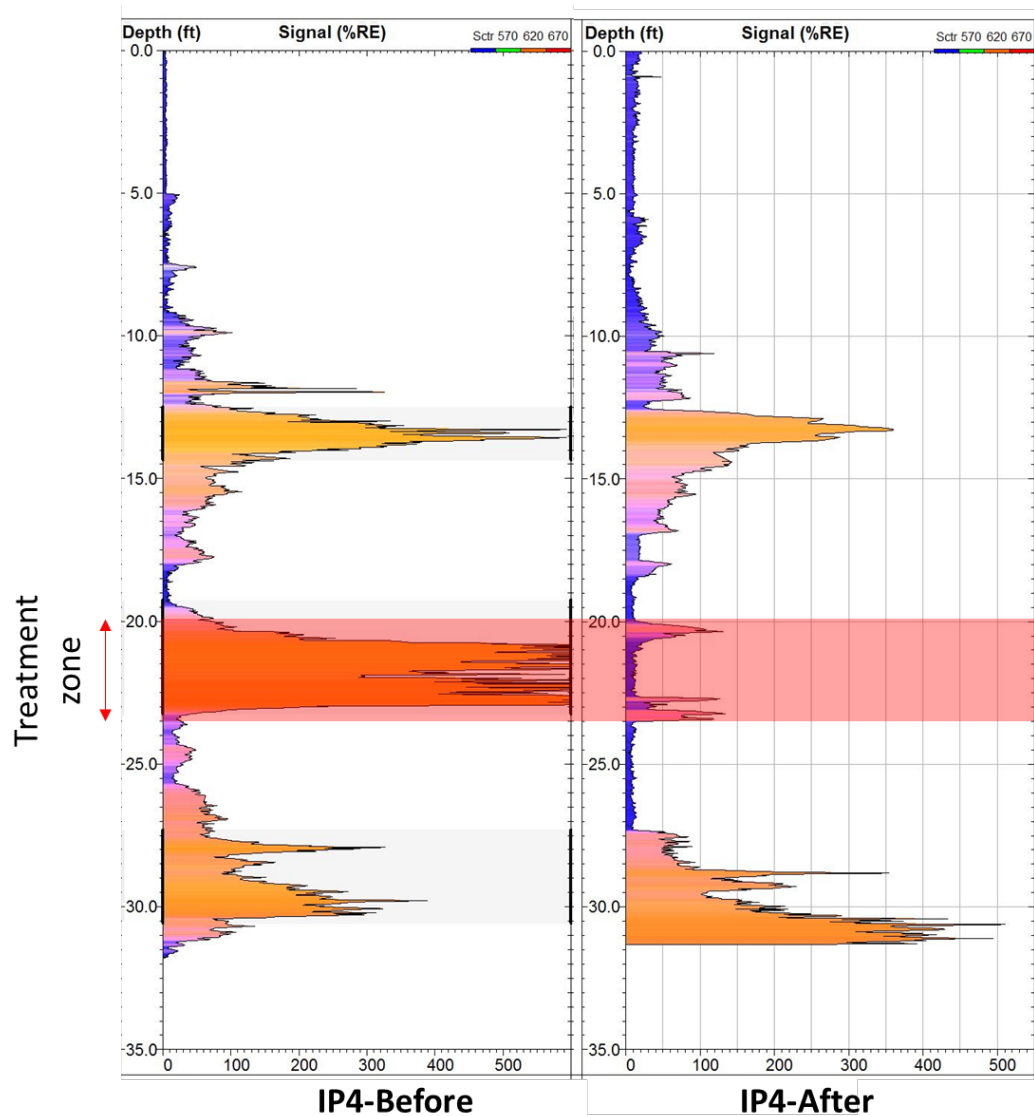
Figure 3-14. Before and after TarGOST® of IP4. Depth is in feet. Signal in % response (more details in Appendix A).

To further evaluate the re-infiltration of groundwater in the deep cell, ratio images were generated between the end of treatment (representing likely maximum extent of the dry treatment zones, volume of air injection and volume of combustion gases generated) and one day after treatment shutdown and air pressure release at the IPs. Figure 3-15 shows the resulting ratio images for lines S-N and W-E. The images show an overall decrease in resistivity in the regions below the MM where it was expected that combustion gases were trapped. These images suggest that re-infiltration dominated in the Alluvium where water saturation was lowest and where the resistivity increase during treatment was greatest. See Appendix H for more images on re-infiltration.
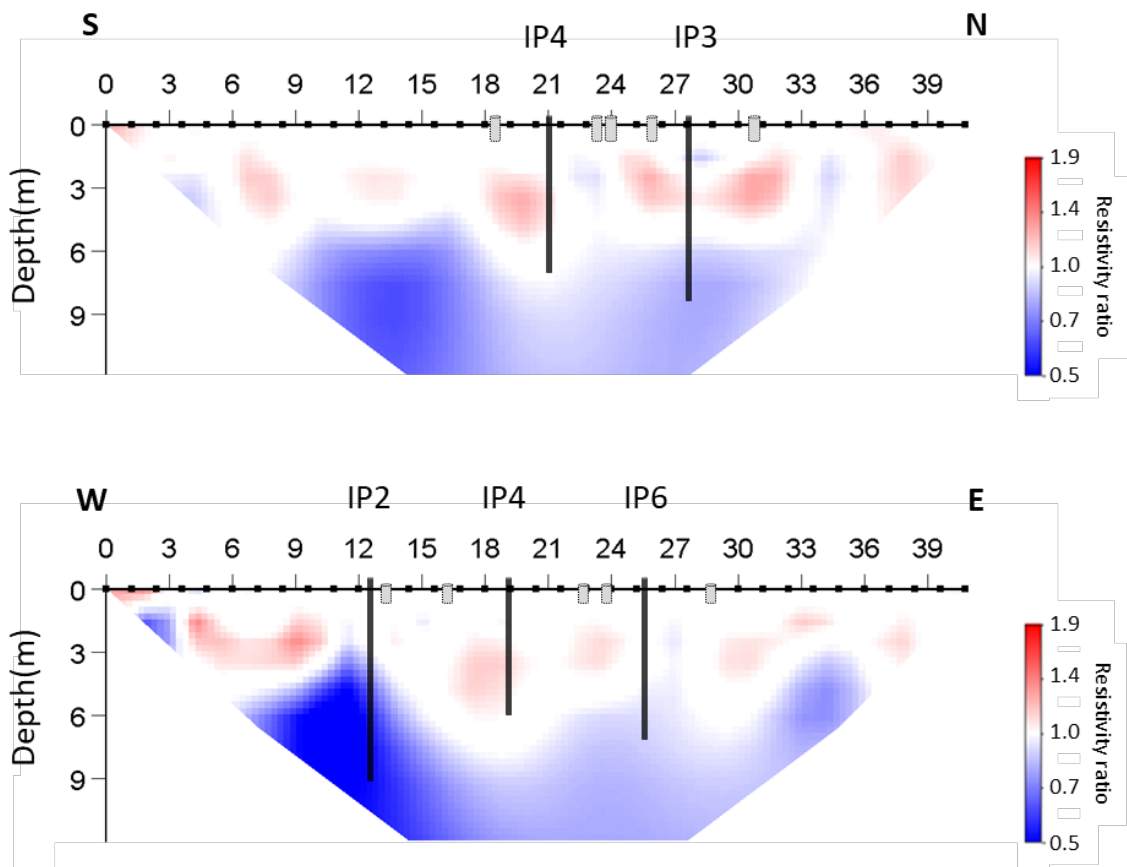
Figure 3-15. Deep cell S-N and W-E groundwater re-infiltration analysis.

3.5. Data Quality

A general description of the data quality for the images is provided and divided in three categories: measurement data quality, inversion quality and ratio images quality. The measured data quality was maximized due to low contact resistance provided by the installation of the electrodes. By reducing the contact resistance, the injection of DC current is improved (> 1

Amp) and the voltages that were recorded to convert to resistance using the geometrical factors were higher, indicating good signal to noise ratio. Raw data repeatability obtained by stacking indicated that less than 3% of the data was rejected due to high errors (>5%). Having a good signal to noise ratio and data repeatability while using a small spacing between the electrodes (important for the dipole-dipole array) indicate that a high signal is expected, despite the low subsurface resistivity. With the high signal obtained, the depth of investigation was approximately one-third of the total array length.

The inversion results showed good repeatability between lines and, most importantly, good agreement of the baseline ERT inverted models with geological ground truth (i.e., Figure 3-11). Inversion RMS misfit errors (between observed and predicted data) was 10-17%. This is higher than observed in other field studies (e.g., Tildy et al., 2017), however within expectations due to the metal interferences and the complex signal environment (competitive resistivity changes). The noise from the inversion results comes most likely from (i) the choice of performing a 2D ERT evaluation as a proof-of-concept, ignoring that STAR is a 3D phenomenon, (ii) the metal objects were also 3D, however in 2D inversion they are considered infinite in the direction perpendicular to the ERT lines, and (iii) high resistivity contrasts challenge the finite element solver of the governing differential equations; the need for higher discretization in order to provide a more accurate description of the modelled subsurface would require exhaustive computational time and programing. Given these challenges, the obtained inversion RMS misfit errors are quite reasonable and the inversion results are considered reliable.

Time-lapse ratio inversion results are affected by the overall inversion quality described previously. The repeatability of the images through time indicated smooth changes for the period that the STAR related actions were changing. This provides confidence in the time-lapse images. It is acknowledged that there is a good possibility that part of the changes we see are artifacts. To deal with the artifacts, the following approach was taken (i) choosing full-L_2 minimization of the inversion scheme producing smooth models that suppress artifacts, and (ii) data interpretation were focused only where data resolution was expected to be relatively high and where ground-truth was available to compare with the resistivity changes. This strategy provided a conservative approach to the data interpretation.

3.6.   Summary and Conclusions

Time-lapse ERT was applied for the first time to smouldering remediation of DNAPLs, to complement conventional data used to monitor STAR in field applications. To the author's knowledge, this represents the first time that ERT has been used to visualize the removal of DNAPL mass during a remediation program. Both a shallow (target depth ~3 m) and a deep (target depth ~8 m) coal tar layer smouldering event was monitored at a site undergoing full-scale STAR remediation. Each treatment cell was monitored with hourly tomograms over several days with two 2D perpendicular lines of 36 surface electrodes. 4D inversion was used to produce ration images in both cases.

A distinct, local signature for in situ STAR treatment was identified in the high-resolution, time-lapse ratio images of the shallow cell. Locations within an ignition point's radius of influence that exhibited a distinct "valley", representing a decrease in resistivity followed by an increase, appear to be correlated to STAR treatment by multiple lines of evidence. The decrease corresponds to the initial heating of the pore fluids while the increase corresponds to the subsequent boiling/smouldering removal of fluids from the pores. This signature allowed for mapping the approximate extent of STAR treatment in the shallow cell and distinguishing between ignition points that started outwards propagation smouldering reactions from those that did not. This provides information that would only be available with a much more extensive, dense network of multi-level thermocouples which is cost prohibitive on such a large site.

Due to the reduced resolution associated with deeper tomograms, the localized preheating of soil adjacent to ignition wells were not observed in the deep cell. However, time-lapse ratio images in both the shallow and deep treatments clearly showed expanding resistive zones around IPs known to have ignited. Moreover, both the shallow and the deep cells exhibited an increase in average subsurface resistivity during the known smouldering period which increases in parallel with the concentration of combustion gases collected at the surface (and thus rate of coal tar destroyed).

Numerous other features associated with the remediation operations were imaged by ERT. For example, the main vapour capture zones of influence and potential pockets of entrapped

air/combustion gases. There is evidence for the latter, in particular, trapped underneath the clay-rich Meadow Mat. Moreover, after system shut-down, in both cells a rapid general decrease in resistivity is observed that is likely mapping the re-infiltration of groundwater into the warm treated zones.

The results presented are promising for future coupling of geophysics to in situ STAR and other thermal remediation applications. It is acknowledged that in situ remediation processes are three-dimensional phenomena that are here being monitored by 2D ERT. This work should be considered as an initial proof-of-concept. Further evaluation would benefit from 3D ERT monitoring with optimized arrays to target the specific treatment depths. Moreover, additional in situ measurements, such as thermocouples, post-treatment cores and TarGOST®, and continuous groundwater levels would provide ground truth to further verify the ERT-based hypotheses. These are expected to be possible with a fully instrumented in situ STAR pilot test on a future site. For those locations where ground truth is available, the hypothesis of increased resistivity near IPs corresponding to treatment is validated.

3.7. References

Atekwana, E. A., Sauck, W. A., & Werkema, D. D. (2000). Investigations of geoelectrical signatures at a hydrocarbon contaminated site. Journal of Applied Geophysics, 44(2), 167-180.

Carrigan, C. R., Yang, X., LaBrecque, D. J., Larsen, D., Freeman, D., Ramirez, A. L., Daily, W., Aines, R., Newmark, R., & Friedmann, J. (2013). Electrical resistance tomographic monitoring of CO 2 movement in deep geologic reservoirs. International Journal of Greenhouse Gas Control, 18, 401-408.

Chandra, S., Ahmed, S., Nagaiah, E., Singh, S. K., & Chandra, P. C. (2011). Geophysical exploration for lithological control of arsenic contamination in groundwater in Middle Ganga Plains, India. Physics and Chemistry of the Earth, Parts A/B/C, 36(16), 1353-1362.

Clément, R., Oxarango, L., & Descloitres, M. (2011). Contribution of 3-D time-lapse ERT to the study of leachate recirculation in a landfill. Waste Management, 31(3), 457-467.

Commer, M., Doetsch, J., Dafflon, B., Wu, Y., Daley, T. M., & Hubbard, S. S. (2016). Time-lapse 3-D electrical resistance tomography inversion for crosswell monitoring of

dissolved and supercritical CO2 flow at two field sites: Escatawpa and Cranfield, Mississippi, USA. International Journal of Greenhouse Gas Control, 49(Complete), 297-311.

Daily, W., & Ramirez, A. (1995). Electrical resistance tomography during in-situ trichloroethylene remediation at the Savannah River Site. Journal of Applied Geophysics, 33(4), 239-249.

Daily, W., Ramirez, A., LaBrecque, D., & Nitao, J. (1992). Electrical resistivity tomography of vadose water movement. Water Resources Research, 28(5), 1429-1442.

Danielsen, B. E., & Dahlin, T. (2010). Numerical modelling of resolution and sensitivity of ERT in horizontal boreholes. Journal of Applied Geophysics, 70(3), 245-254.

Deng, Y., Shi, X., Xu, H., Sun, Y., Wu, J., & Revil, A. (2017). Quantitative assessment of electrical resistivity tomography for monitoring DNAPLs migration–Comparison with high-resolution light transmission visualization in laboratory sandbox. Journal of Hydrology, 544, 254-266.

Gaylor, D. W., Culp, S. J., Goldstein, L. S., & Beland, F. A. (2000). Cancer Risk Estimation for Mixtures of Coal Tars and Benzo(a)pyrene. Risk Anal., 20(1), 81.

Giordano, N., Arato, A., Comina, C., & Mandrone, G. (2017). Time-lapse electrical resistivity imaging of the thermally affected zone of a Borehole Thermal Energy Storage system near Torino (Northern Italy). Journal of Applied Geophysics, 140(Complete), 123-134.

Halihan, T., Paxton, S., Graham, I., Fenstemaker, T., & Riley, M. (2005). Post-remediation evaluation of a LNAPL site using electrical resistivity imaging. Journal of Environmental Monitoring, 7(4), 283-287.

Haslam, E. P., Gunn, D. A., Jackson, P. D., Lovell, M. A., Aydin, A., Prance, R. J., & Watson, P. (2014). Novel laboratory methods for determining the fine scale electrical resistivity structure of core. Journal of Applied Geophysics, 111, 384-392.

Hermans, T., Nguyen, F., Robert, T., & Revil, A. (2014). Geophysical Methods for Monitoring Temperature Changes in Shallow Low Enthalpy Geothermal Systems, Energies, 7, 5083–5118.

Hermans, T., Wildemeersch, S., Jamin, P., Orban, P., Brouyère, S., Dassargues, A., & Nguyen, F. (2015). Quantitative temperature monitoring of a heat tracing experiment using cross-borehole ERT. Geothermics, 53(Complete), 14-26.

Johnson, T. C., Versteeg, R. J., Day-Lewis, F. D., Major, W., & Lane, J. W. (2015). Time-Lapse Electrical Geophysical Monitoring of Amendment-Based Biostimulation. Groundwater, 53(6), 920-932.

Karaoulis, M., Kim, J.-H., & Tsourlos, P. (2011). 4D active time constrained resistivity inversion. Journal of Applied Geophysics, 73(1), 25-34.

Kavanaugh, M. C., Rao, P. S., & Wood, A. L. (2003). The DNAPL remediation challenge: is there a case for source depletion? U.S. Environmental Protection Agency, Washington, DC, EPA/600/R-03/143.

Kim, J.-H., Supper, R., Tsourlos, P., & Yi, M.-J. (2013). Four-dimensional inversion of resistivity monitoring data through Lp norm minimizations. Geophysical Journal International, 195(3), 1640-1656.

Kim, J.-H., Yi, M.-J., Park, S.-G., & Kim, J. G. (2009). 4-D inversion of DC resistivity monitoring data acquired over a dynamically changing earth model. Journal of Applied Geophysics, 68(4), 522-532.

Kim, K.-J., & Cho, I.-K. (2011). Time-lapse inversion of 2D resistivity monitoring data with a spatially varying cross-model constraint. Journal of Applied Geophysics, 74(2), 114-122.

Kinsman, L., Torero, J. L., & Gerhard, J. I. (2017). Organic liquid mobility induced by smoldering remediation. J Hazard Mater, 325, 101-112.

Kueper, B. H., & Davies, K. (2009). Assessment and Delineation of DNAPL Source Zones at Hazardous Waste Sites.

Kueper, B. H., Stroo, H. F., Vogel, C. M., & Ward, C. H. (2014). Chlorinated solvent source zone remediation: Springer.

LaBrecque, D. J., Ramirez, A. L., Daily, W. D., Binley, A. M., & Schima, S. A. (1996). ERT monitoring of environmental remediation processes. Measurement Science and Technology, 7(3), 375-383.

LaBrecque, D. J., & Yang, X. (2001). Difference inversion of ERT data: A fast inversion method for 3-D in situ monitoring. Journal of Environmental & Engineering Geophysics, 6(2), 83-89.

Lekmine, G., Auradou, H., Pessel, M., & Rayner, J. L. (2017). Quantification of tracer plume transport parameters in 2D saturated porous media by cross-borehole ERT imaging. Journal of Applied Geophysics, 139(Complete), 291-305.

Lundegard, P. D., & LaBrecque, D. (1995). Air sparging in a sandy aquifer (Florence, Oregon, USA): Actual and apparent radius of influence. Journal of Contaminant Hydrology, 19(1), 1-27.

Mao, D., Revil, A., Hort, R. D., Munakata-Marr, J., Atekwana, E. A., & Kulessa, B. (2015). Resistivity and self-potential tomography applied to groundwater remediation and contaminant plumes: Sandbox and field experiments. Journal of Hydrology, 530, 1-14.

Masy, T., Caterina, D., Tromme, O., Lavigne, B., Thonart, P., Hiligsmann, S., & Nguyen, F. (2016). Electrical resistivity tomography to monitor enhanced biodegradation of hydrocarbons with Rhodococcus erythropolis T902. 1 at a pilot scale. Journal of Contaminant Hydrology, 184, 1-13.

Miller, C. R., Routh, P. S., Brosten, T. R., & McNamara, J. P. (2008). Application of time-lapse ERT imaging to watershed characterization. Geophysics, 73(3), G7-G17.

Newmark, R. L., Boyd, S., Daily, W., Goldman, R., Hunter, R., Kayes, D., Kenneally, K., Ramirez, A., Udell, K., & Wilt, M. (1994). *Using geophysical techniques to control in situ thermal remediation*.

Newmark, R. L., Daily, W. D., Kyle, K. R., & Ramirez, A. L. (1998). Monitoring DNAPL pumping using integrated geophysical techniques. Journal of Environmental and Engineering Geophysics, 3(1), 7-13.

Pironi, P., Switzer, C., Gerhard, J. I., Rein, G., & Torero, J. L. (2011). Self-Sustaining Smoldering Combustion for NAPL Remediation: Laboratory Evaluation of Process Sensitivity to Key Parameters. Environ. Sci. Technol., 45(7), 2980.

Pironi, P., Switzer, C., Gerhard, J. I., Rein, G., Torero, J. L., & Fuentes, A. (2009). Small-Scale Forward Smouldering Experiments for Remediation of Coal Tar in Inert Media. Proc. Combust. Inst., 32(2), 1957.

Power, C., Gerhard, J. I., Karaoulis, M., Tsourlos, P., & Giannopoulos, A. (2014). Evaluating four-dimensional time-lapse electrical resistivity tomography for monitoring DNAPL source zone remediation. J Contam Hydrol, 162-163, 27-46.

Power, C., Gerhard, J. I., Tsourlos, P., Soupios, P., Simyrdanis, K., & Karaoulis, M. (2015). Improved time-lapse electrical resistivity tomography monitoring of dense non-aqueous phase liquids with surface-to-horizontal borehole arrays. Journal of Applied Geophysics, 112, 1-13.

Ramirez, A., Daily, W., LaBrecque, D., Owen, E., & Chesnut, D. (1993). Monitoring an underground steam injection process using electrical resistance tomography. Water Resources Research, 29(1), 73-87.

Revil, A., Karaoulis, M., Johnson, T., & Kemna, A. (2012). Some low-frequency electrical methods for subsurface characterization and monitoring in hydrogeology. Hydrogeology Journal, 20(4), 617-658.

Samouëlian, A., Cousin, I., Tabbagh, A., Bruand, A., & Richard, G. (2005). Electrical resistivity survey in soil science: a review. Soil and Tillage research, 83(2), 173-193.

Sasaki, Y. (1992). Resolution of resistivity tomography inferred from numerical simulation.

Schmidt-Hattenberger, C., Bergmann, P., Labitzke, T., Wagner, F., & Rippe, D. (2016). Permanent crosshole electrical resistivity tomography (ERT) as an established method for the long-term CO2 monitoring at the Ketzin pilot site. International Journal of Greenhouse Gas Control, 52(Complete), 432-448.

Scholes, G. C., Gerhard, J. I., Grant, G. P., Major, D. W., Vidumsky, J. E., Switzer, C., & Torero, J. L. (2015). Smoldering Remediation of Coal-Tar-Contaminated Soil: Pilot Field Tests of STAR. Environmental Science & Technology, 49(24), 14334-14342.

Slater, L., & Binley, A. (2003). Evaluation of permeable reactive barrier (PRB) integrity using electrical imaging methods. Geophysics, 68(3), 911-921.

Slater, L., & Binley, A. (2006). Synthetic and field-based electrical imaging of a zerovalent iron barrier: Implications for monitoring long-term barrier performance. Geophysics, 71(5), B129-B137.

Slater, L., Binley, A. M., Daily, W., & Johnson, R. (2000). Cross-hole electrical imaging of a controlled saline tracer injection. Journal of Applied Geophysics, 44(2), 85-102.

Sparrenbom, C. J., Åkesson, S., Johansson, S., Hagerberg, D., & Dahlin, T. (2017). Investigation of chlorinated solvent pollution with resistivity and induced polarization. Science of the Total Environment, 575, 767-778.

Switzer, C., Pironi, P., Gerhard, J. I., Rein, G., & Torero, J. L. (2009). Self-Sustaining Smoldering Combustion: A Novel Remediation Process for Non-Aqueous-Phase Liquids in Porous Media. Environ. Sci. Technol., 43, 5871.

Tildy, P., Neducza, B., Nagy, P., Kanli, A. I., & Hegymegi, C. (2017). Time lapse 3D geoelectric measurements for monitoring of in-situ remediation. Journal of Applied Geophysics, 136, 99-113.

Tøndel, R., Schütt, H., Dümmong, S., Ducrocq, A., Godfrey, R., LaBrecque, D., Nutt, L., Campbell, A., & Rufino, R. (2014). Reservoir monitoring of steam-assisted gravity drainage using borehole measurements. Geophysical Prospecting, 62(4), 760-778.

Wang, S., Lee, M., Park, M. K., & Kim, J.-M. (2010). Box experiments on monitoring the CO 2 migration in a homogeneous medium using electrical resistivity survey. Geosciences Journal, 14(1), 77-85.

Yi, M.-J., Kim, J.-H., & Chung, S.-H. (2003). Enhancing the resolving power of least-squares inversion with active constraint balancing. Geophysics, 68(3), 931-941.

Chapter 4

4. Conclusions and Recommendations

4.1. Conclusions

This research focused on applying surface time-lapse Electrical Resistivity Tomography (ERT), a surface-based geophysical technique, as a complementary method for conventional intrusive monitoring of the first full-scale in situ application of the smouldering technology STAR for a site in Newark, New Jersey contaminated with coal tar. Qualitative analysis of resistivity ratio images was performed to compare with temperature profiles (peak temperature from 300°C to 1000°C) and combustion gases (mainly CO_2) concentration data. Two treatment cells were analysed, a shallow heterogenous Fill layer (shallow cell) and the Alluvium sandy layer (deep cell). A cell, consists of IPs, VEPs and thermocouples that monitor temperature. Each cell was monitored for approximately 8 days, with two 2D lines of 36 electrodes of 0.6m spacing for shallow cell (target depth ~3 meters) and 1.2m spacing for deep cell (target depth ~8m). Installation of electrodes was a challenge, as it had to go through the asphalt and Columbia Fill (mainly gravel) into the Fill layer, however contact resistance of 0.5 Kohm indicated that the contact between electrodes and soil was good. Resistivity surveys were conducted before, during and after treatment to provide insight into the spatial extent of the STAR smouldering reaction, groundwater and gas mobility, influence of air flow and the capture zone of vapor extraction system.

Results suggested that:

- Vertical conductive interferences from metal IPs, with resistivity values of 0.2 - 4 ohm·m, were observed in the background and 4D images for both shallow and deep cells. These interferences were localized and did not cover the major geological features of the background and 4D images, such as the heterogenous Fill layer (190 ohm·m), the Meadow Mat (10-20 ohm·m) and the Alluvium (30 ohm·m).

- 4D images, inverted simultaneously in time (Kim et al., 2009; Kim et al., 2013), show consistent inversion results. However, to remove the background geological and static interferences, ratio images were used to interpret the changes in the subsurface due to remedial activities. RMS (root mean square) error of the ratio images after data filtering were in between 10-12% for the shallow cell and 15-17% for the deep cell. For a 3D remedial phenomenon with 3D effects monitored by a 2D ERT array, these RMS represents good quality of data.

- Electrical resistivity changes could be coming from several chemical and physical changes in the subsurface (Ramirez et al., 1993; Samouëlian et al., 2005), indeed STAR presents a complex signal for electrical resistivity imaging. However, when associated to the combustion gas concentration and temperature profiles, in general, the 4D images show signal response with temperature changes, where resistivity reaches more than 60% reduction, as well with combustion gases generation, where increase of resistivity was more than 130%, when compared to the background.

- Physical displacement of water by air injection in the surrounding of the wells, pre-treatment, shows increase of resistivity values as water saturation changes, for both shallow and deep cells. Whereas during the preheating phase, decreases in resistivity values are observed. Preheating is observed only in the shallow cell.

- When reaching boiling temperature, both temperature and saturation changes are in effect, and resistivity starts to increase, for both cells. Continuous increases in resistivity after boiling temperature is observed at the same time as continuous extraction of combustion gases (CO_2 and CO) generated from the smouldering reaction, suggesting that increases in resistivity could be related to generation of CO_2 and CO in the subsurface. This realization is particularly important for the deep cell, where gas generation was not measured for the beginning of the smouldering reaction.

- In the deep cell, it was not possible to distinguish specific IP treatment zones, because of low resolution and possibly trapped gases below the clay layer (Meadow Mat), increasing the images resistivity below the Meadow Mat (i.e., Alluvium).

- Capture zones of the vapor extraction system were possible to be identified in the shallow and deep cells by vertical continuous resistivity pathways. Because full-scale STAR uses a step approach where each cell is installed one at a time, this could have significant importance when designing future vapor extraction point installations.

- After shutdown of treatment, decrease in resistivity was observed in the overall images for both cells and can be correlated to water re-infiltrating the subsurface after remedial activities dried the soil.

- Focused analysis in the shallow cell provided insight on the extent of the dry clean treated zone generated by smouldering reaction: the "postulated STAR treatment zones". However, areas of low resolution and possible trapped gases not captured by the vapor extraction system were showed. The "postulated STAR treatment zones" are not easily provided by conventional monitoring, it would be required too many boreholes to give an idea of the extent of the reaction. This analysis showed that smouldering did not occur in IP1 and IP2, while IP3, IP4 and IP5 presented smouldering reaction extending to the expected radii of influence of an IP. This is a novel and approximate method to identify smouldering reaction extent that is specific and not definitive. This analysis proved to be another line of evidence and complimentary to the other information provided both by temperature and CO_2, as well as the resistivity images.

In summary, ERT applied to in situ monitoring of the STAR presents the potential for a new, non-intrusive and less costly alternative method to complement the conventional monitoring already in place for smouldering remediation, and provide further insights and conclusions that could be useful for both designing and efficiency analysis of the remedial activities of the site.

4.2. Recommendations

The results presented are promising for future coupling of geophysics to in situ STAR applications. Considering this is the first study to perform ERT to STAR, there are many improvements and recommendations for future work. Some of them are below:

- STAR is a 3D phenomenon that is being monitored in this case by 2D ERT as a proof-of-concept; therefore, to continue this evaluation, it is suggested a 3D ERT monitoring within the treatment cells. Time-lapse should still be used to remove interferences from metals and the background geology.

- For increase resolution in deeper cells, an optimized array could be useful, as it combines different types of array (e.g., dipole-dipole, multi-gradient) to focus on the target and depth desired (Loke et al., 2015).

- Coupled geophysics methods, such as ERT combined with self-potential and induced polarization, could potentially improve understanding of the STAR operation. ERT joint inversion with self-potential is a new field of research that is increasing (e.g., Mao 2015). Self-potential has been used to monitor changes in temperature and has been used applied in laboratory scale to STAR (Ebrahimzadeh et al., 2017).

4.3. References

Ebrahimzadeh, M., Tsourlos, P., & Gerhard, J.I. (2017). Self-potential for monitoring soil remediation by smoldering: proof of concept. *Near Surface Geophysics*, In press.

Kim, J.-H., Supper, R., Tsourlos, P., & Yi, M.-J. (2013). Four-dimensional inversion of resistivity monitoring data through Lp norm minimizations. *Geophysical Journal International, 195*(3), 1640-1656.

Kim, J.-H., Yi, M.-J., Park, S.-G., & Kim, J. G. (2009). 4-D inversion of DC resistivity monitoring data acquired over a dynamically changing earth model. *Journal of Applied Geophysics, 68*(4), 522-532.

Loke, M. H., Wilkinson, P. B., Chambers, J. E., Uhlemann, S. S., & Sorensen, J. P. R. (2015). Optimized arrays for 2-D resistivity survey lines with a large number of electrodes. *Journal of Applied Geophysics, 112*, 136-146.

Mao, D., Revil, A., Hort, R. D., Munakata-Marr, J., Atekwana, E. A., & Kulessa, B. (2015). Resistivity and self-potential tomography applied to groundwater remediation and contaminant plumes: Sandbox and field experiments. *Journal of Hydrology, 530*, 1-14.

Ramirez, A., Daily, W., LaBrecque, D., Owen, E., & Chesnut, D. (1993). Monitoring an underground steam injection process using electrical resistance tomography. *Water Resources Research, 29*(1), 73-87.

Samouëlian, A., Cousin, I., Tabbagh, A., Bruand, A., & Richard, G. (2005). Electrical resistivity survey in soil science: a review. *Soil and Tillage research, 83*(2), 173-193.

Appendices

APPENDIX A. Details on STAR operation

Shallow treatment unit details of installation confirmatory sampling

Details on the installation of the shallow ignition points (IPs) are shown in Table A-1. These numbers were based on the core logs collected in the locations prior to installation of IPs (Figure A-1). The screen intervals are the location where the heaters will be located as well as air was injected. The treatment target depth was based on the core logs observation of DNAPL (dense non-aqueous phase liquids) free phase or residuals, as well as the PID (photo-ionizing detector) levels. The thermocouples installation depth is the depth of the deepest thermocouple to be installed in the multilevel thermocouple. In a length of 0.8 meters, four thermocouples are placed, 0.2 meters apart (Table A-1).

Table A-1. STAR IP and Thermocouples Installation Summary - Shallow Cell

IP	IP Screen interval (mbgs)	Approx. target treatment depths (mbgs)	Thermocouples installation depth (mbgs)
IP1	2.7-3.0	2.7-2.9	3.0
IP2	2.6-2.9	2.6-2.9	2.9
IP3	2.6-2.9	1.9-2.9	2.9
IP4	2.4-2.7	2.4-2.7	2.7
IP5	2.7-3.0	1.8-2.8	3.0

The geology in each core log is shown in Figure A-1, as well as the contamination level and PID signal. The predominant geology observed in the shallow treatment unit is the Fill layer, and it is possible to observe heterogeneous materials in this layer (concrete, wood, gravel). The Meadow Mat delimitate the shallow treatment unit, being that the IPs are installed on top of the Meadow Mat. The contamination level (light, moderate and heavy impacts and residuals/stains) is based on observation of the cores according to the

professional that logged the cores. The contamination level determines the target treatment depths. PID (photo-ionizing detector) measurements detect total volatile organic compounds in the samples in parts per million (ppm), confirming the observations taken on the contamination levels.
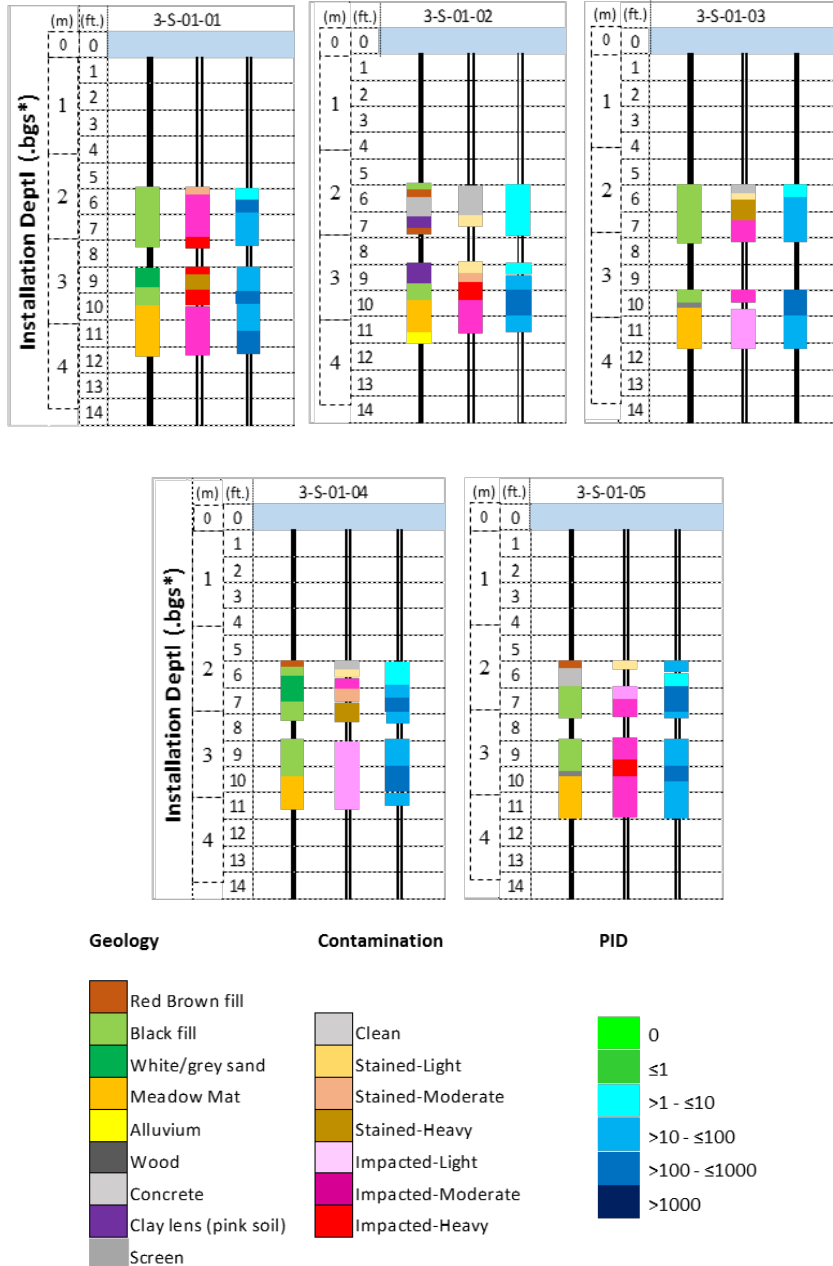

Figure A-1. Core logs from IPs in the shallow treatment unit, containing geology, contamination level and PID observations. *.bgs = below ground surface, results are shown in meters and feet. IPX = 3-S-01-0X.

Figure A-2 shows the only core taken after the treatment, the core was collected near IP3, to confirm a smouldering reaction in that region. As noted, the reaction region where the treatment was expected (red rectangle) returned as not recovered core. In fact, this is one of the reasons why geophysics is being analyzed for STAR.
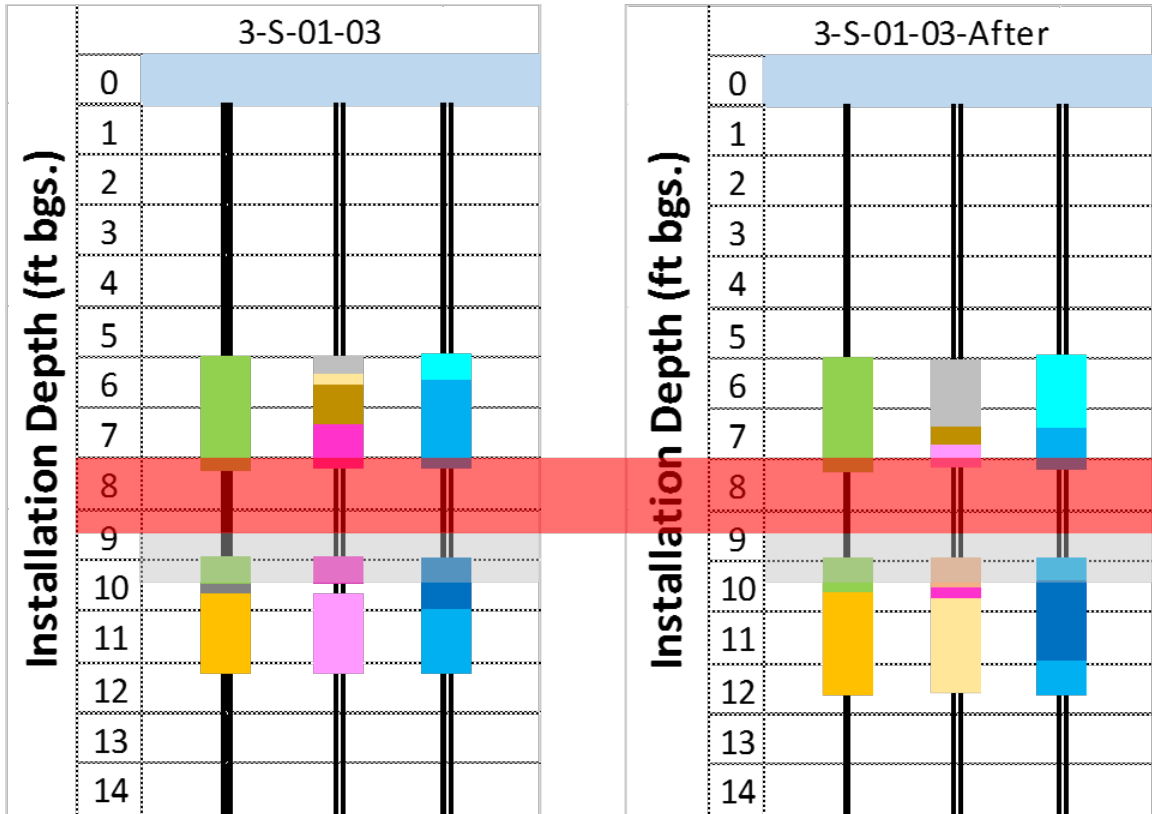
Figure A-2. Core log before and after treatment for IP3 (3-S-01-03), displayed in Line W-E in the shallow unit treatment. The expected treatment region (red rectangle) has no-recovery cores. Legend in Figure A-1.

Deep treatment unit details of installation confirmatory sampling

The deep treatment unit installation details are shown in Table A-2. Cores are not taken in deep units of treatment, instead the analysis of contaminant level and target treatment is based on a direct-push screening technology that targets coal tar and creosotes in free phase (DNAPL). TarGOST ® (Tar-specific Green Optical Screening Tool) has a probe with a sapphire window in the side that is inserted in a direct-push rod. A fluorescent light is shoot in the window and the coal tar and creosote fluorescence signal is directed back up-hole to

be analyzed. Responses are indicated in real-time on a graph of Signal versus depth, as seen in Figure A-3a-c. The logged results are color-coded, orange colour is indicative of coal tar DNAPL. The call-outs for each TARGOST ® log in Figure A-3a-c indicates the Meadow Mat layer, as well as the shallow and deep treatment targets for the treatment unit. Only one layer is treated per time, the second treatment layer is treated afterwards. The Meadow Mat ranges from 3.4 - 4.4 mbgs.

Table A-2. STAR IP and Thermocouples Installation Summary - Deep cell

IP	IP Screen interval (mbgs)	Approx. target treatment depths (mbgs)	Thermocouples installation depth (mbgs)
IP1	6.9-7.2	6.2-7.0	7.2
IP2	9.1-9.4	8.6-9.3	9.4
IP3	7.5-7.8	6.9-7.7	7.8
IP4	6.9-7.2	6.2-7.0	7.2
IP5	7.5-7.8	6.8-7.6	7.8
IP6	7.2-7.5	6.1-7.3	7.5
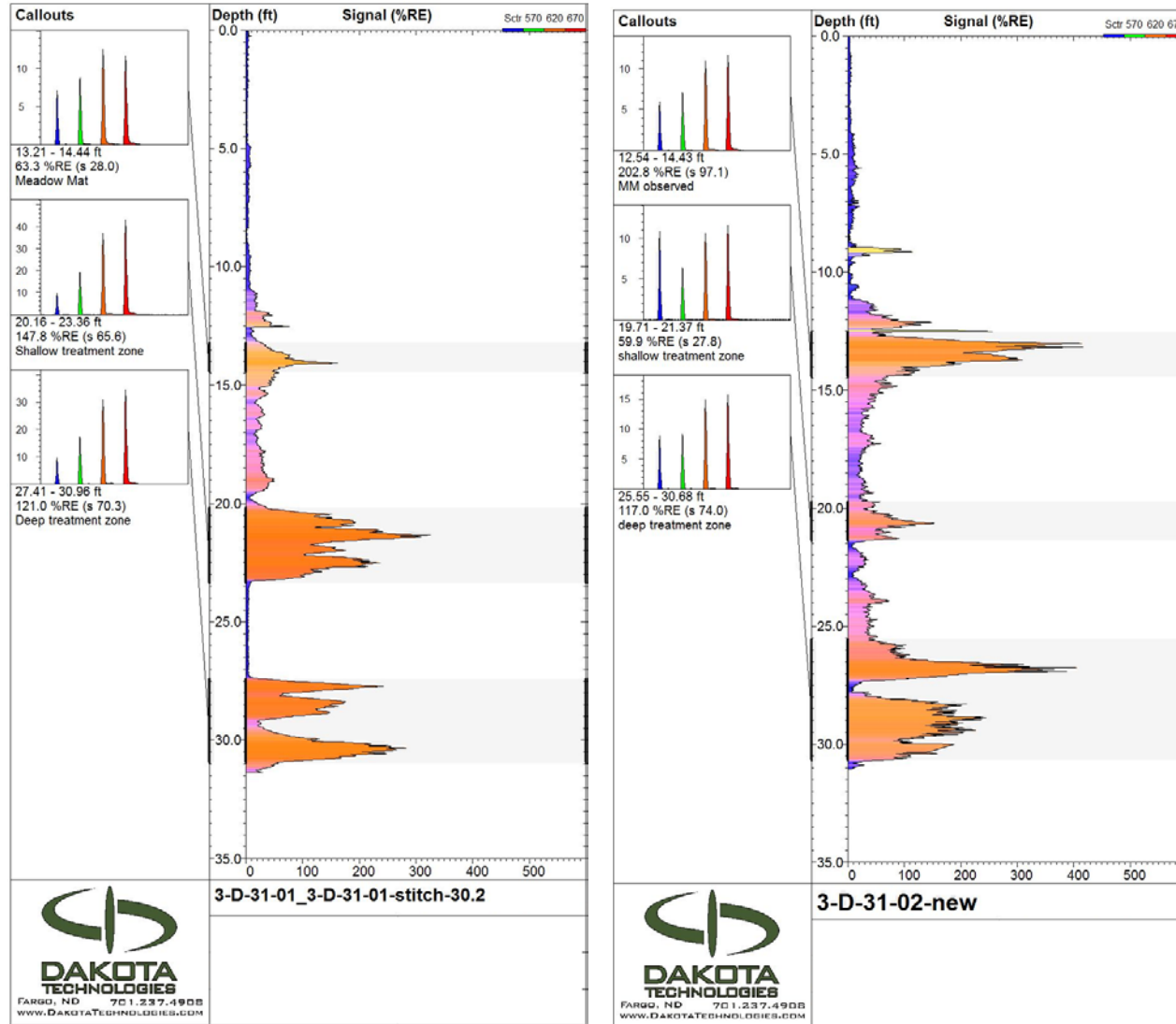
Figure A-3a. TarGOST ® data for IP1 (3-D-31-01), target treatment at 20 - 23 ft. and IP2 (3-D-31-02-new), target treatment at 25 - 30 ft.
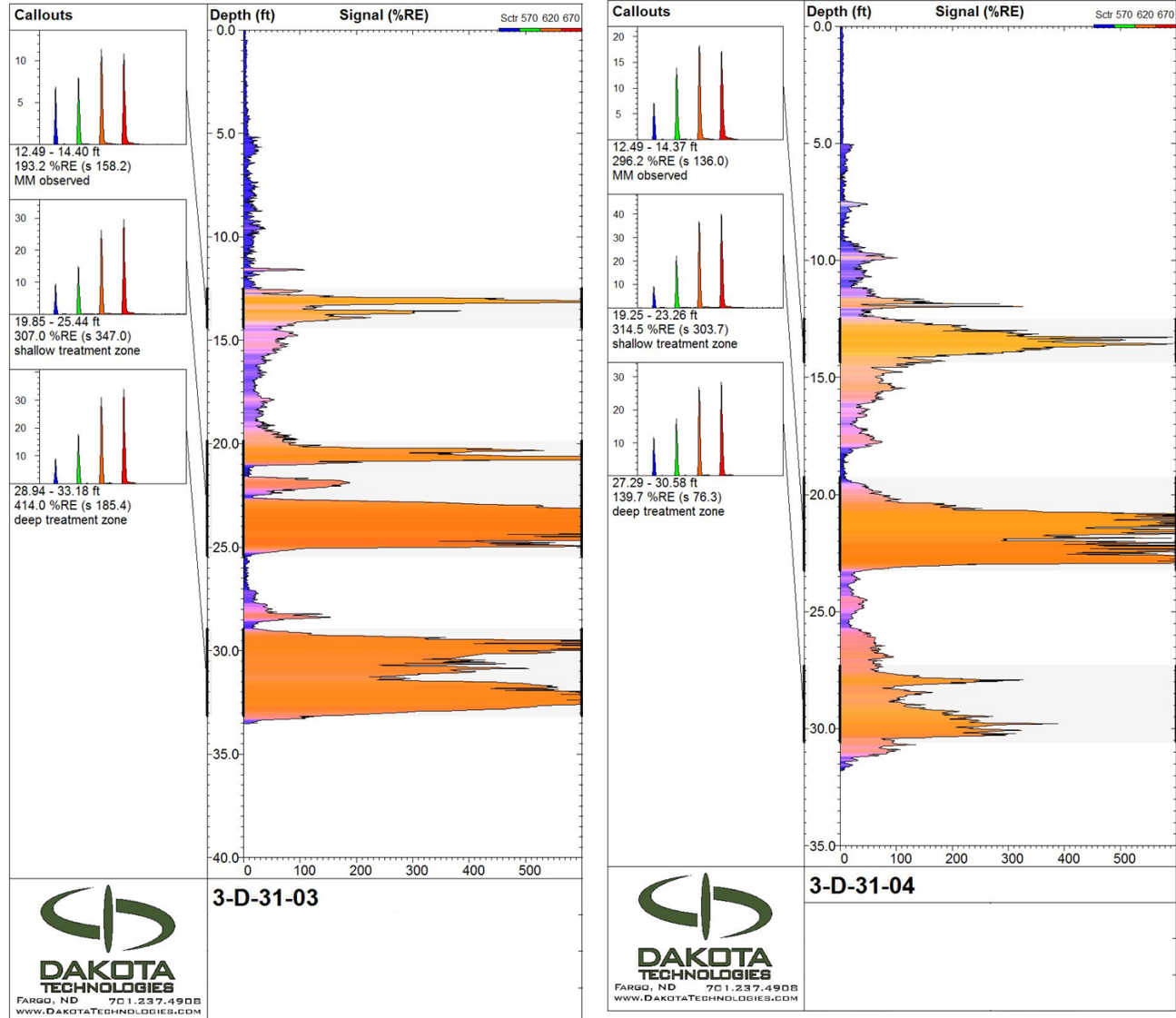
Figure A-3b. TarGOST ® data for IP3 (3-D-31-03), target treatment 20 - 25 ft. and IP4 (3-D-31-04), target treatment 20 - 23 ft.
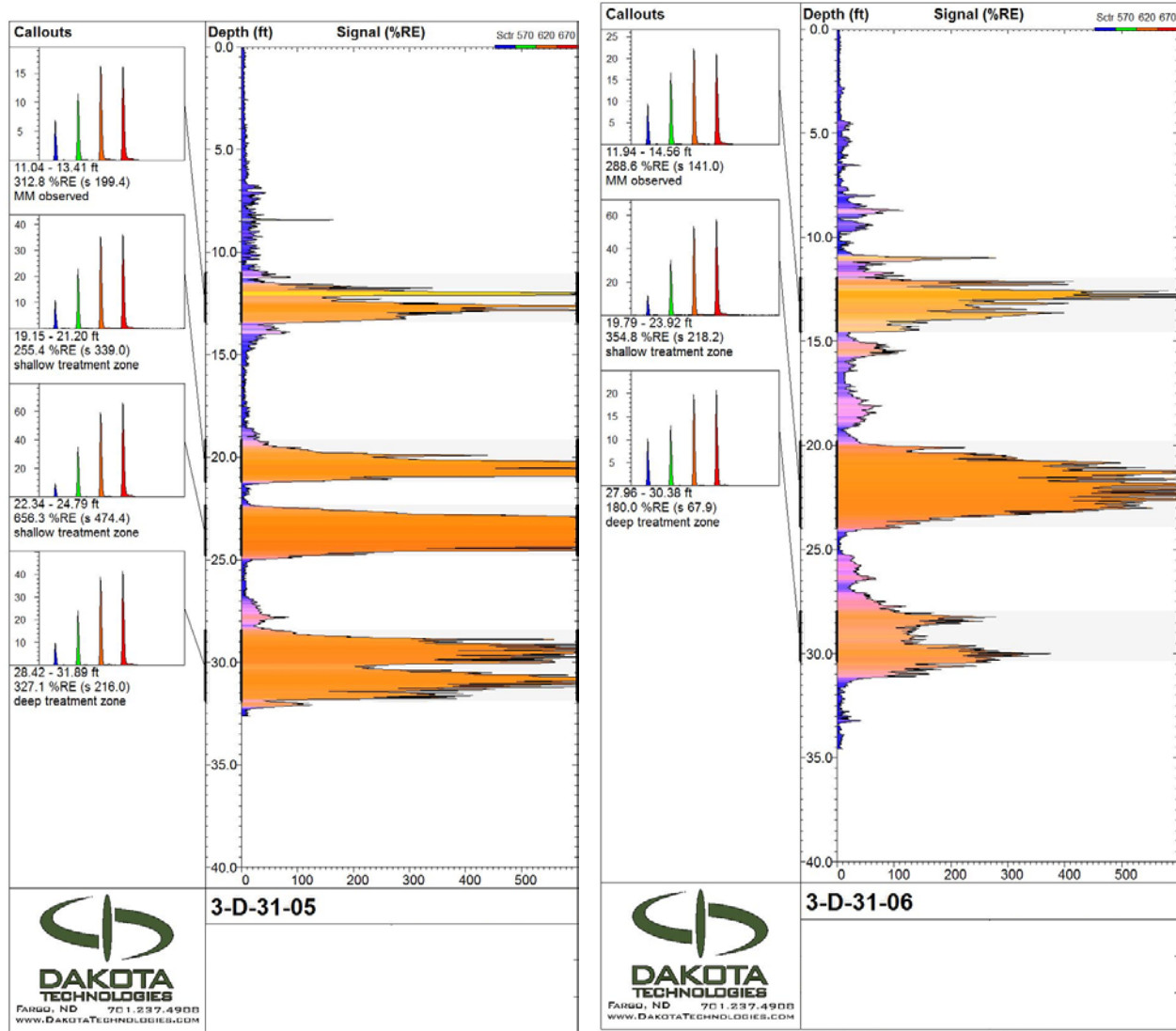
Figure A-3c. TarGOST ® data for IP4 (3-D-31-05), target treatment 20 - 25 ft. and IP5 (3-D-31-06), target treatment 20 - 24 ft. Note that IP5 has two deep treatment zones.

TarGOST ® logs were taken before and after treatment for IP4, as seen in Figure A-4. The target treatment, as described in Table A-2, was free of free-phase DNAPL after STAR treatment.
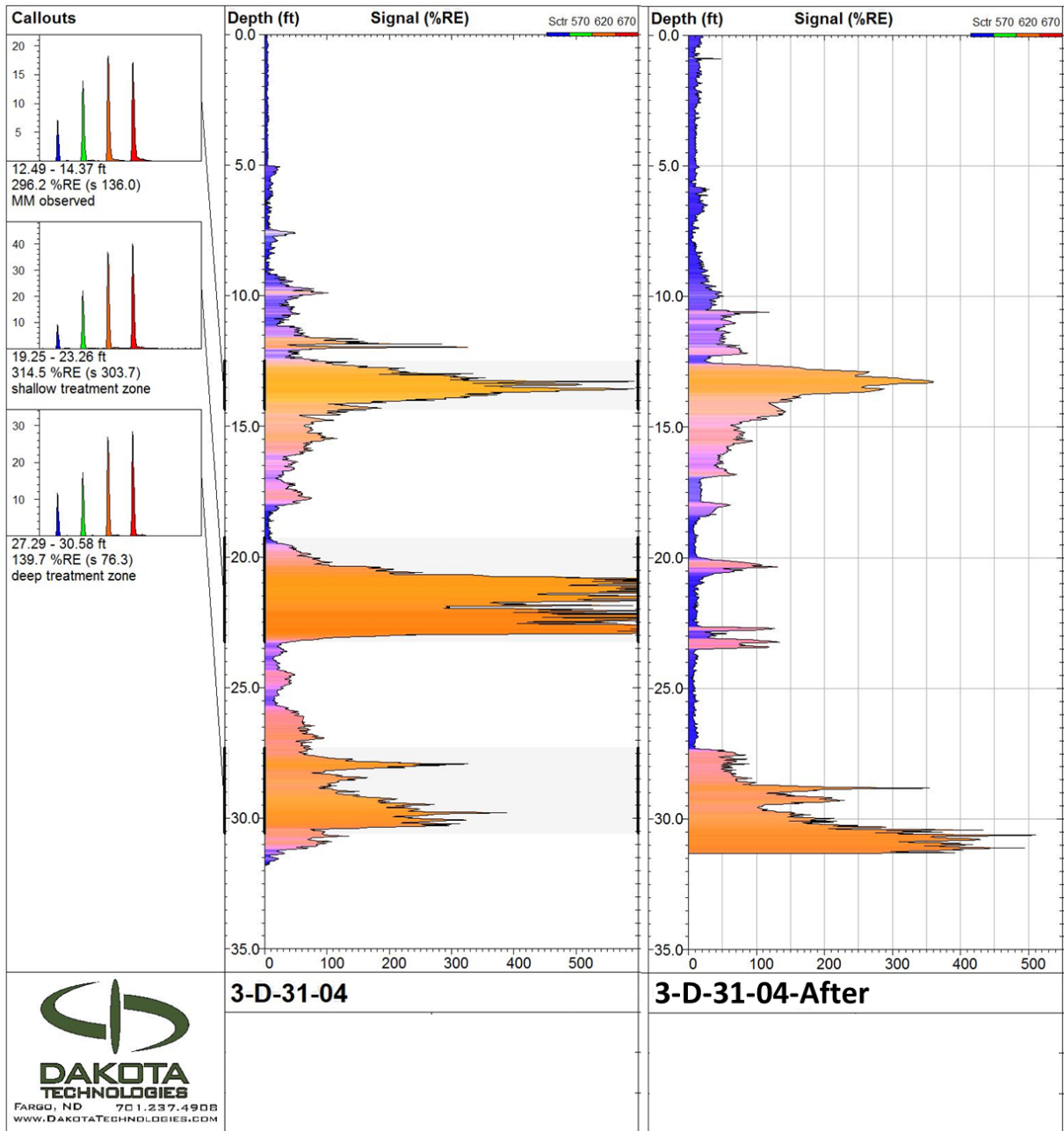
Figure A-4. Before and after TarGOST® of IP4 (3-D-31-04). Target treatment depth between 20-25 feet.

Groundwater levels

Groundwater levels for both cells are shown in Table A-3.

Table A-3. Groundwater Levels in Meters Below Ground Surface (mbgs)*

Date	WLP-3[1]	WLP-4[2]
2016-07-11	1.40	-
2016-08-02	1.14	1.07
2016-08-09	1.23	1.12
2016-08-30	-	1.24
2016-09-03	1.58	1.28
2016-09-12	-	1.54
Average	1.36	1.25
MAX	1.58	1.54
MIN	1.14	1.07

* Only showing monitoring wells near the treatment unit

[1] WLP-31 is near both units

[2] WLP-42 is near deep treatment unit

APPENDIX B. Details on ERT installation

Electrode installation tests were conducted prior to the actual field implementation, due to the complexity of the top layer (Figure B-1): heterogenous Fill layer, covered by asphalt and gravel (Colombia Fill), possibly dry, resisting current injection by increasing contact resistance. For the shallow cell, the gravel layer was thinner than the deep, therefore the installation of the electrodes was done manually using a hammer drill (Figure B-2) to drill a hole 0.23cm mbgs (meters below ground surface) using a 4cm drill bit, where the electrodes where placed and hammered down to an additional 15cm into the historical Fill cell. The drilled holes were filled with bentonite (Figure B-2) to keep a good contact resistance during the system operation. For the deep cell, the electrodes were installed 1.02m deep with a Geoprobe (Figure B-2) and the last 15cm were installed with a hammer drill direct push (Figure B-2). The holes were filled with sand and bentonite and watered afterward (Figure B-2). All electrode holes were capped with tar (Figure B-2) to avoid preferential pathways of gas during the smouldering reactions. The final installation is shown in Figure B-3.
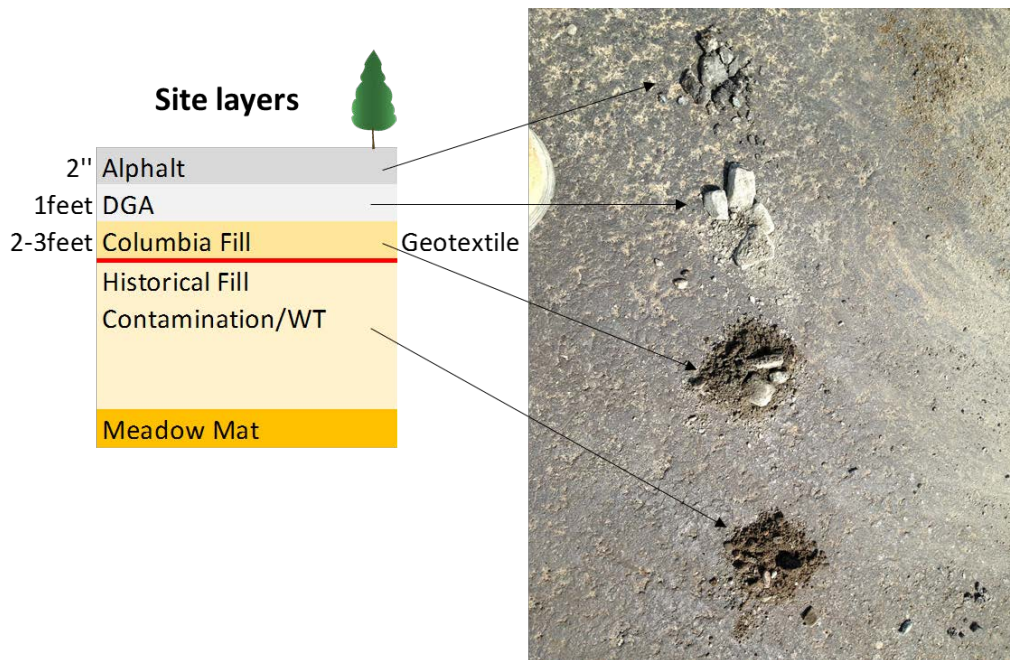

Figure B-1. Layers to be overcome by the electrodes. Installation had to occur in the Historical Fill layer. As possible to observe, gravel and heterogeneities reduce with depth.

Figure B-2. Details on the installation of the ERT electrodes using geoprobe and hammer drill.

Figure B-3. Details on the installation of the ERT for the shallow cell.

The monitoring occurred during the day and throughout the night, when no one could be at the field site. Therefore, the equipment needed to be protected from rain, wind and any other external interferences. The set up (Figure B-4) was different for shallow and deep, but mainly consisted in encapsulating the equipment with a fan to prevent from overheating in one plastic box, while encapsulating the computer with remote control, internet access, battery for ERT equipment during the night and another fan in another plastic box. Both boxes were above a pallet. At night, the boxes were covered with a tarp to avoid rain. During the day, temperatures were very high and the site is very windy, therefore protection were also in place for sun protection (tents).

Figure B-4. (Top) Blue box contained the ERT equipment and switch box (right), while grey box contained the computer with battery support for the ERT equipment (left). (Bottom) Tarp was used to cover to protect from rain.

APPENDIX C. L1 and L2 norms

As discussed in the literature review and main chapter of this thesis, regularizations are added to the inversion algorithm to smooth and control the modeled data. Regularizations can be in an L2-norm, or in an L1-norm. For 4D time-lapse inversions, L1- and L2-norms can be use in either space domain or time domain. A third regularization (either L1- or L2-norm) can also be applied to the data error minimization (see Kim et al., 2013). Full L1-norm are called robust inversion, while full L2-norm is called smooth inversion. L1 minimization help overcome problems with too smoothly varying and diminished model changes, characteristics of the L2-norm (Kim et al., 2013).

In this appendix, tests will be shown for all the eight possible configurations of the inversion. For facilitating the analysis, the regularizations will be described as $LX_1LX_2LX_3$, being that LX_1 represents the error minimization, LX_2 represents the regularization in the space domain and LX_3 represents the regularization in the time domains. Therefore, L2L1L2 means that the type of inversion applied L2-norm for error minimization, L1-norm for space domains, and L2-norm for time domain.

Figures C-1-4 shows the results of the inversions in five different times. The general observation in this experiment is that, no matter what regularization is being used, the main effects are seeing. For example, in Figure C-1, all the images shown a growing resistivity zone in the middle of the images, as well as in the last image t5, the overall resistivity decreases, the same occurs for Figures C-2-4.

A full L2-norm inversion was selected for this work, as it represents the inversion that was most consistent between the lines and that correlated best with the ground truth presented for STAR (coring, TarGOST®, temperature and combustion gas concentration).

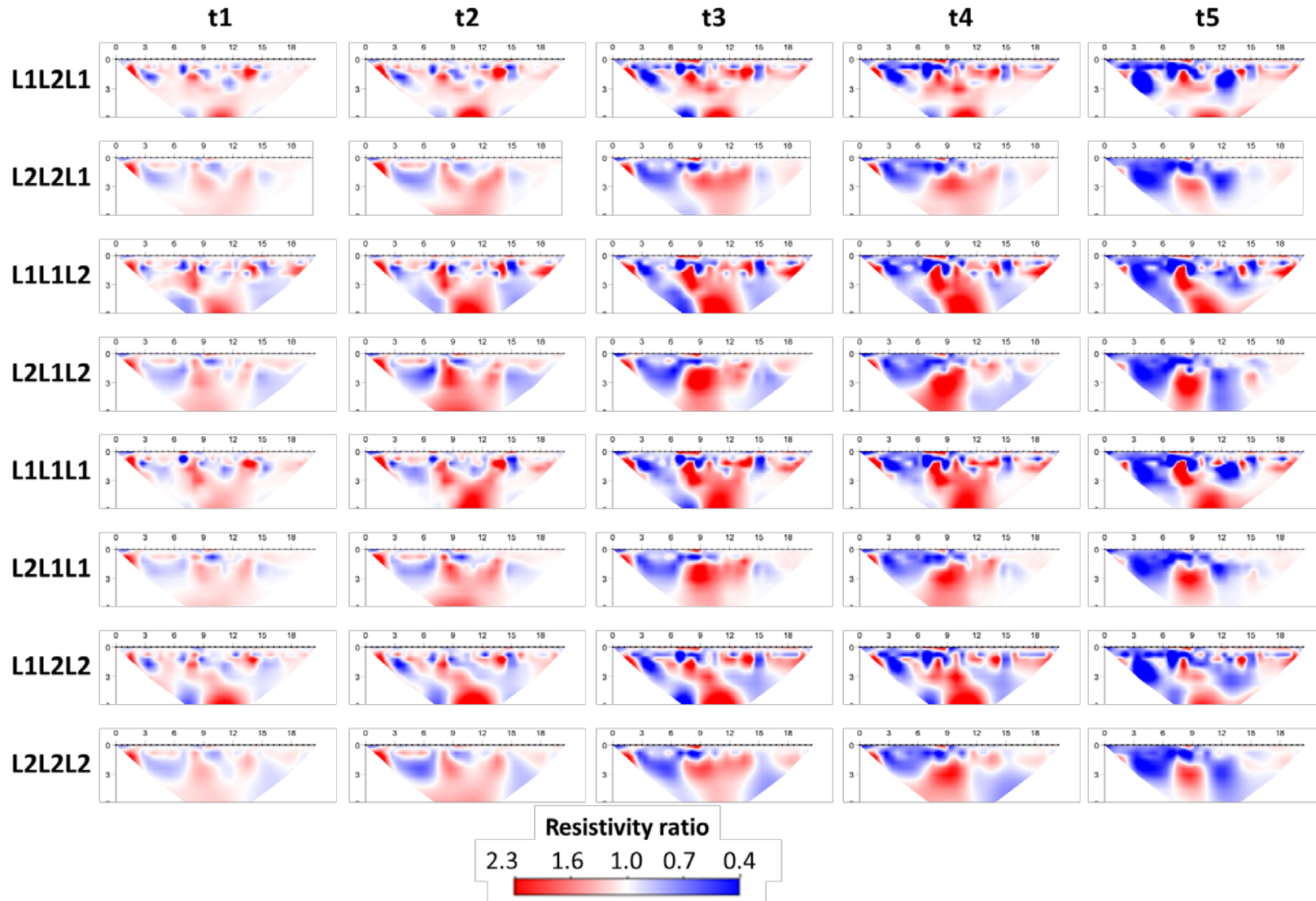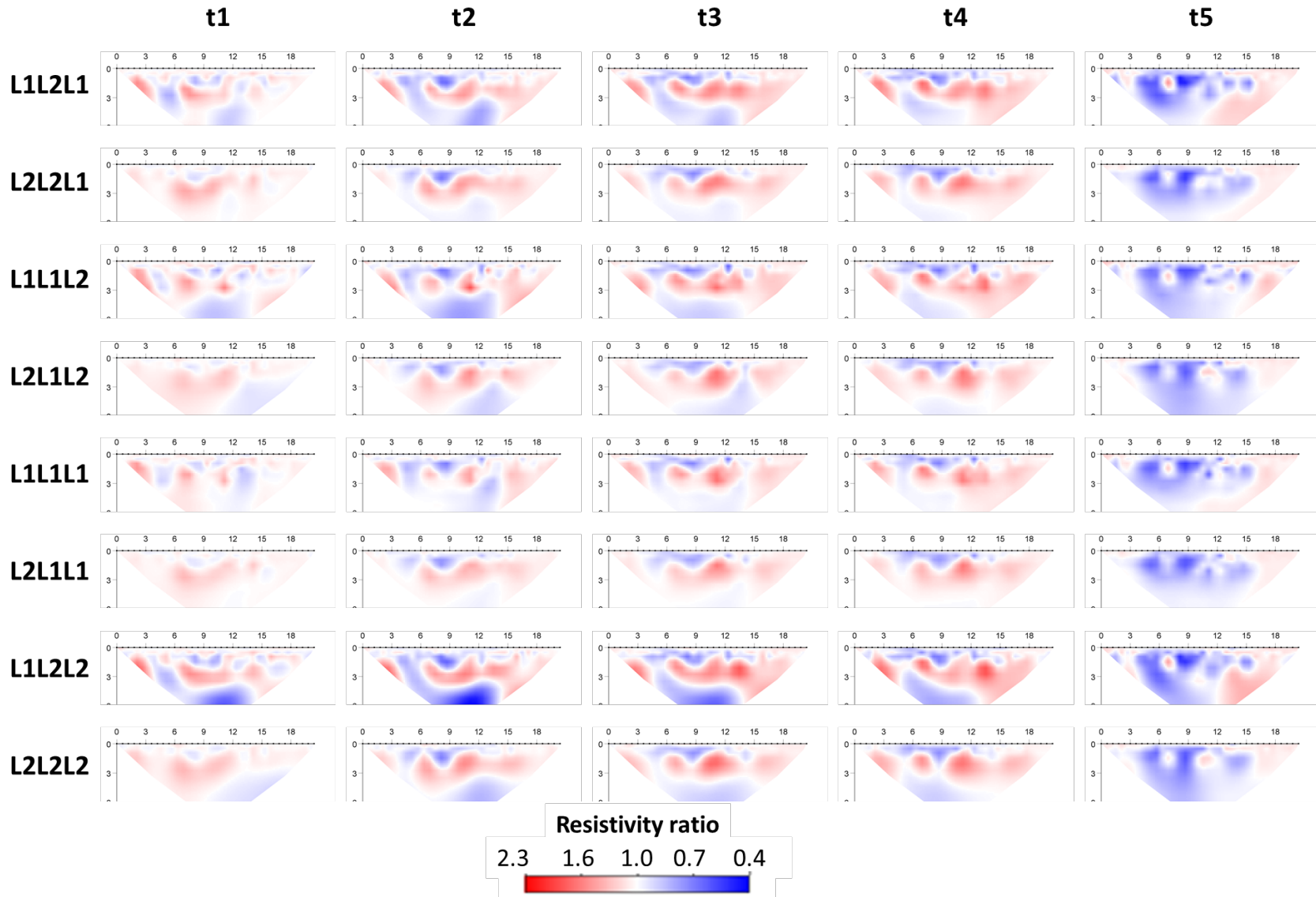**Figure C-1.** Regularization analysis for the shallow cell line S-N. Depth and distance are in meters.

Figure C-2. Regularization analysis for the shallow cell line W-E. Depth and distance are in meters.
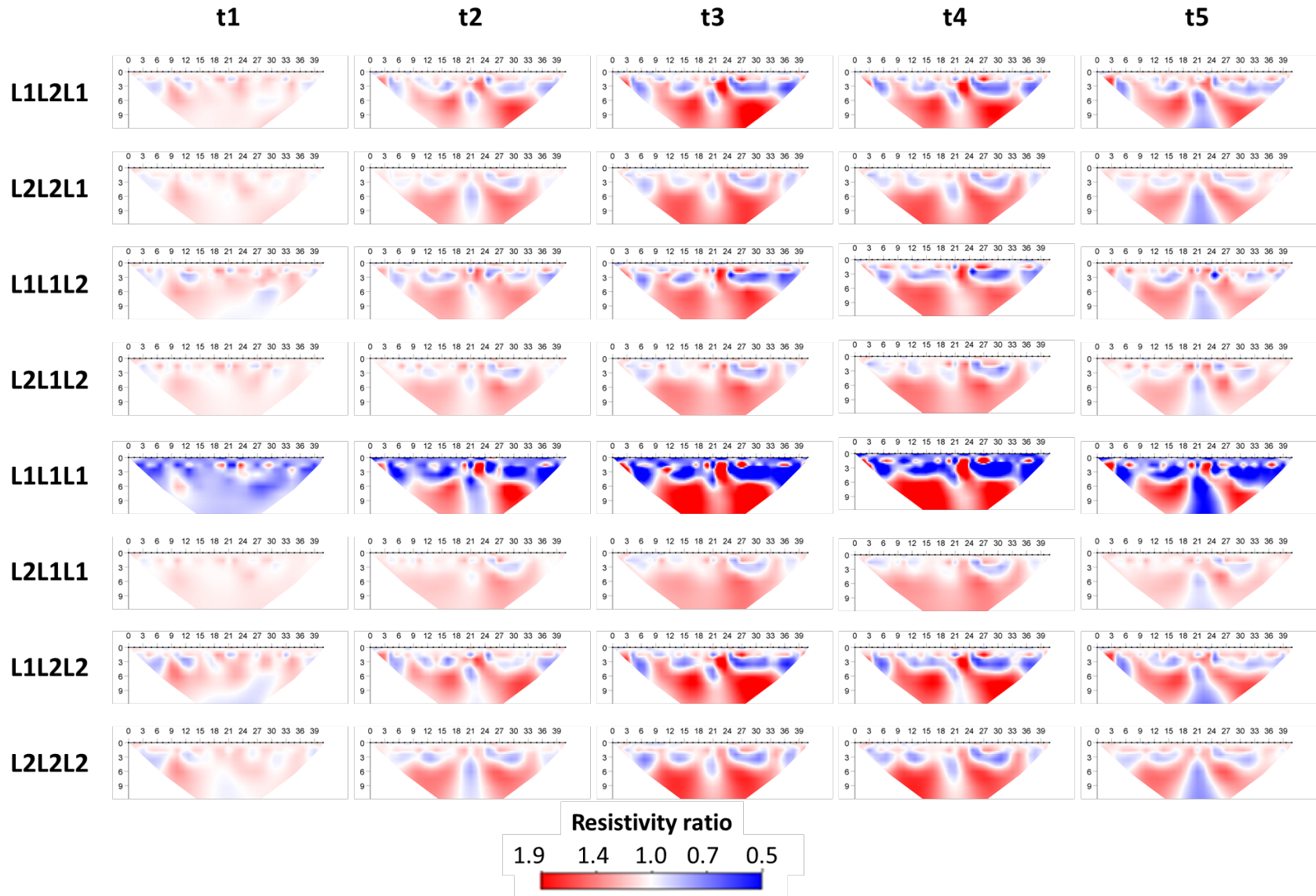
Figure C-3. Regularization analysis for the deep cell line S-N. Depth and distance are in meters.
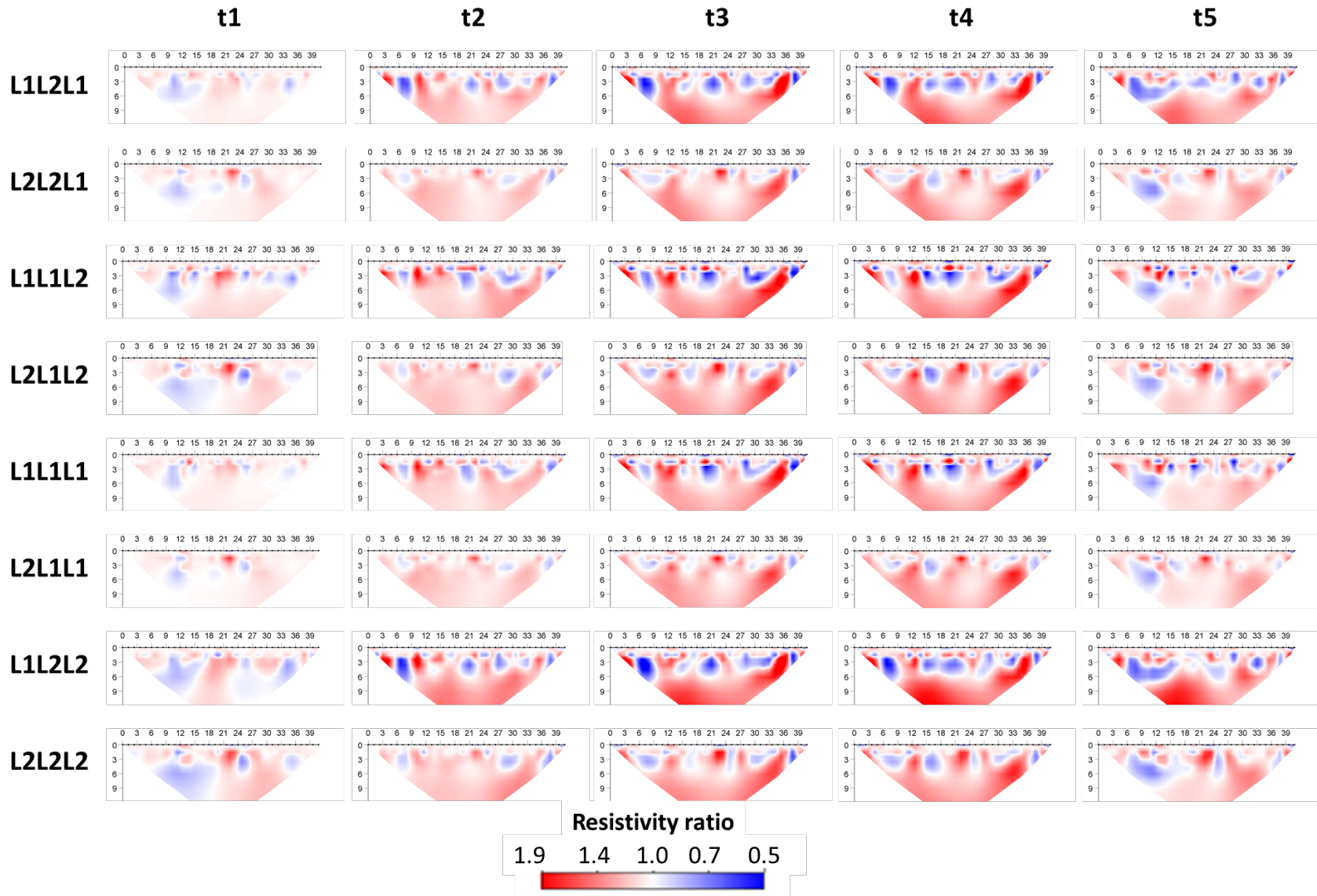
Figure C-4. Regularization analysis for the deep cell line W-E. Depth and distance are in meters.

As mentioned previously, the Lagrangian multipliers for the inversions were kept default. The default setting of the program was developed for L2L2L2 (Yi et al., 2003, Kim et al., 2013). Figure C-5 shows the parameters for the L2L2L2 inversion chosen for this work.
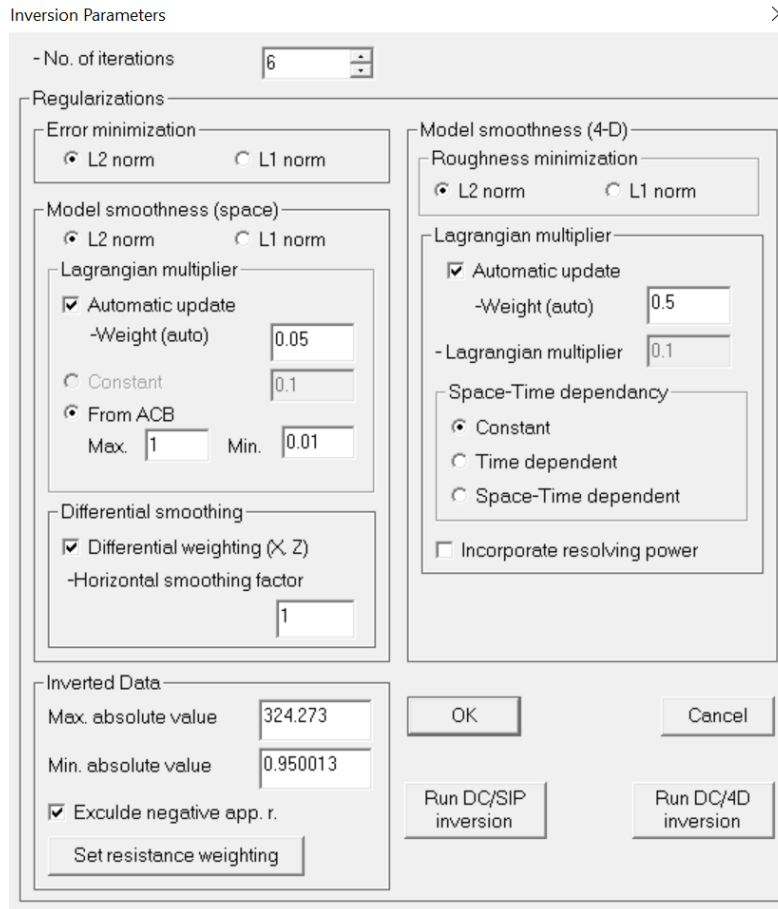
Figure C-5. Menu of the DC_2DPRO inversion software for inversion parameters. Setting for Lagrangian multipliers and L1 vs L2 norms.

References

Kim, J.-H., Supper, R., Tsourlos, P., & Yi, M.-J. (2013). Four-dimensional inversion of resistivity monitoring data through Lp norm minimizations. *Geophysical Journal International, 195*(3), 1640-1656.

Yi, M.-J., Kim, J.-H., & Chung, S.-H. (2003). Enhancing the resolving power of least-squares inversion with active constraint balancing. *Geophysics, 68*(3), 931-941.

APPENDIX D. All inversion results for shallow and deep lines

This appendix presents all the images that were analyzed and filtered during the extend of this project (Figures D-1-4). Tables D-1-4 show the time each image was taken and their assigned time-lapse value compared to image t0.

Table D-1. Shallow Cell Images- Line S-N

Image number	Date	Time	Assigned Time-lapse (days)
t0	2016-08-14	8:22:16 AM	0.00
t1	2016-08-14	1:15:26 PM	0.20
t2	2016-08-14	4:30:24 PM	0.34
t3	2016-08-15	7:43:23 AM	0.97
t4	2016-08-15	10:16:17 AM	1.08
t5	2016-08-15	12:14:45 PM	1.16
t6	2016-08-15	5:49:06 PM	1.39
t7	2016-08-15	7:15:11 PM	1.45
t8	2016-08-15	8:15:10 PM	1.49
t9	2016-08-16	1:15:10 AM	1.70
t10	2016-08-16	8:15:11 AM	1.99
t11	2016-08-16	10:32:34 AM	2.09
t12	2016-08-16	12:37:08 PM	2.18
t13	2016-08-16	4:40:09 PM	2.34
t14	2016-08-17	12:30:10 AM	2.67
t15	2016-08-17	8:53:05 AM	3.02
t16	2016-08-17	11:00:39 AM	3.11
t17	2016-08-17	12:58:17 PM	3.19
t18	2016-08-17	7:00:09 PM	3.44
t19	2016-08-17	9:15:09 PM	3.54

Image number	Date	Time	Assigned Time-lapse (days)
t20	2016-08-18	7:30:09 AM	3.96
t21	2016-08-18	11:01:49 AM	4.11
t22	2016-08-18	4:45:09 PM	4.35
t23	2016-08-18	6:45:09 PM	4.43
t24	2016-08-19	4:45:09 AM	4.85
t25	2016-08-19	1:49:55 PM	5.23
t26	2016-08-19	8:30:54 PM	5.50
t27	2016-08-20	4:30:54 AM	5.84
t28	2016-08-20	12:32:38 PM	6.17
t29	2016-08-20	5:00:09 PM	6.36
t30	2016-08-21	12:00:09 AM	6.65
t31	2016-08-21	5:09:09 AM	6.86
t32	2016-08-21	8:58:02 AM	7.02
t33	2016-08-21	1:51:32 PM	7.23
t34	2016-08-21	4:53:15 PM	7.35
t35	2016-08-21	6:34:03 PM	7.42
t36	2016-08-21	8:14:51 PM	7.49
t37	2016-08-21	8:48:27 PM	7.52
t38	2016-08-21	9:22:03 PM	7.54
t39	2016-08-22	1:50:51 AM	7.73
t40	2016-08-22	5:12:27 AM	7.87
t41	2016-08-22	6:53:15 AM	7.94

Resistivity ratio
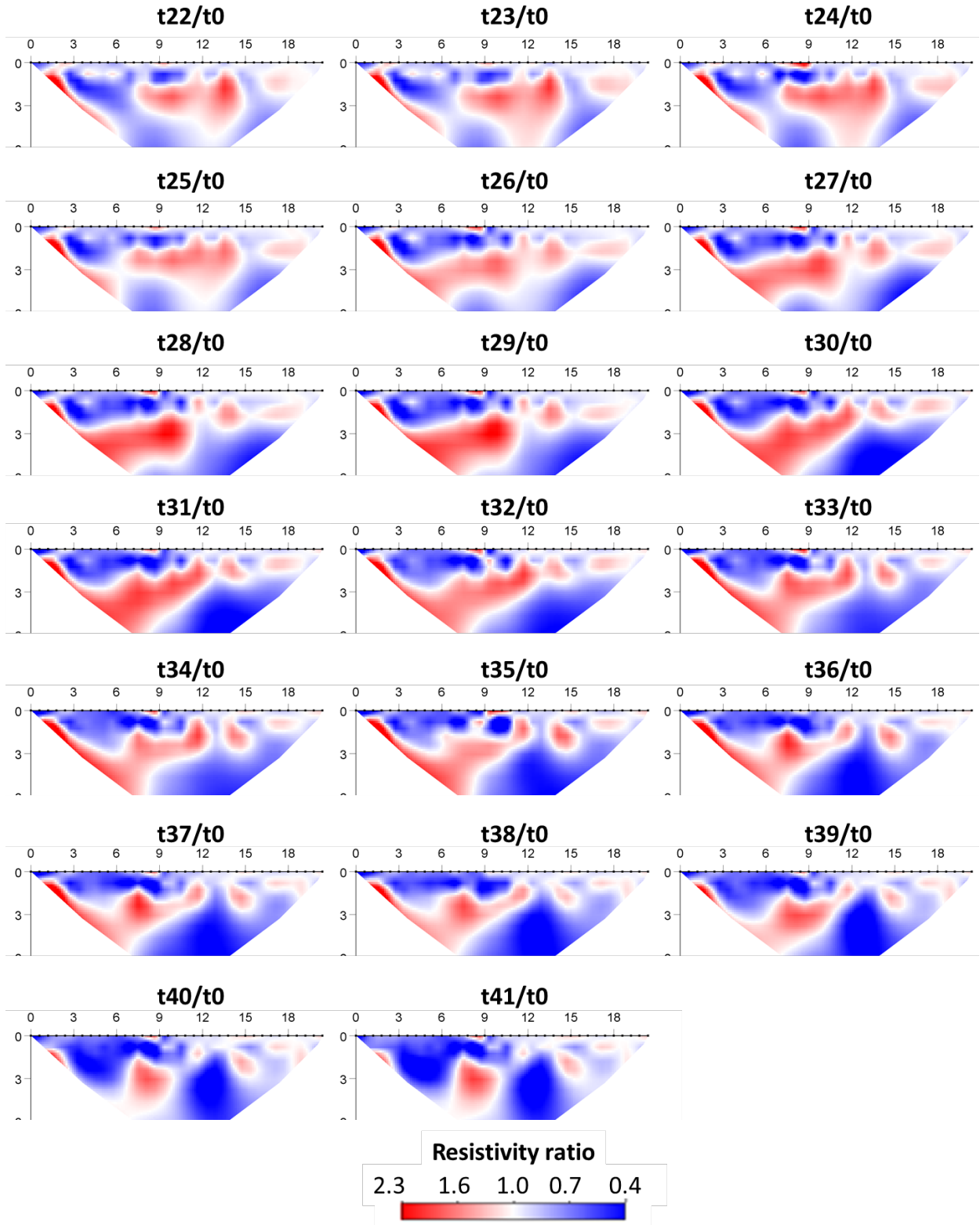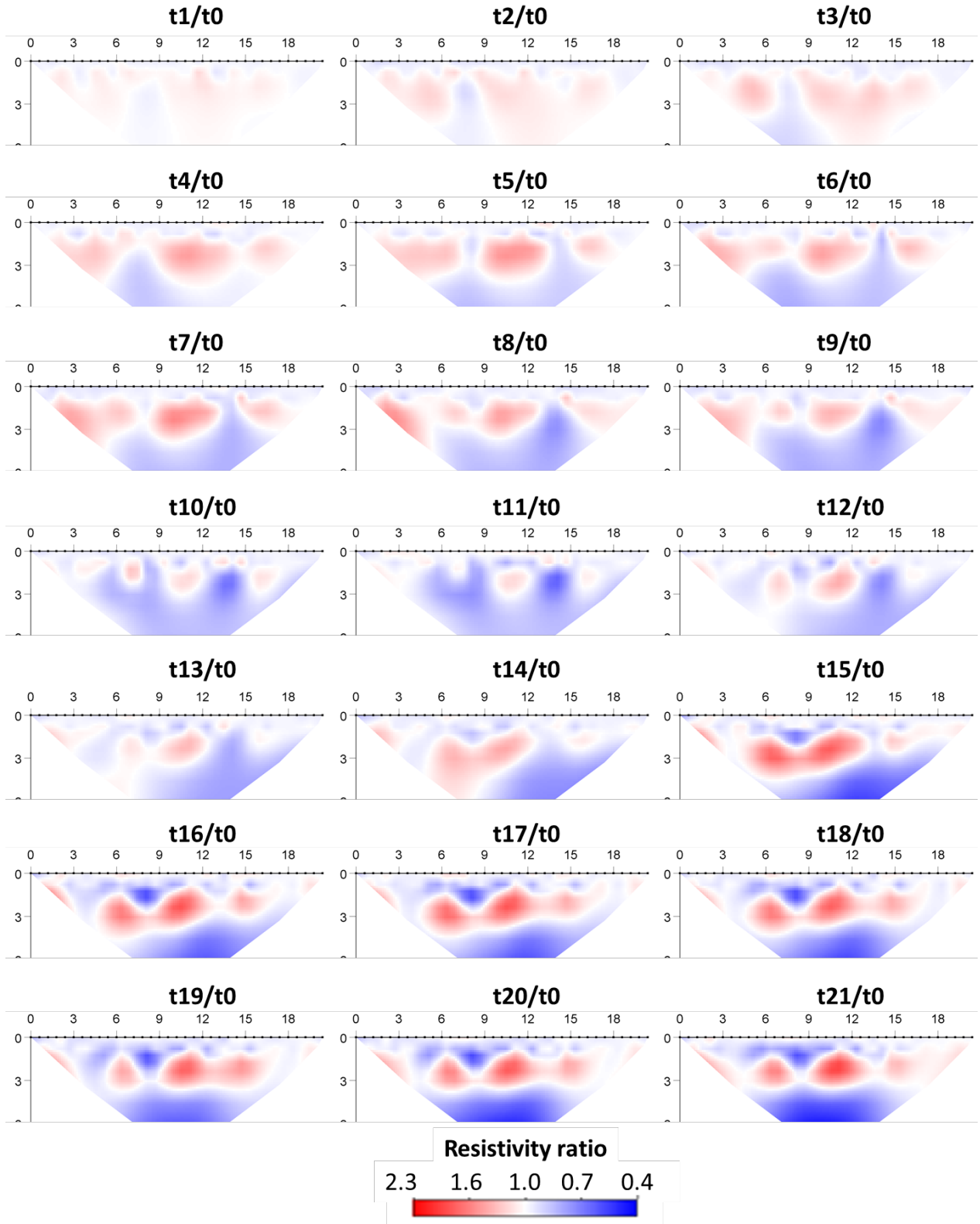
2.3 1.6 1.0 0.7 0.4

107
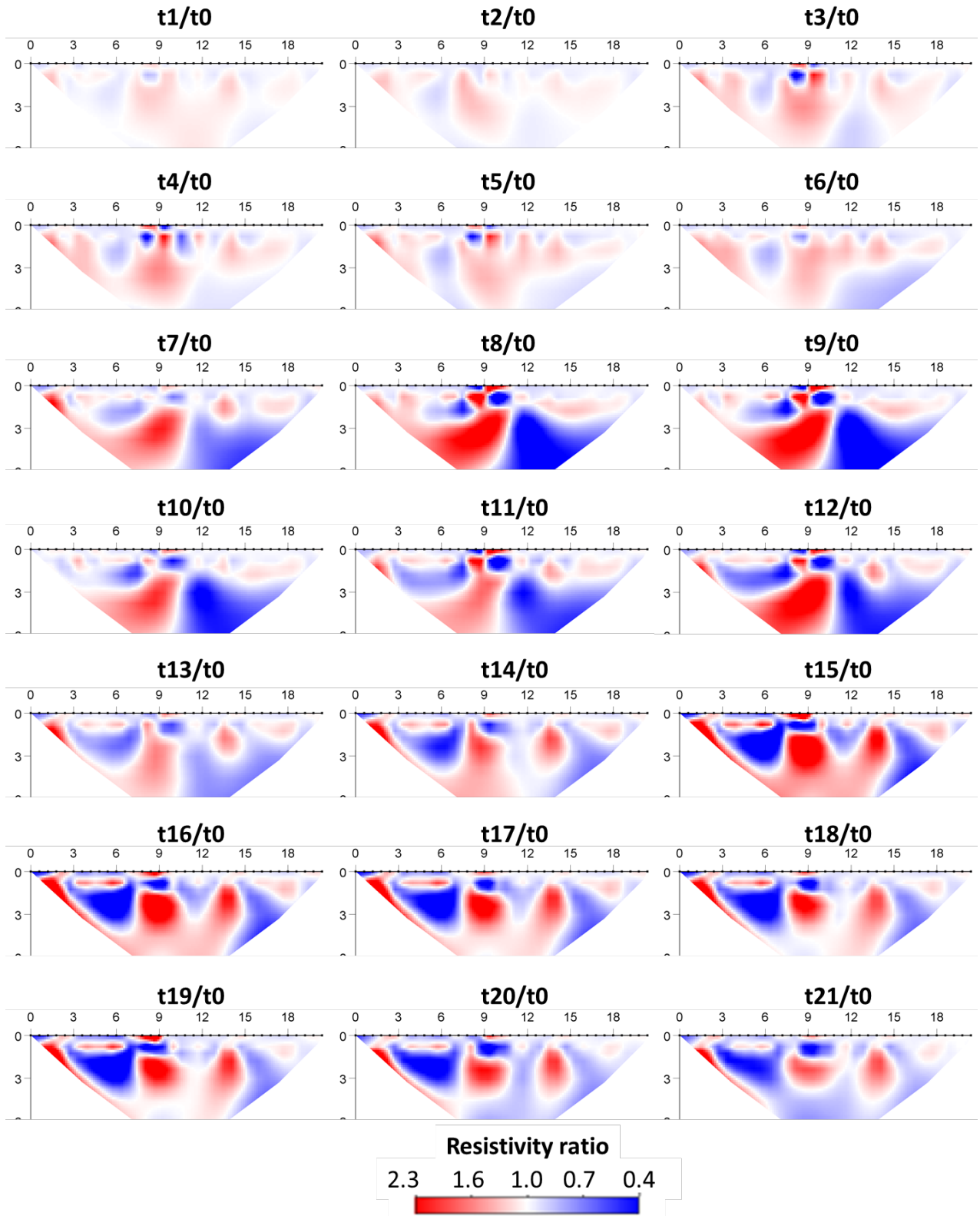
Figure D-1. All 42 images for shallow cell in Line W-E.

Table D-2. Shallow Cell Images - Line W-E

Image number	Date	Time	Assigned Time-lapse (days)
t0	2016-08-14	8:28:10 AM	0.00
t1	2016-08-14	1:23:30 PM	0.21
t2	2016-08-14	4:42:55 PM	0.35
t3	2016-08-14	6:28:09 PM	0.42
t4	2016-08-15	7:51:45 AM	0.98
t5	2016-08-15	10:10:40 AM	1.07
t6	2016-08-15	12:49:29 PM	1.18
t7	2016-08-15	6:12:09 PM	1.41
t8	2016-08-15	7:30:10 PM	1.46
t9	2016-08-15	8:30:10 PM	1.50
t10	2016-08-16	1:30:10 AM	1.71
t11	2016-08-16	8:30:10 AM	2.00
t12	2016-08-16	10:38:58 AM	2.09
t13	2016-08-16	12:47:31 PM	2.18
t14	2016-08-16	4:53:01 PM	2.35
t15	2016-08-17	12:42:33 AM	2.68
t16	2016-08-17	9:01:19 AM	3.03
t17	2016-08-17	11:06:29 AM	3.11
t18	2016-08-17	1:03:23 PM	3.19
t19	2016-08-17	7:13:06 PM	3.45
t20	2016-08-17	9:27:34 PM	3.54
t21	2016-08-18	7:42:57 AM	3.97
t22	2016-08-18	11:08:49 AM	4.11
t23	2016-08-18	4:57:42 PM	4.36
t24	2016-08-18	10:57:26 PM	4.61
t25	2016-08-19	4:57:26 AM	4.86

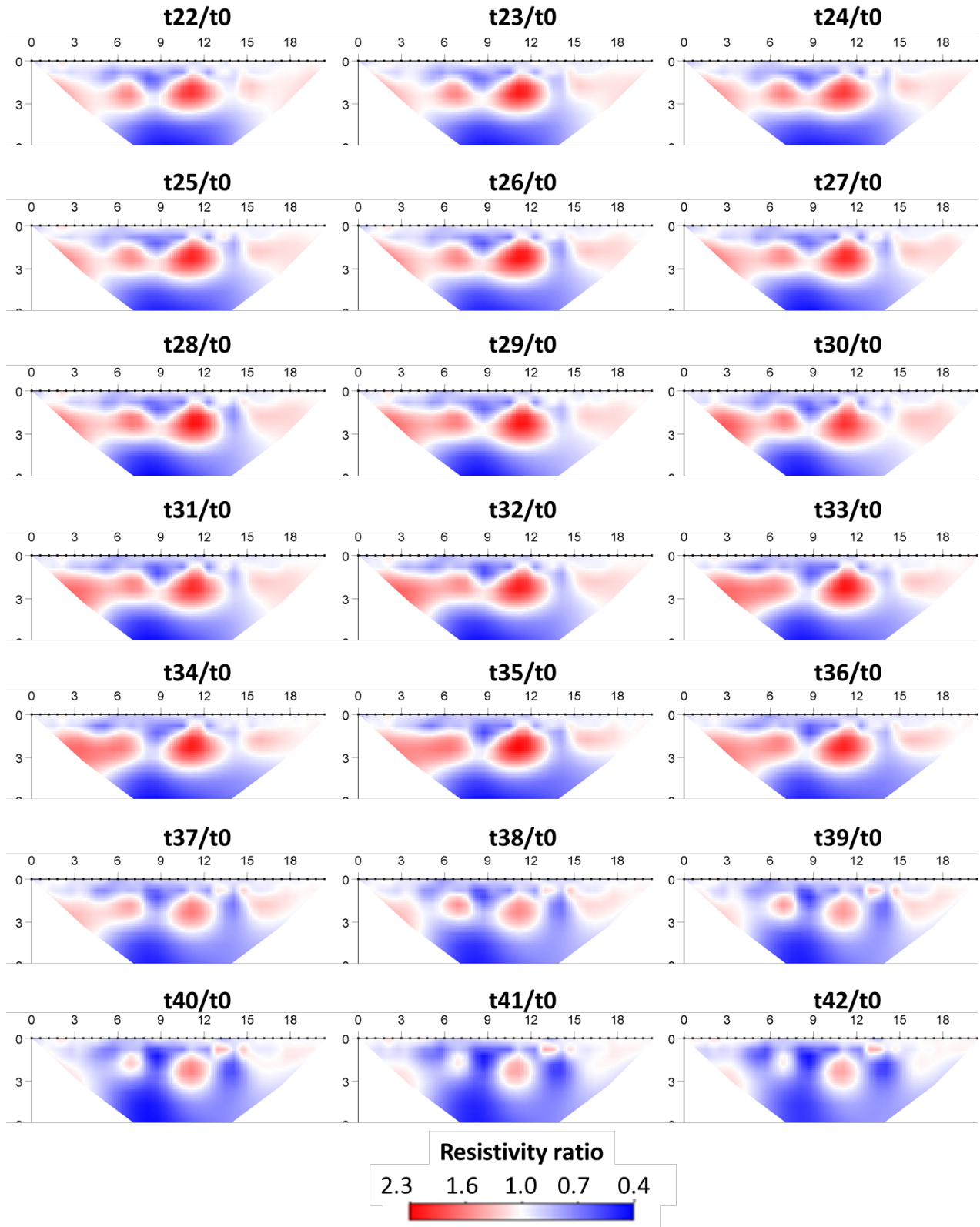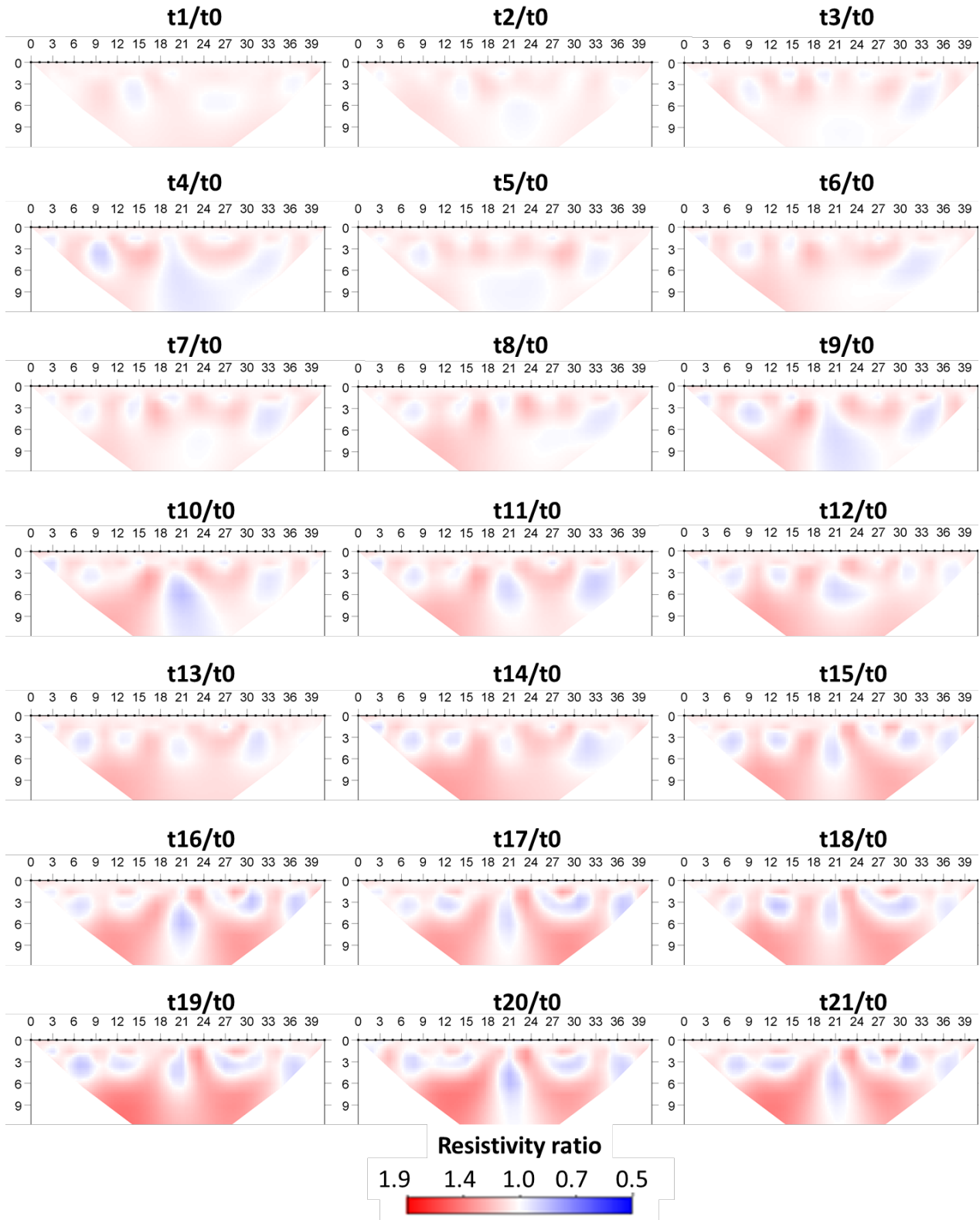| Image number	Date	Time	Assigned Time-lapse (days)
t26	2016-08-19	1:55:17 PM	5.23
t27	2016-08-19	8:43:18 PM	5.51
t28	2016-08-20	4:43:14 AM	5.85
t29	2016-08-20	12:13:59 PM	6.16
t30	2016-08-20	5:12:50 PM	6.37
t31	2016-08-21	12:12:23 AM	6.66
t32	2016-08-21	5:12:16 AM	6.87
t33	2016-08-21	9:24:27 AM	7.04
t34	2016-08-21	1:32:01 PM	7.21
t35	2016-08-21	5:07:52 PM	7.36
t36	2016-08-21	6:47:59 PM	7.43
t37	2016-08-21	8:28:52 PM	7.50
t38	2016-08-21	9:02:34 PM	7.53
t39	2016-08-21	9:36:08 PM	7.55
t40	2016-08-22	2:05:08 AM	7.74
t41	2016-08-22	5:26:43 AM	7.88
t42	2016-08-22	7:07:45 AM	7.95

Figure D-2. All 43 images for shallow cell in Line S-N.

Table D-3. Deep Cell Images - Line S-N

Image number	Date	Time	Assigned Time-lapse (days)
t0	2016-08-26	3:09:41 PM	0.00
t1	2016-08-26	4:16:04 PM	0.05
t2	2016-08-26	5:26:57 PM	0.10
t3	2016-08-26	7:16:45 PM	0.17
t4	2016-08-27	3:21:19 AM	0.51
t5	2016-08-27	6:17:43 AM	0.63
t6	2016-08-27	7:45:55 AM	0.69
t7	2016-08-27	2:40:33 PM	0.98
t8	2016-08-27	4:49:09 PM	1.07
t9	2016-08-27	9:05:21 PM	1.25
t10	2016-08-28	3:47:57 AM	1.53
t11	2016-08-28	5:37:45 AM	1.60
t12	2016-08-28	6:50:57 AM	1.65
t13	2016-08-28	7:27:33 AM	1.68
t14	2016-08-28	8:04:09 AM	1.70
t15	2016-08-28	1:29:10 PM	1.93
t16	2016-08-28	2:09:33 PM	1.96
t17	2016-08-28	2:42:56 PM	1.98
t18	2016-08-28	4:57:05 PM	2.07
t19	2016-08-28	6:05:43 PM	2.12
t20	2016-08-28	6:40:10 PM	2.15
t21	2016-08-28	7:14:44 PM	2.17
t22	2016-08-28	8:21:47 PM	2.22
t23	2016-08-28	9:28:46 PM	2.26
t24	2016-08-28	11:08:13 PM	2.33
t25	2016-08-29	12:48:12 AM	2.40

Image number	Date	Time	Assigned Time-lapse (days)
t26	2016-08-29	1:54:27 AM	2.45
t27	2016-08-29	3:00:58 AM	2.49
t28	2016-08-29	4:40:21 AM	2.56
t29	2016-08-29	6:20:09 AM	2.63
t30	2016-08-29	7:28:06 AM	2.68
t31	2016-08-29	8:42:00 AM	2.73
t32	2016-08-29	12:09:10 PM	2.87
t33	2016-08-29	2:16:58 PM	2.96
t34	2016-08-29	5:07:22 PM	3.08
t35	2016-08-29	9:22:58 PM	3.26
t36	2016-08-30	12:13:22 AM	3.38
t37	2016-08-30	3:03:46 AM	3.50
t38	2016-08-30	9:11:45 AM	3.75
t39	2016-08-30	5:49:21 PM	4.11
t40	2016-08-30	6:31:57 PM	4.14
t41	2016-08-30	10:47:33 PM	4.32
t42	2016-08-31	8:01:21 AM	4.70
t43	2016-08-31	1:22:48 PM	4.93
t44	2016-08-31	6:19:21 PM	5.13
t45	2016-09-01	11:08:58 AM	5.83
t46	2016-09-01	2:41:59 PM	5.98
t47	2016-09-01	8:22:46 PM	6.22
t48	2016-09-02	4:11:22 AM	6.54
t49	2016-09-02	7:44:22 AM	6.69
t50	2016-09-02	11:09:09 AM	6.83
t51	2016-09-02	1:16:57 PM	6.92
t52	2016-09-02	6:17:27 PM	7.13

Image number	Date	Time	Assigned Time-lapse (days)
t53	2016-09-02	9:00:21 PM	7.24
t54	2016-09-03	1:31:51 AM	7.43
t55	2016-09-03	3:20:27 AM	7.51
t56	2016-09-03	5:09:03 AM	7.58
t57	2016-09-03	9:40:33 AM	7.77

Resistivity ratio

1.9   1.4   1.0   0.7   0.5

Resistivity ratio

1.9   1.4   1.0   0.7   0.5
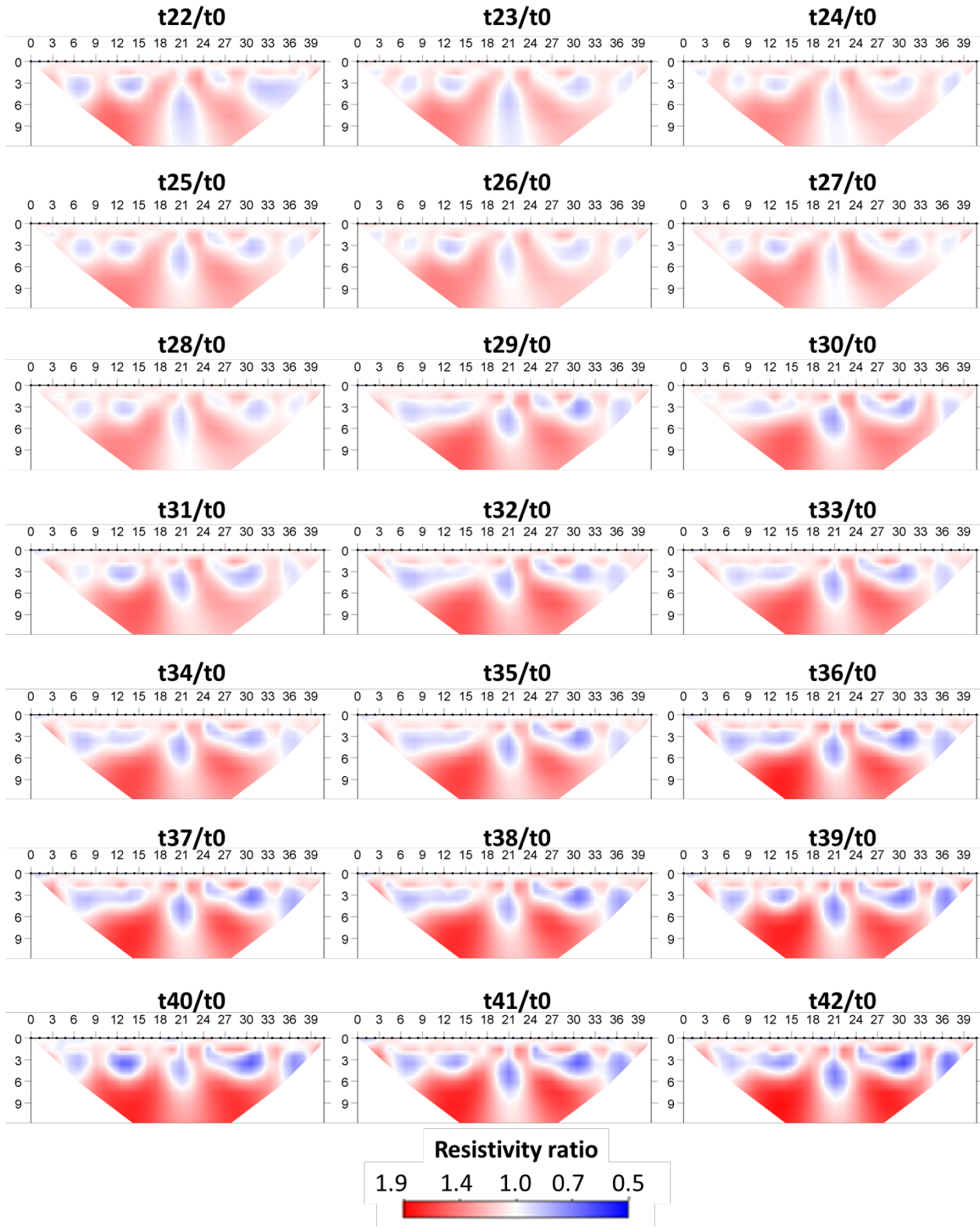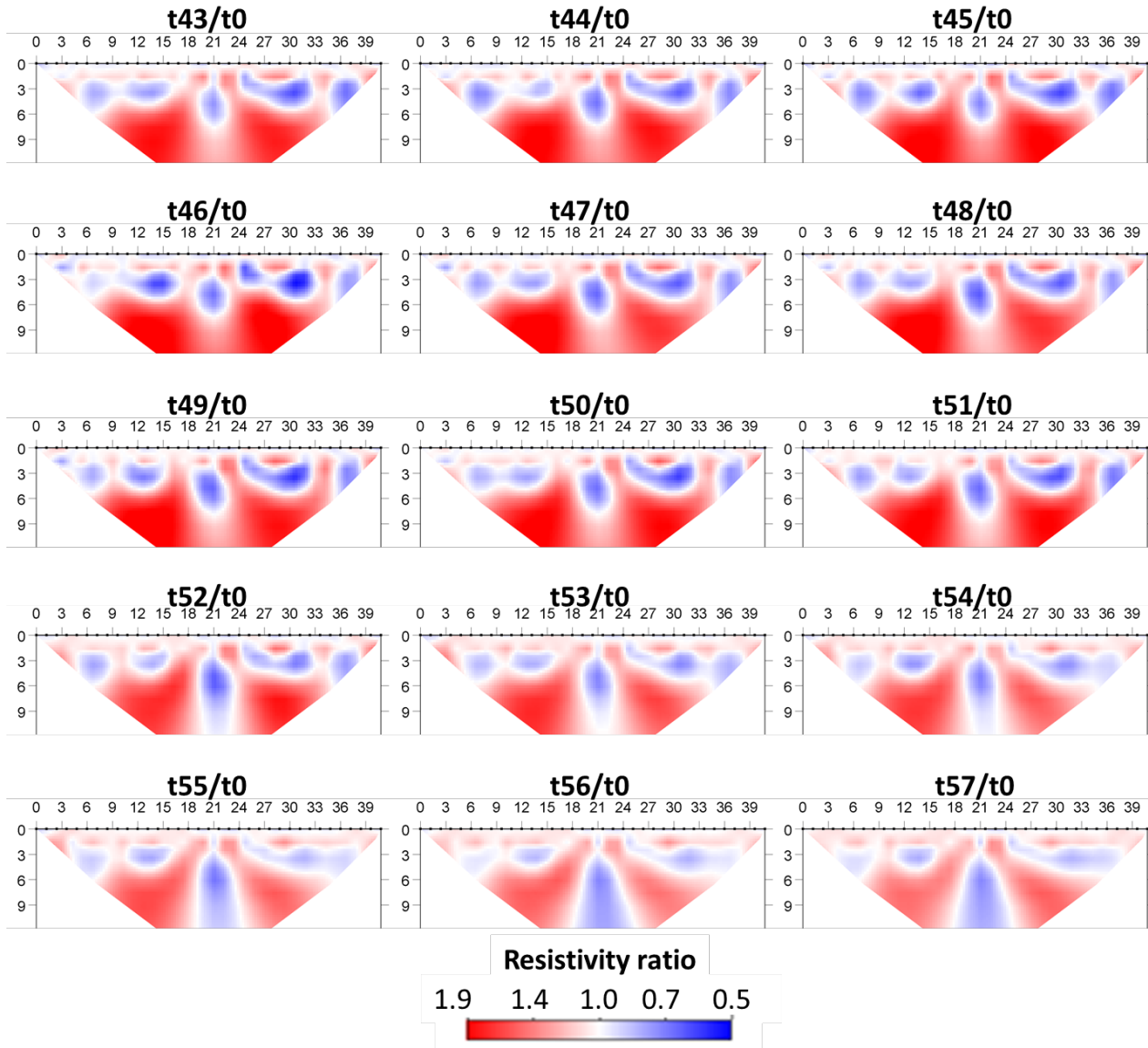
Figure D-3. All 58 images for deep cell in Line S-N.

Image number	Date	Time	Assigned Time-lapse (days)
t0	2016-08-26	3:23:11 PM	0.01
t1	2016-08-26	4:29:34 PM	0.06
t2	2016-08-26	5:40:41 PM	0.10
t3	2016-08-26	7:30:19 PM	0.18
t4	2016-08-27	3:41:25 AM	0.52
t5	2016-08-27	6:37:49 AM	0.64
t6	2016-08-27	8:06:01 AM	0.71
t7	2016-08-27	2:54:09 PM	0.99
t8	2016-08-27	5:02:45 PM	1.08
t9	2016-08-27	9:18:50 PM	1.26
t10	2016-08-28	4:01:26 AM	1.54
t11	2016-08-28	5:51:11 AM	1.61
t12	2016-08-28	7:04:35 AM	1.66
t13	2016-08-28	7:41:26 AM	1.69
t14	2016-08-28	8:18:26 AM	1.71
t15	2016-08-28	1:42:42 PM	1.94
t16	2016-08-28	2:23:10 PM	1.97
t17	2016-08-28	2:56:30 PM	1.99
t18	2016-08-28	5:11:04 PM	2.08
t19	2016-08-28	6:19:58 PM	2.13
t20	2016-08-28	6:54:25 PM	2.16
t21	2016-08-28	7:28:28 PM	2.18
t22	2016-08-28	8:35:38 PM	2.23
t23	2016-08-28	9:42:15 PM	2.27
t24	2016-08-28	11:21:52 PM	2.34
t25	2016-08-29	12:28:34 AM	2.39

Image number	Date	Time	Assigned Time-lapse (days)
t26	2016-08-29	2:07:59 AM	2.46
t27	2016-08-29	3:14:27 AM	2.50
t28	2016-08-29	4:54:03 AM	2.57
t29	2016-08-29	6:34:00 AM	2.64
t30	2016-08-29	7:47:32 AM	2.69
t31	2016-08-29	12:22:57 PM	2.88
t32	2016-08-29	2:30:28 PM	2.97
t33	2016-08-29	5:21:10 PM	3.09
t34	2016-08-29	9:36:30 PM	3.27
t35	2016-08-30	1:51:58 AM	3.45
t36	2016-08-30	3:17:20 AM	3.51
t37	2016-08-30	9:25:14 AM	3.76
t38	2016-08-30	6:03:23 PM	4.12
t39	2016-08-30	6:45:59 PM	4.15
t40	2016-08-30	11:01:11 PM	4.33
t41	2016-08-31	8:15:10 AM	4.71
t42	2016-08-31	1:36:21 PM	4.94
t43	2016-08-31	6:33:27 PM	5.14
t44	2016-09-01	11:22:53 AM	5.84
t45	2016-09-01	2:56:33 PM	5.99
t46	2016-09-01	8:33:11 PM	6.22
t47	2016-09-02	4:24:49 AM	6.55
t48	2016-09-02	7:58:11 AM	6.70
t49	2016-09-02	11:22:58 AM	6.84
t50	2016-09-02	1:31:00 PM	6.93
t51	2016-09-02	6:21:49 PM	7.13
t52	2016-09-02	9:14:56 PM	7.25

Image number	Date	Time	Assigned Time-lapse (days)
t53	2016-09-03	1:46:32 AM	7.44
t54	2016-09-03	3:35:24 AM	7.52
t55	2016-09-03	5:23:44 AM	7.59
t56	2016-09-03	8:07:26 AM	7.71

t1/t0   t2/t0   t3/t0

t4/t0   t5/t0   t6/t0

t7/t0   t8/t0   t9/t0

t10/t0   t11/t0   t12/t0

t13/t0   t14/t0   t15/t0

t16/t0   t17/t0   t18/t0

t19/t0   t20/t0   t21/t0

Resistivity ratio

1.9   1.4   1.0   0.7   0.5

Resistivity ratio

1.9   1.4   1.0   0.7   0.5
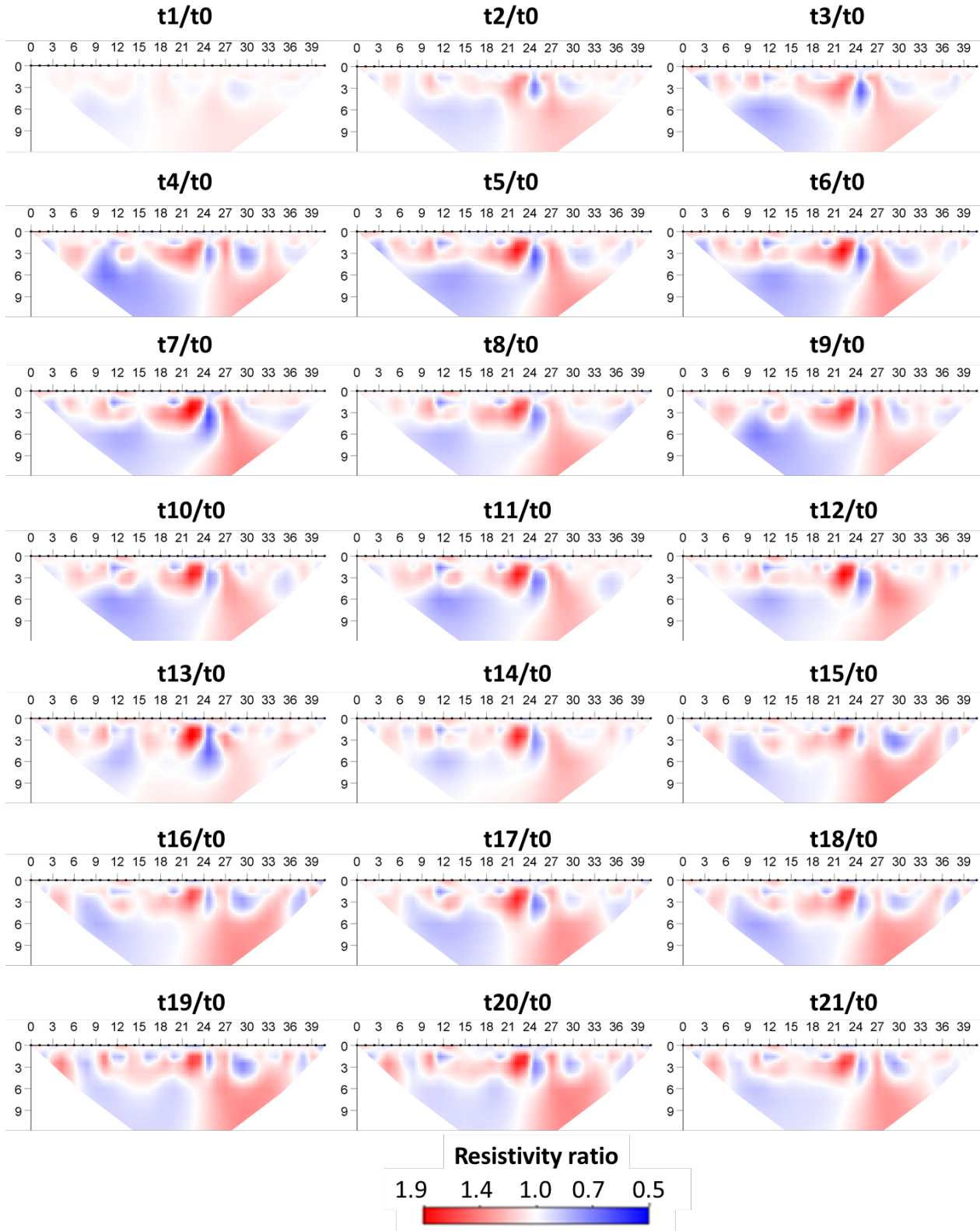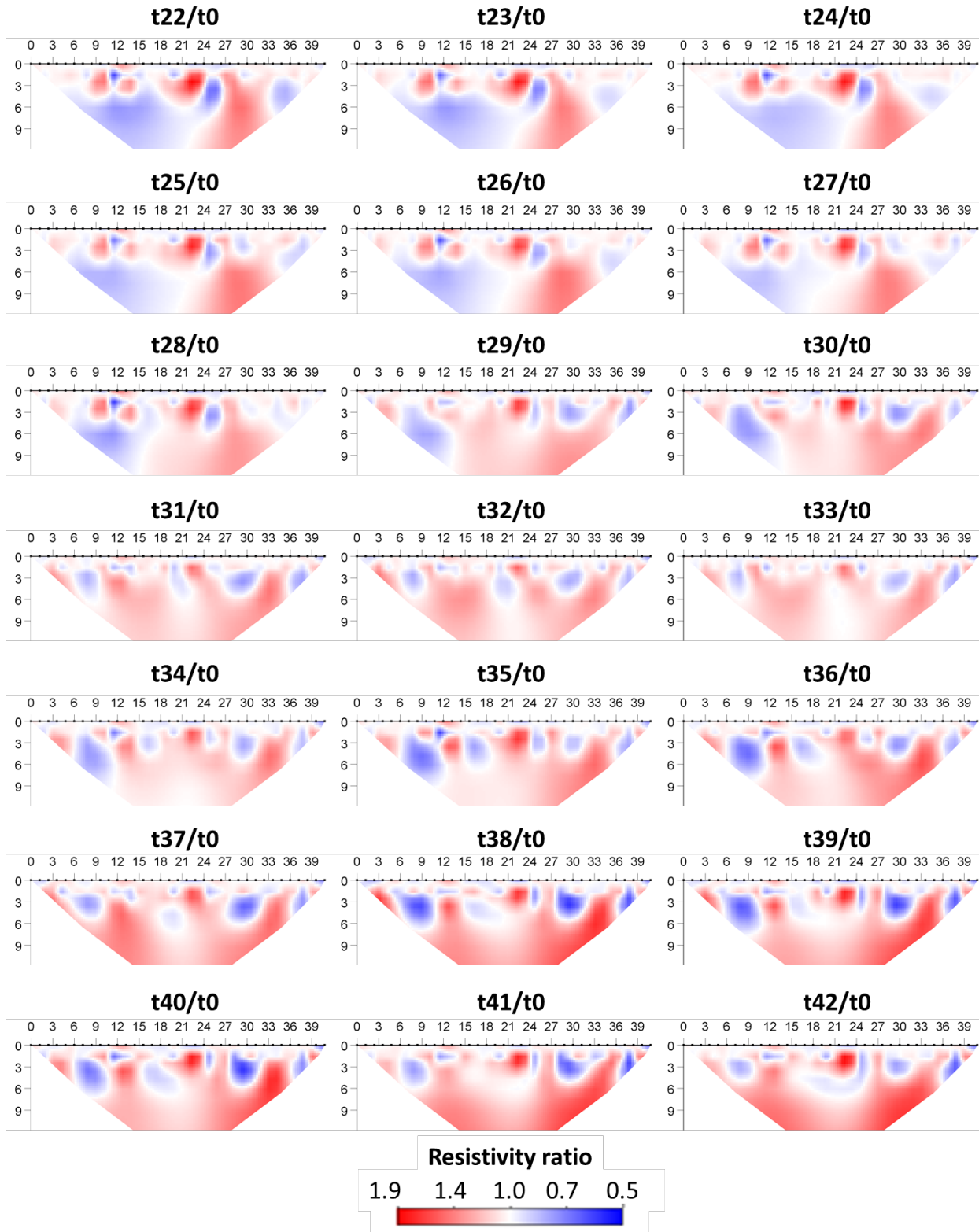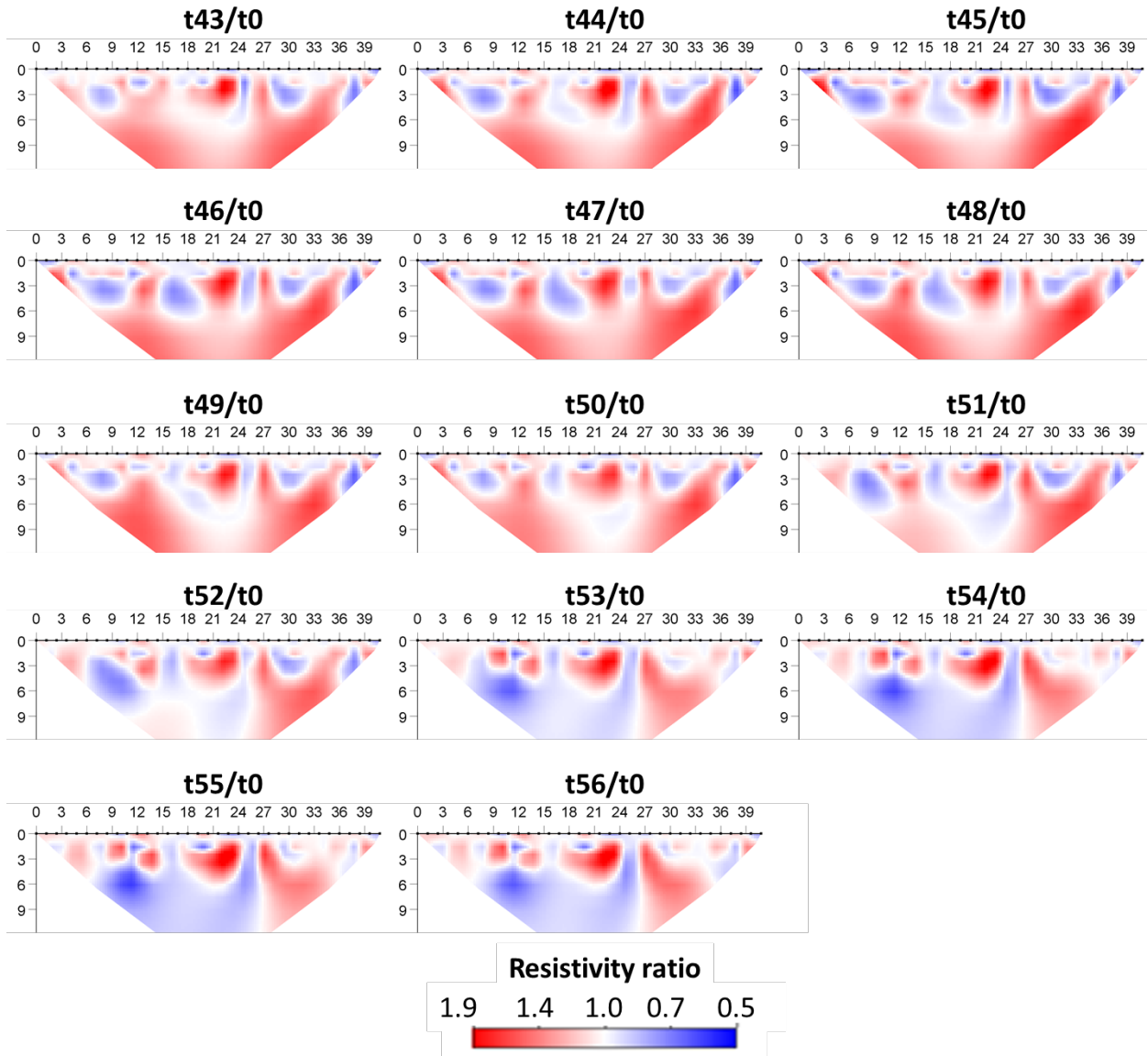
Figure D-4. All 57 images for deep cell in Line W-E.

APPENDIX E. Laboratory experiments

This appendix will show a set of experiments that were conducted in University of Thessaloniki, Thessaloniki, Greece divided in two objectives: i) to identify resistive and conductive moving targets, ii) to conduct experiments with a heater. The objectives of experimenting with resistive and conductive targets were to identify the interferences that would be seen during the field work (specially from metals) and to perform simplistic experiments on what would be expected from the smouldering reaction (conductive and resistive zones) and how they would interfere with each other. The experimental design involved a plastic/fiber tank (80 x 115 centimeters) filled with water, where different targets were added. Electrical Resistivity Tomography (ERT) measurements were conducted in a line of 24 electrodes with a spacing of 3 cm, totalizing 69 cm. The set-up and common targets are shown in Figure E-1. RMS error values for these experiments were in an average of 0.5%.
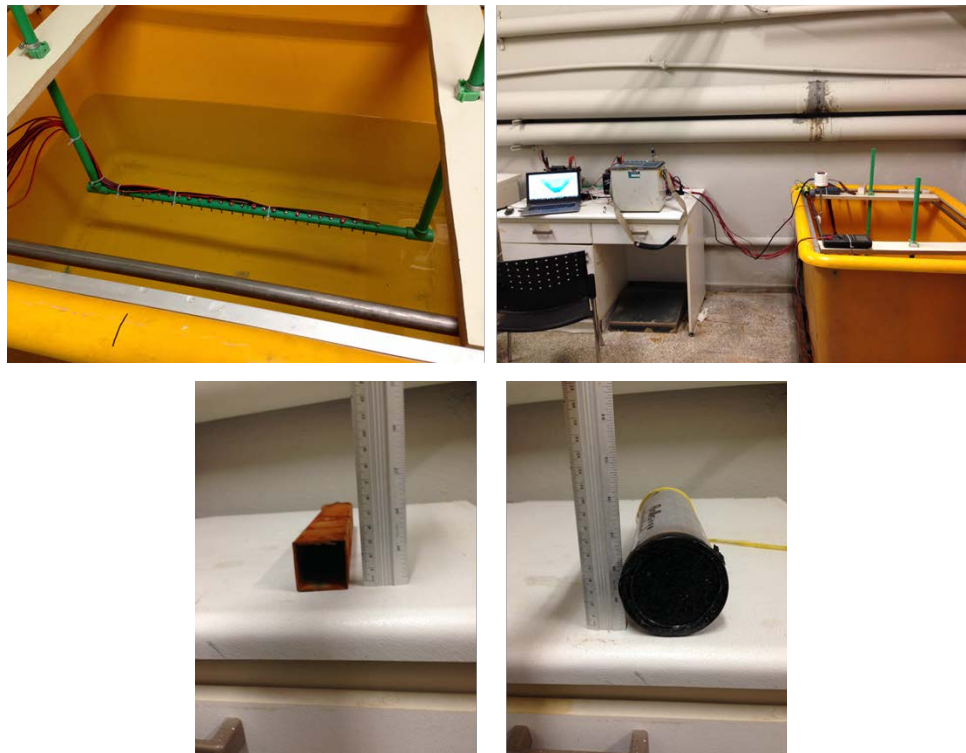

Figure E-1. Set up of the tank experiments. (Top, left) Electrode layout inside the tank and (top, right) tank, with layout connected to the equipment. (Bottom left) Conductive target, (Bottom right) Resistive target.

Conductive versus resistive target

This first experiment consisted in adding a conductive and resistive target to the tank and take measurements to calibrate the equipment, check different arrays, check electrodes and verify depth of penetration of array and sensitivity. The array chosen was dipole-dipole, although experiments were also conducted with multi-gradient arrays. The depth of penetration is about 27 cm, with a resolution/sensitivity being of only 0.18m, that was shown by a conductive region below 0.18m that was not present in the tank. Figure E-2 shows the first experiment.
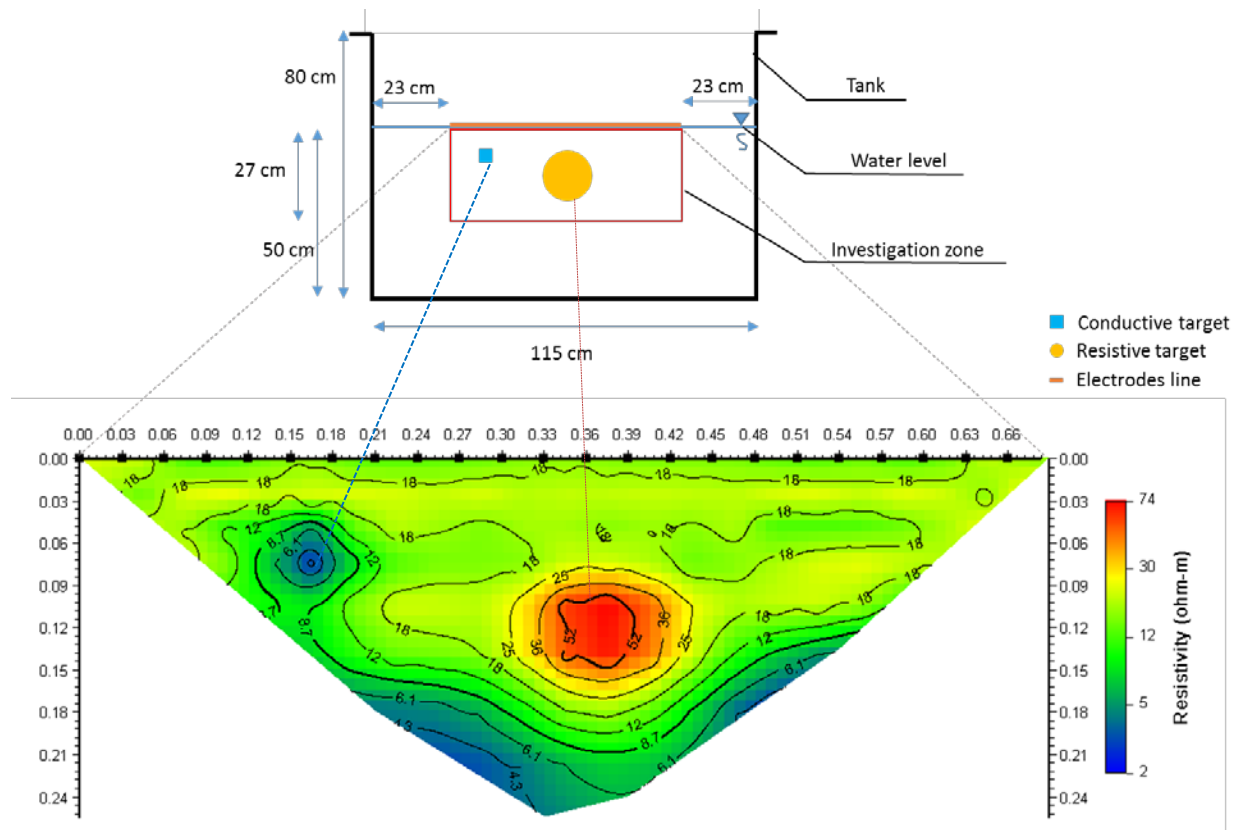
Figure E-2. (Top) Set-up of experiment. (Bottom) independent inversion of the experiment showing a conductive and a resistive target.

Growing conductive target

This experiment was done by adding a conductive target in each of the images on top of the other, as shown in Figure E-2. The objective of this was to see how a growing conductive target would behave using ERT time-lapse inversion.

Results are shown in Figure E-3, where it Is possible to observe the growing of the conductive target, from both the time-lapse images (Figure E-4a) and the ratio images (Figure E-4b).

Figure E-3. Growing conductive target made of metal. Each image represents the addition of one metal bar perpendicular to the electrodes layout.
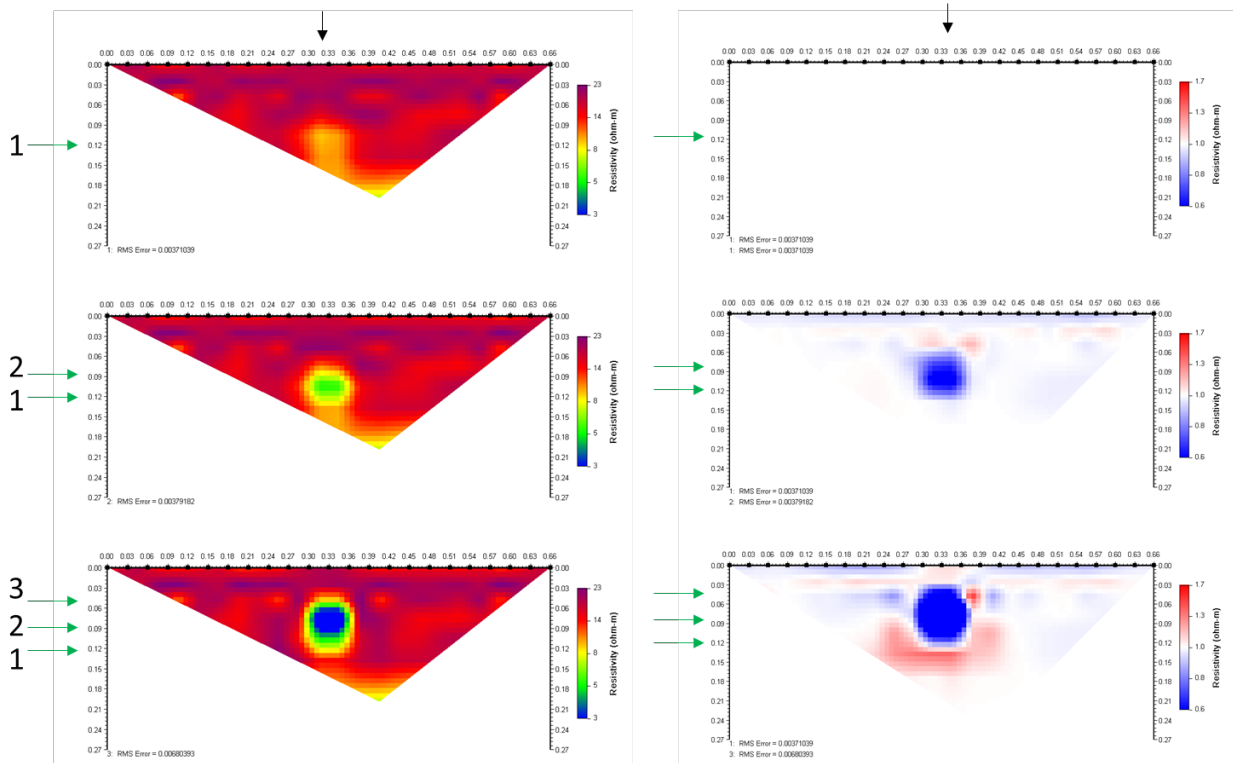

Figure E-4. (Left) Time-lapse images of growing conductive target, as seen in Figure E-3, (right) ratio images. Green arrows indicate position of each conductive target during the data collection. Black arrows indicate the position of the targets on the electrode arrays.

Resistive uplift with static conductive target

This experiment consisted in changing the elevation of the resistive target, while keeping a conductive target static and monitoring the effects with ERT. The experiment set-up is shown in Figure E-5.
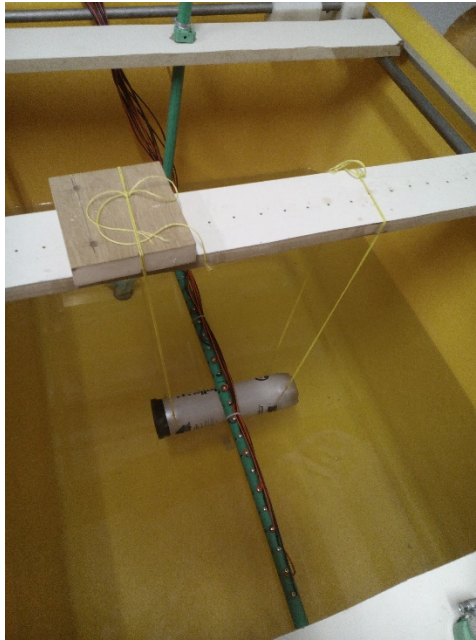

Figure E-5. Resistive target perpendicular to the electrode layout. The target was lifted from 14.2cm, to 11.5cm, 9 cm, 6 cm and 3 cm. Conductive target not shown, but to the left of the resistive target.

Results are shown in Figure E-6, for both time-lapse inversion and ratio images. In the time-lapse inversion, it is possible to observe the interferences of the conductive target. However, the ratio images remove the static interference and focus only on the resistive target moving upwards.
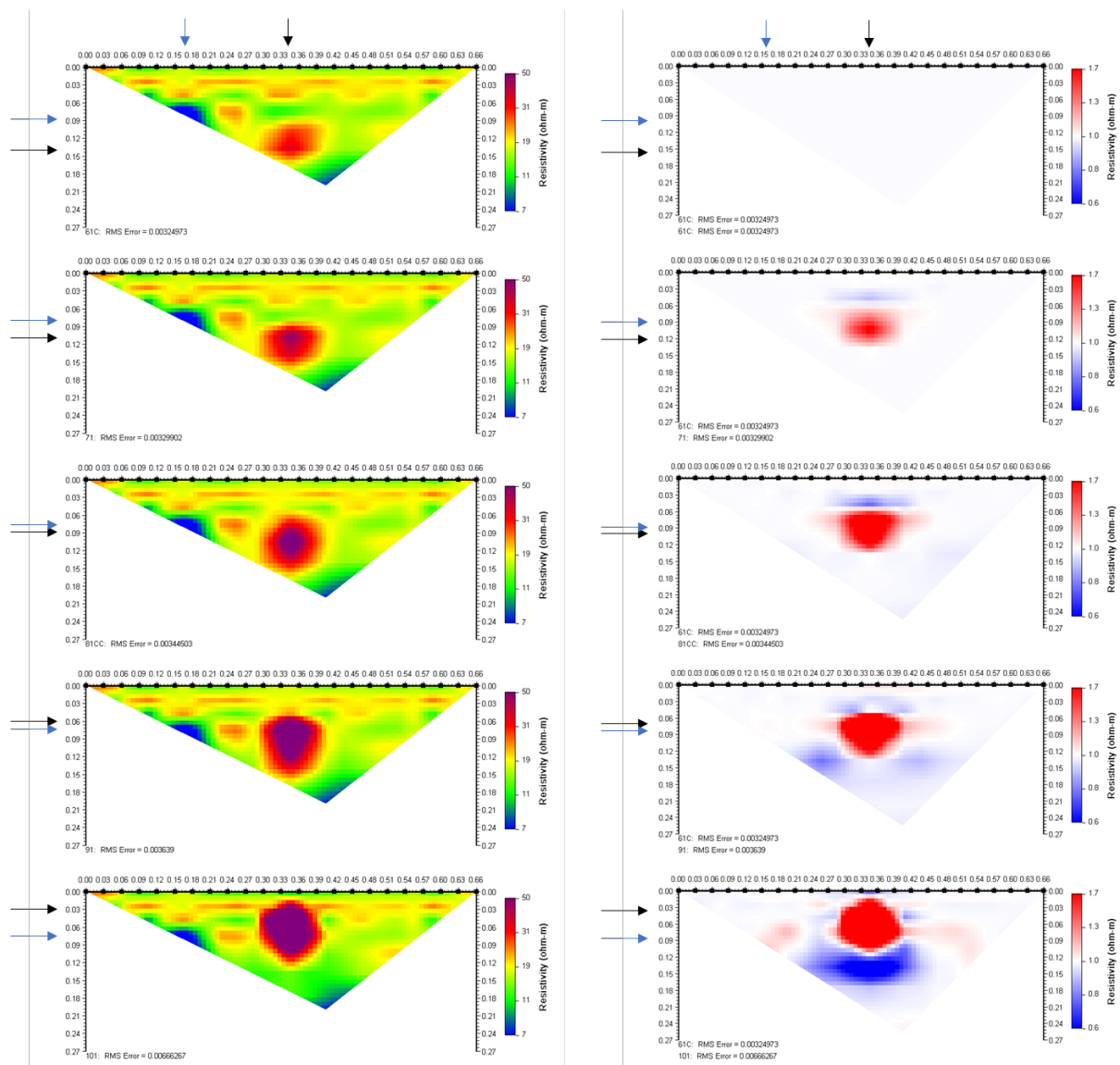
Figure E-6. (Left) Time-lapse images of resistive target uplift with static conductive target, (right) ratio images. Blue arrows indicate position of the static conductive target during the data collection. Black arrows indicate the position of the resistive target moving upward.

Conductive target with vertical pipe

The interferences of a monitoring or ignition well in the ERT line were mimic using a horizontal metal pipe. Figure E-7 shows the vertical pipe anomaly in an independent inversion. The metal pipe is shown in Figure E-8, with a conductive target. A experiment was performed were the metal pipe was static and the conductive target (set up in Figure E-8) would move laterally throughout the electrodes line. Only ratio resistivity results are shown in Figure E-9.
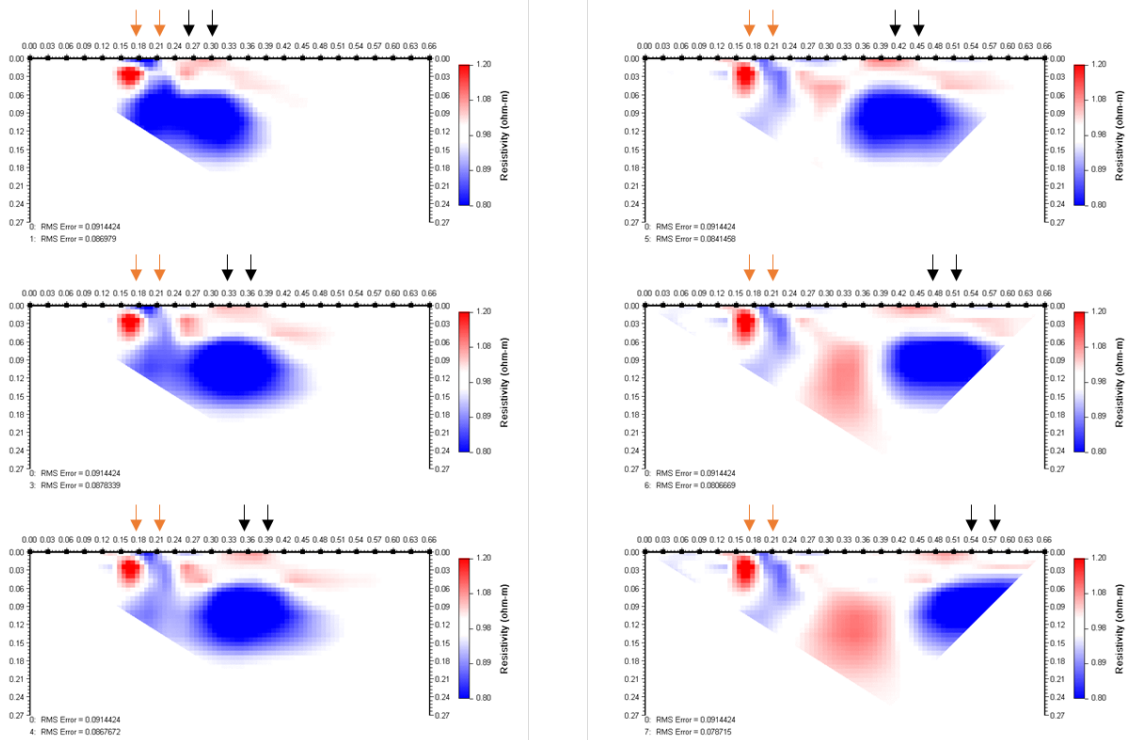
Figure E-7. Metal vertical pipe included in the tank experiment. Anomaly presented as a very conductive anomaly (0.2-2 ohm·m). Orange arrow indicates location of the metal pipe.

Figure E-8. Set up for the vertical metal pipe and moving conductive target experiment.

Figure E-9. Ratio images of conductive target moving further from a vertical pipe. Orange arrows indicate the position of the static vertical pipe. Black arrows indicate position of the moving conductive target during the data collection.

Conductive heater

Figure E-10. Set up for conductive heater experiment.

Tests with a conductive heater was performed. The set up for this experiment is shown in Figure E-10. The tank average temperature in image t0 is T_0=20.9°C, where T_x is temperature at time "x". Ratio images of the heating experiment are shown in Figure E-11. As observed, the temperature changes create conductive anomalies that starts in the center of the image where the heater is located and slowly heats the surface of the water table, spreading downwards after.
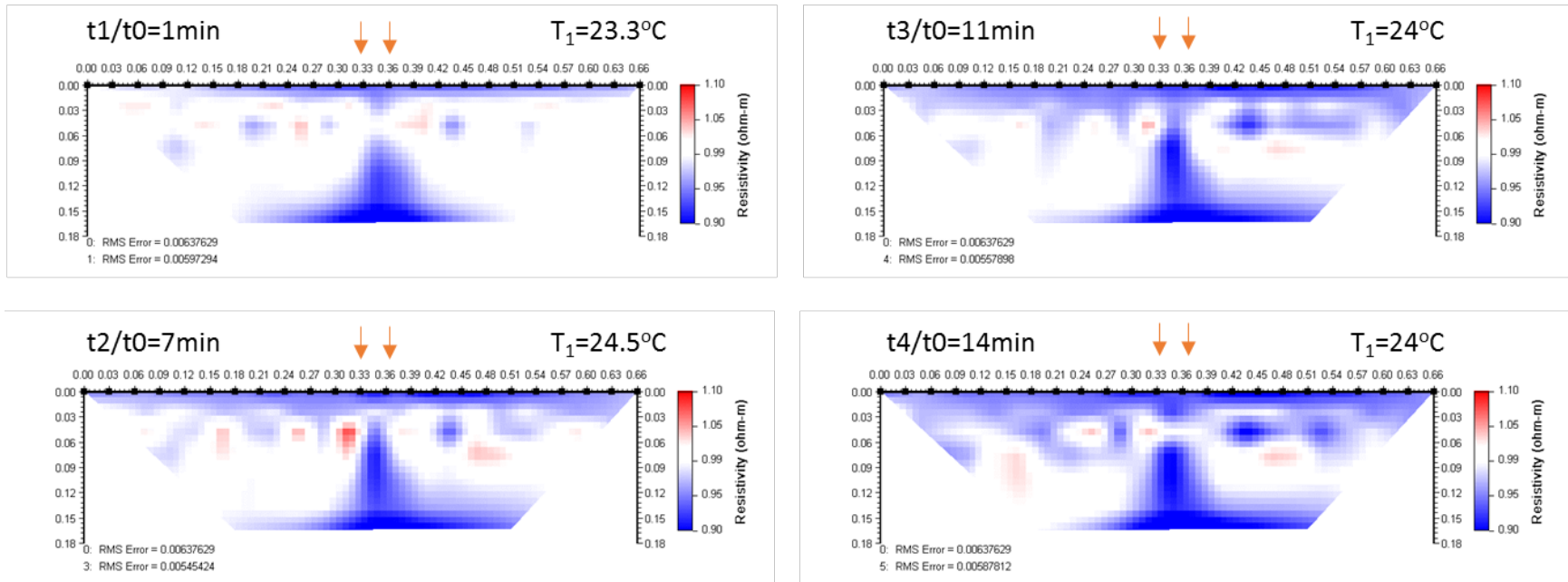
Figure E-11. Conductive heating experiment. Images taken at 1 min, 7 min, 11 min and 14 min after heater was turned on. Average temperatures are shown. Initial temperature was 20.9°C. Orange arrows indicate location of the heater.

Heater in a sand bucket with a horizontal pipe

To try to contain the heat and simulate in more real conditions the heat transfer in the subsurface, a sandbox was included in the experiment, containing the conductive heater inside. This sandbox was enclosed with a textile to guarantee that the soil would not escape from the box into the water in the tank. Set up is shown in Figure E-12. Several experiments were conducted with the sandbox, however, the experiment shown here demonstrate the heating of the sandbox with a vertical metal pipe on top of it, trying to simulate a STAR IP.
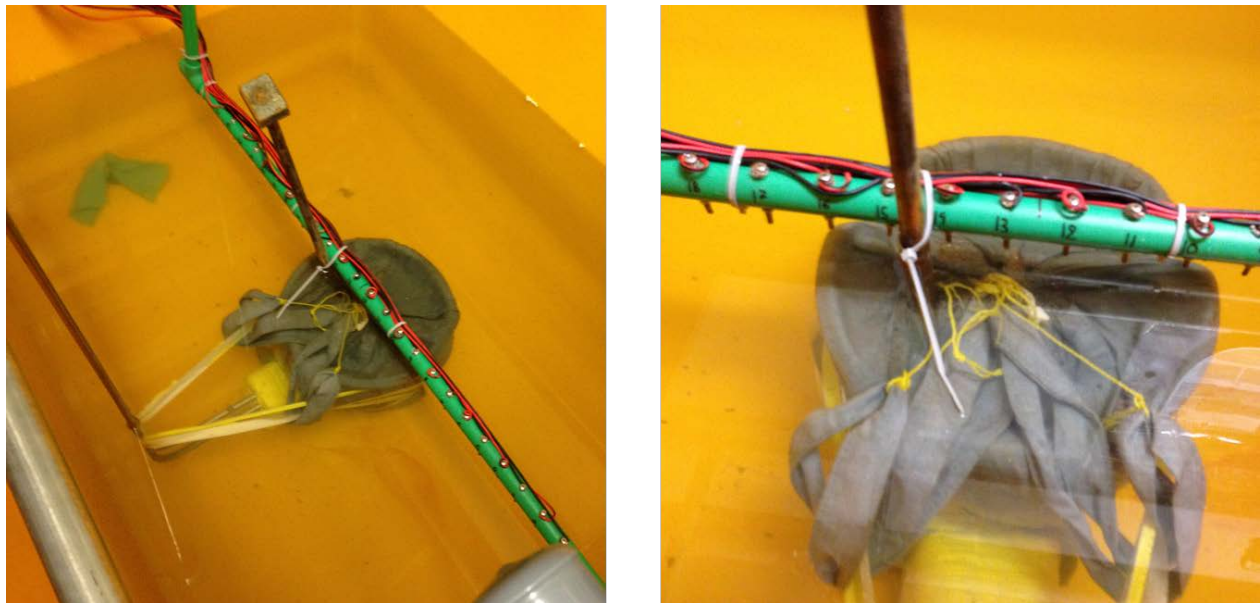
Figure E-12. Set up of heater inside the sandbox covered in textile. The vertical metal pipe is inserted inside the sandbox.

Ratio images from this experiment is shown in Figure E-13. A comparative pattern can be seen in this experiment compared to previous ones (Figure E-11), where temperature changes occur mainly around the heater and move upwards. However, it can be observed that the heating is much more focused within the sandbox. It is also possible to notice that the metal pipe seems to increase conductivity when heated first.

Small and strong resistive anomalies are seen in the image, located on top of the sandbox. At first, they were thought to be inversion artifacts, however, when observing the textile covering the sandbox, it was noted that bubbles were being formed, most likely because the sand was not

compacted enough, generating bubbles as water replaced the pores. These bubbles were trapped between the textile and the sandbox. Experiments conducted were images were taken before and after bubbles scape from the textile, as well as experiments with the textile opened confirmed this analysis (not shown here).
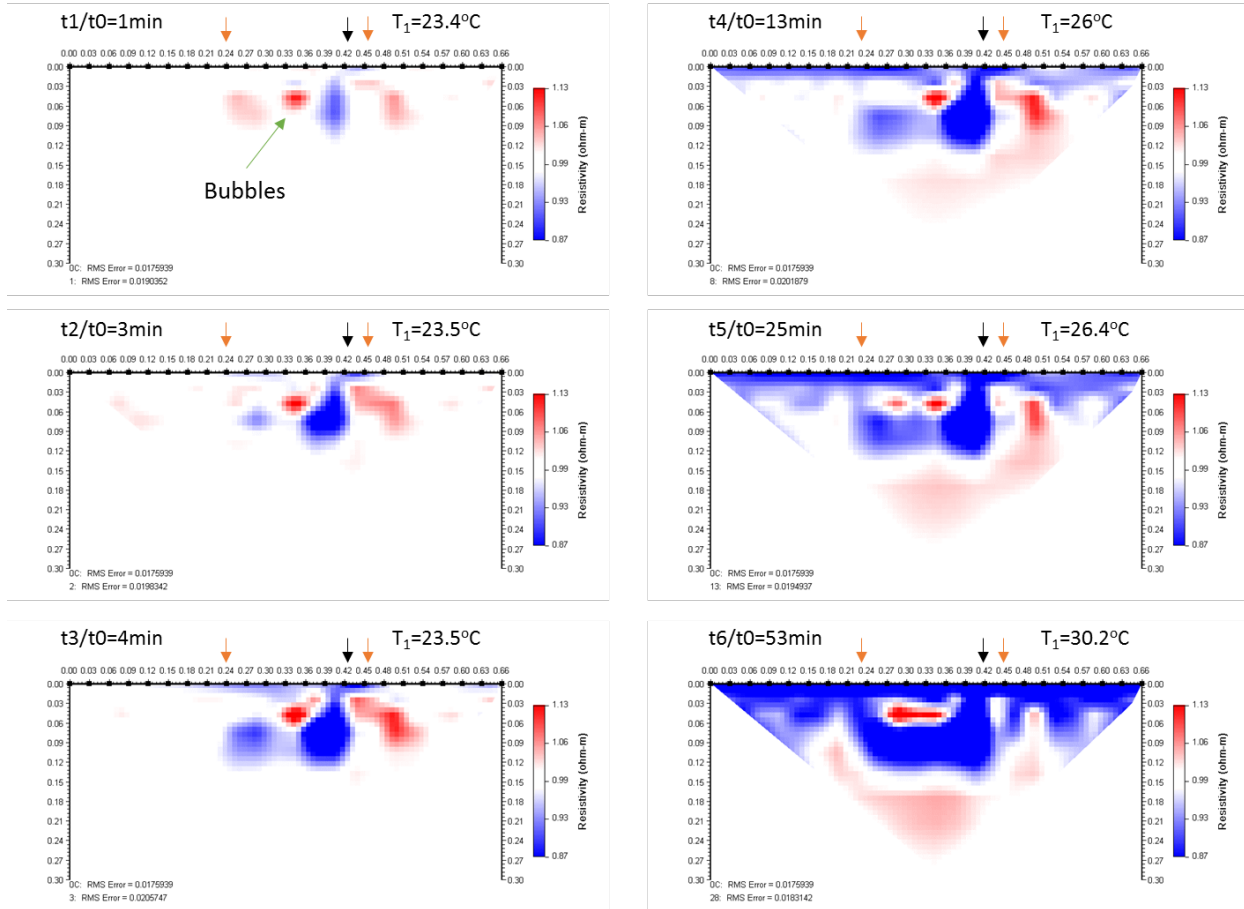

Figure E-13. Conductive heating experiment using a sandbox and a vertical metal pipe. Images taken at 1 min, 3 min, 4 min, 13 min, 25 min, and 53 min after heater was turned on. Average temperatures are shown. Initial temperature was 23.3°C. Orange arrows indicate location of the sandbox, with the heater in the middle. Black arrow indicates the vertical pipe location.

APPENDIX F. Sensitivity analysis

Model block sensitivity of a resistivity survey is measured by the amount of data collected contained in each model block of the inversion. It is well known that shallow surface resistivity has more sensitivity than deeper, because the sensitivity function (Jacobian) has more values in the shallow region (Loke, 2013). The model block sensitivity for each of the lines in the shallow and deep cell were calculated based on a homogenous subsurface (Figure F-1-4). The block sensitivity was calculates using RESDINV (Loke, 2013).

Figures F-1-2 shows that relatively high model sensitivity for the shallow cell goes down to approximately 3 mbgs, while Figure F-3-4, shows the analysis for the deep cell, and the relatively high model sensitivity goes down to approximately 6 mbgs.

References

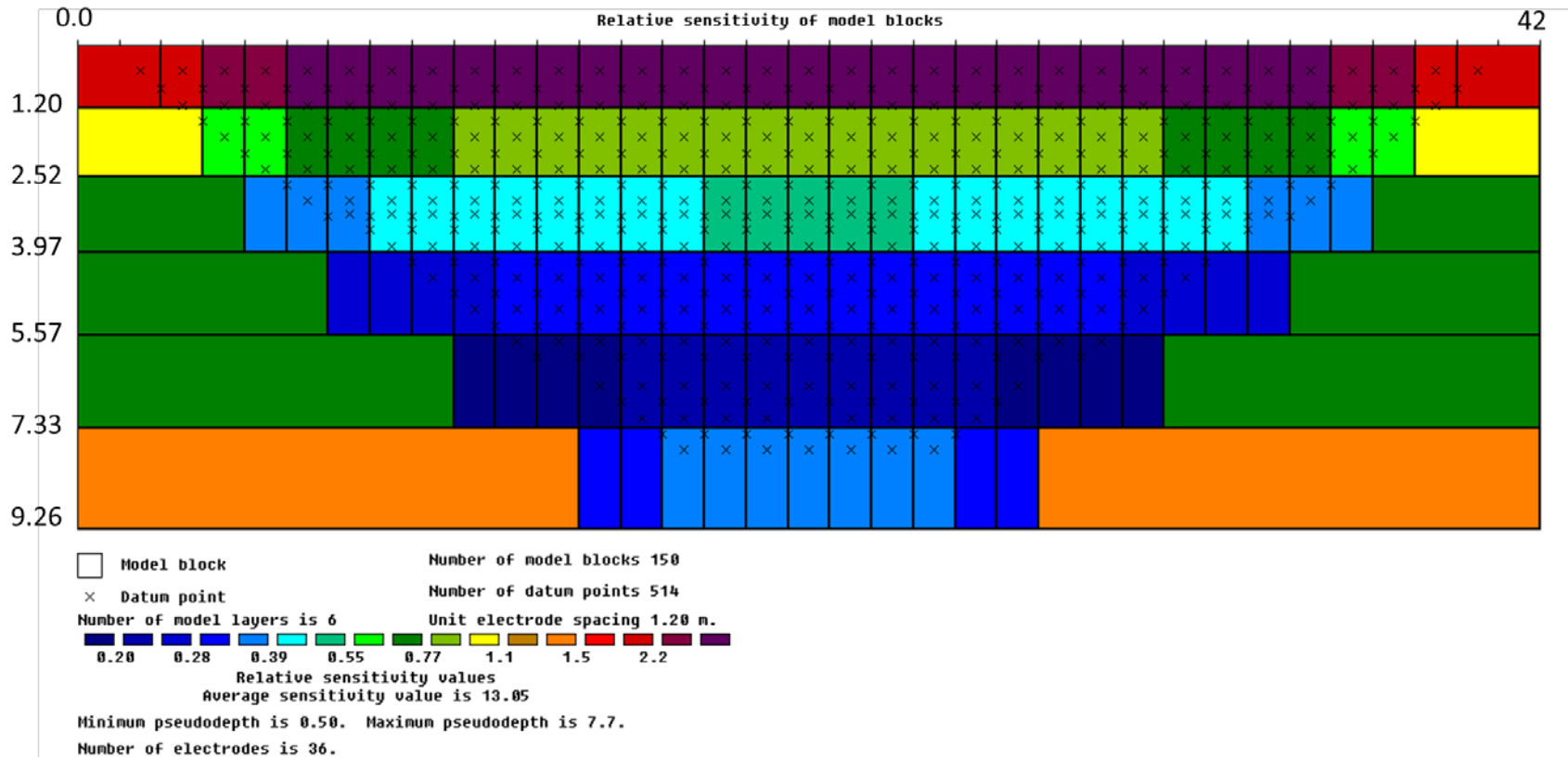Loke, M. H. (2013). Tutorial: 2-D and 3-D electrical imaging surveys.

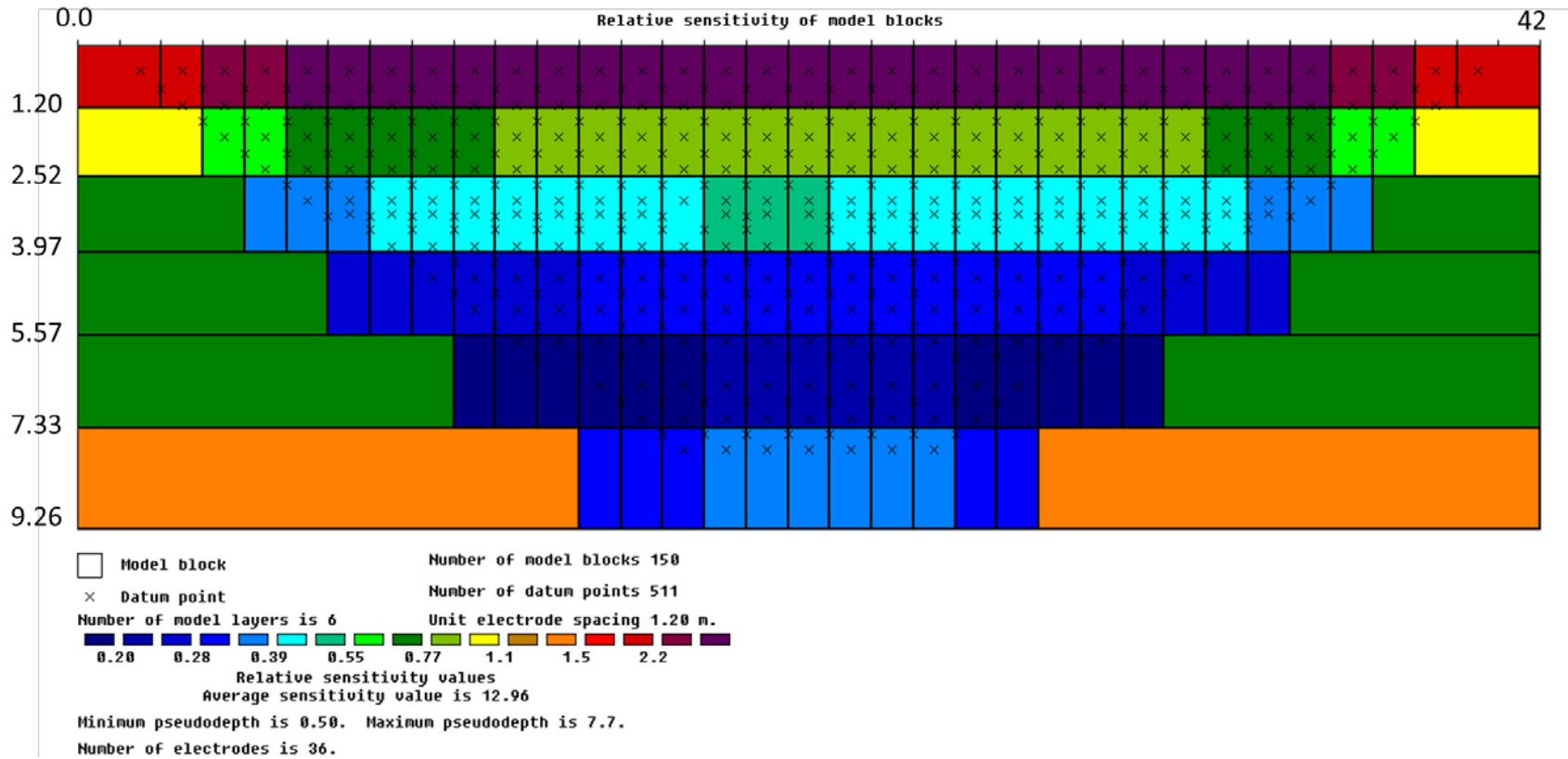**Figure F-1.** Model block sensitivity analysis for a homogenous earth for the deep cell line S-N.

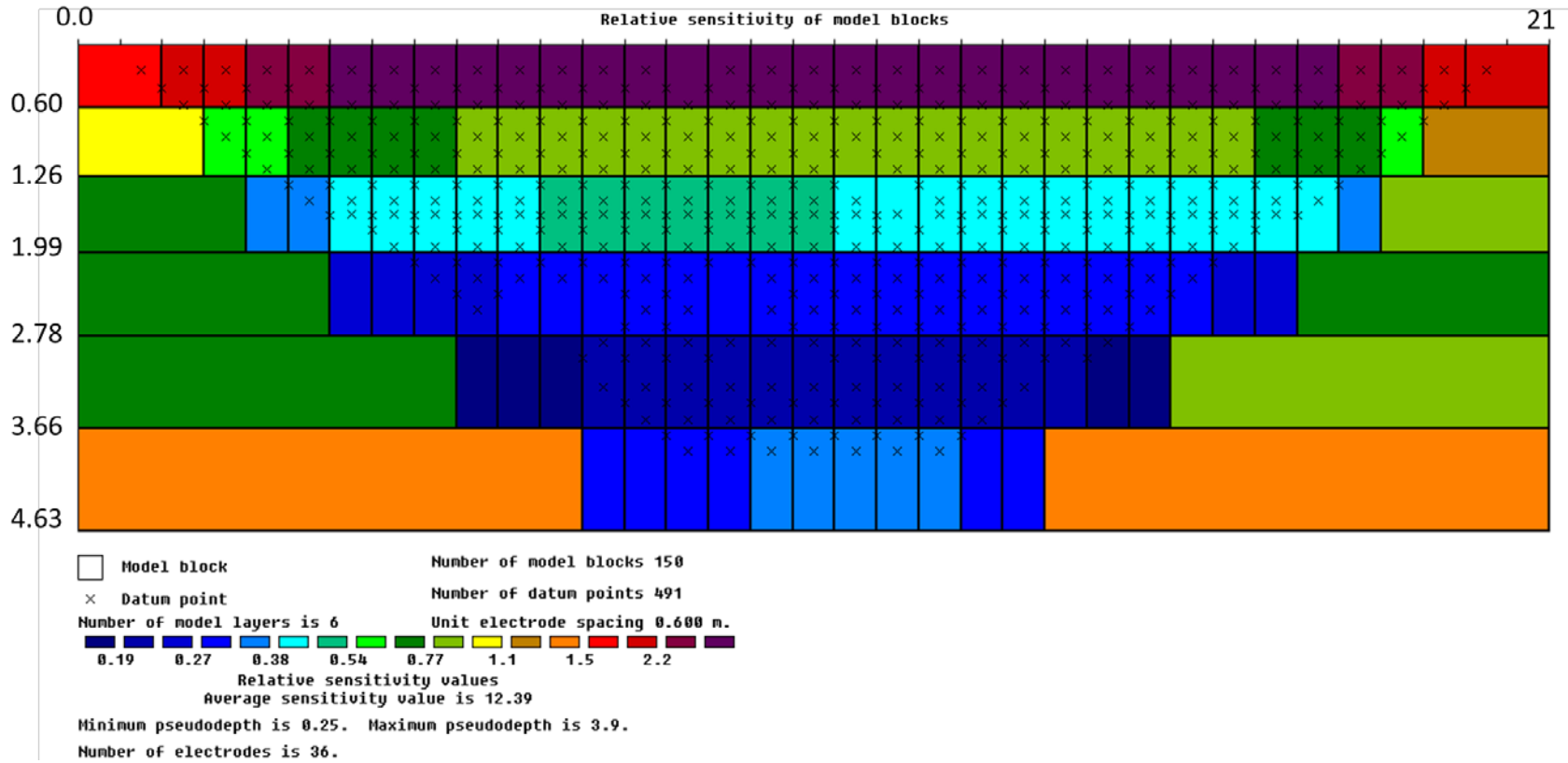**Figure F-2.** Model block sensitivity analysis for a homogenous earth for the deep cell line W-E.

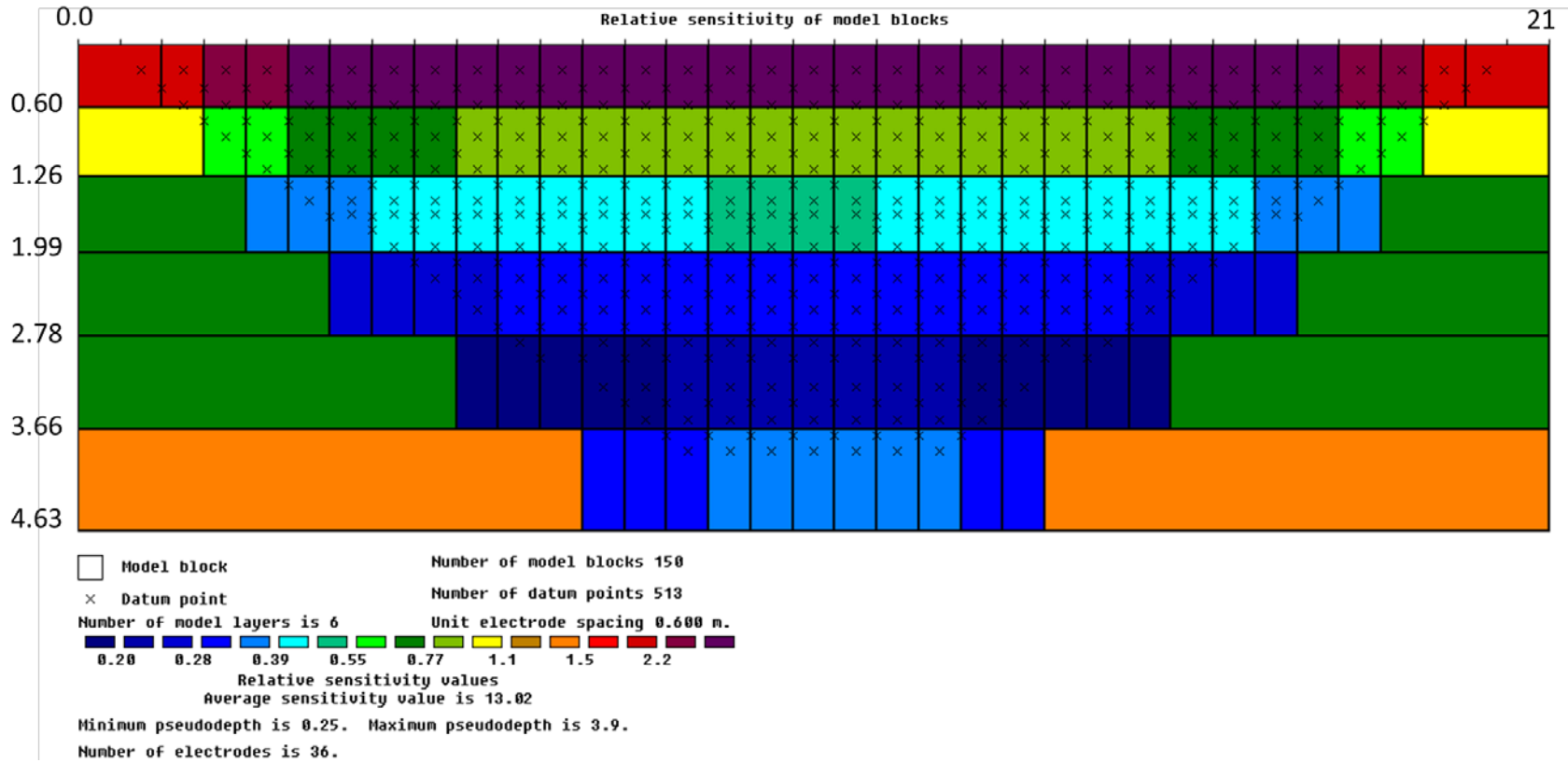**Figure F-3.** Model block sensitivity analysis for a homogenous earth for the shallow cell line S-N.

Figure F-4. Model block sensitivity analysis for a homogenous earth for the shallow cell line W-E.

APPENDIX G. Focused analysis of shallow cell and layered average resistivity values for the deep

This appendix shows more examples of the node analysis performed for the shallow cell, mostly focusing on Line W-E not shown during Chapter 3 and examples of locations were the "valley" approach was not shown (IP1 for both lines). Afterwards, it will show the analysis performed for the deep cell on the layered resistivity analysis, for both lines, in the Fill, Meadow Mat, Alluvium and overall resistivity.

Shallow focused analysis extra graphs

Figure G-1a represents line S-N background image without interpolation showing discrete nodes for the resistivity analysis in time. Figure G-1i, ii show five graphs representing the analysis for IP4 and IP5, as well as IP1. As observed in Chapter 3, Figure G-1i contains the "valley" approach, however, Figure G-1ii does not contain the "valley" approach described in Chapter 3.

The results of this analysis and further description can be observed in Chapter 3, section 3.4.1.2 (Focused analysis of the shallow cell) and Figure 3-10.
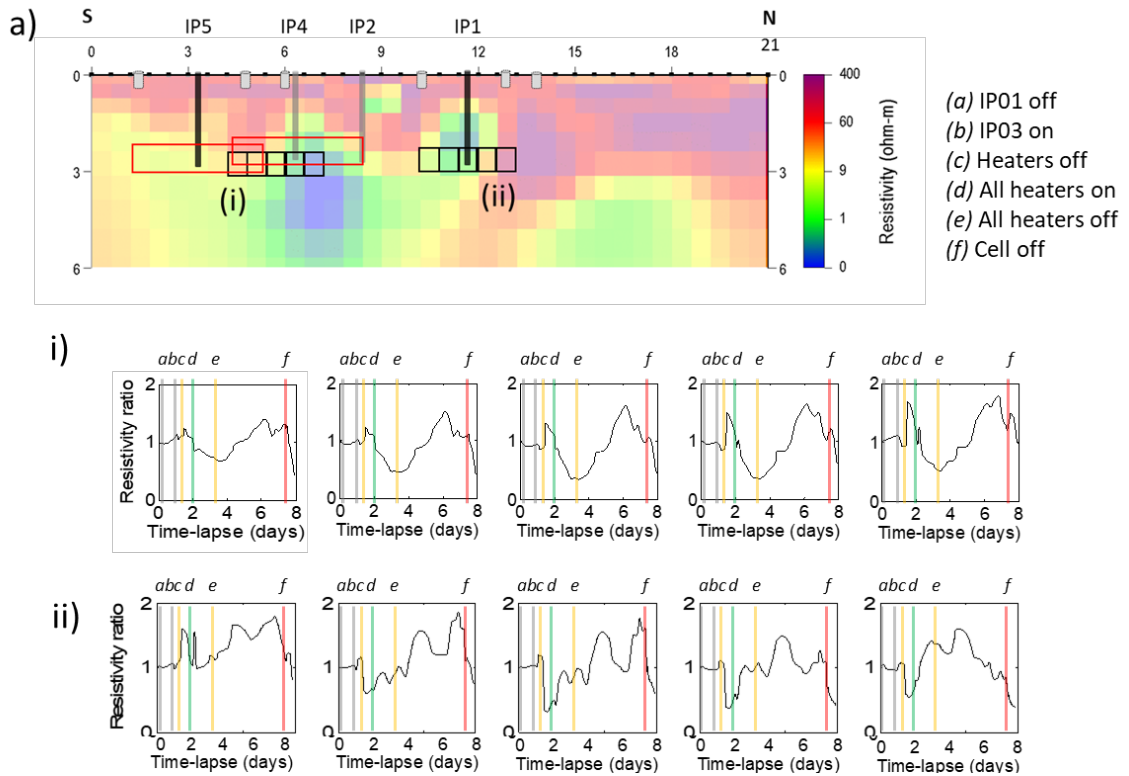
Figure G-1. More examples of focused analysis: resistivity over time in expected smouldering zone of IP4 and IP5 (i) and IP1 (ii). a) Discrete values for each node in the resistivity inversions of S-N background image. Red rectangles are the expected reaction zones for IP4 and IP5. Black squares correspond to the location of each graph in i) and ii). i) and ii) are ratio resistivity values in time-lapse for nodes shown in a) compared to values in t0. *a)-f)* are time-steps as shown in legend and Table 3-1.

Figure G-2a represents line W-E background image without interpolation. Figure G-1i shows five graphs near IP3, however, only the third graph shows the "valley" approach. Figure G-2ii shows five graphs surround IP1, all of them does not contain the "valley" approach.
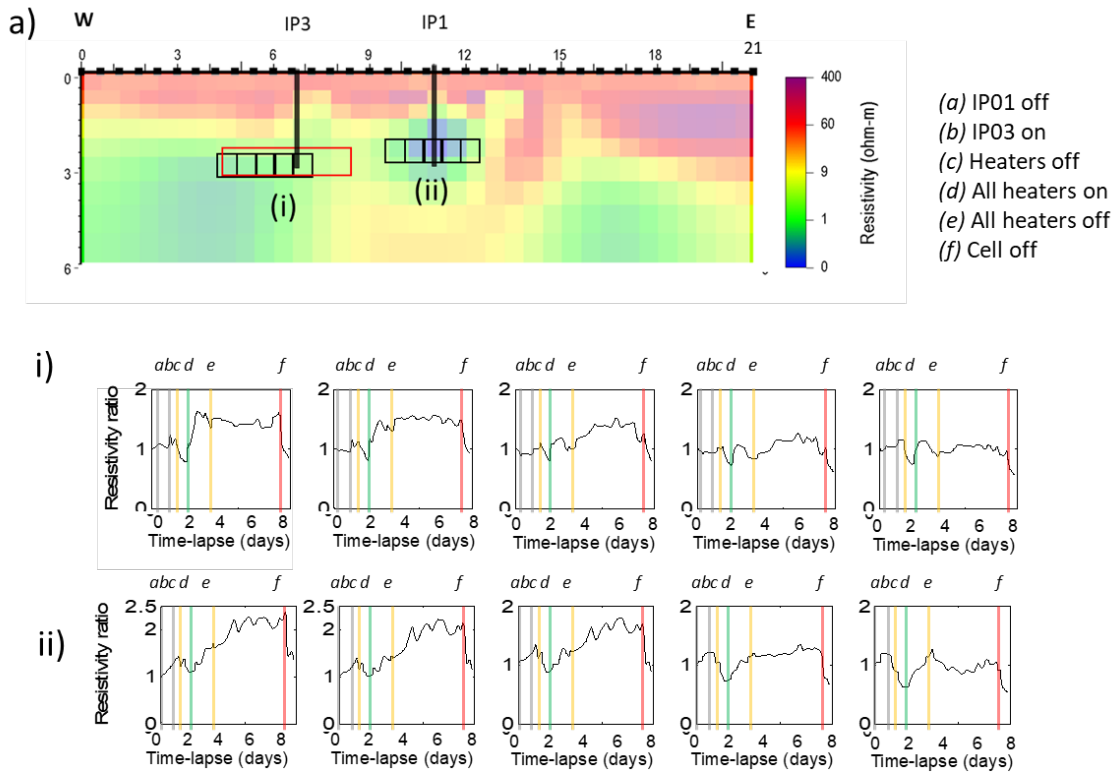
Figure G-2. More examples of focused analysis: resistivity over time in expected smouldering zone of IP3 (i) and IP1 (ii). a) Discrete values for each node in the resistivity inversions of W-E background image. Red rectangles are the expected reaction zones for IP3. Black squares correspond to the location of each graph in i) and ii). i) and ii) are ratio resistivity values in time-lapse for nodes shown in a) compared to values in t0. *a)-f)* are time-steps as shown in legend and Table 3-1.

Deep cell average resistivity values for each layer

To confirm the analysis observed for the deep cell where it was identified that the gases were trapped below the Meadow Mat, an average resistivity for the three different layers in the subsurface was conducted: (i) all, where the entire image average resistivity was calculated (from 0 to 12 m), (ii) Fill layer, obtaining the average resistivity from the images from 0 to 3.6 mbgs, (iii) Meadow Mat (MM) layer (from 3.6 to 7.65 m), and (iv) Alluvium layer (from 7.65 to 11.1 m). The results for line S-N and line W-E are shown in Figure G-3 and G-4, respectively.
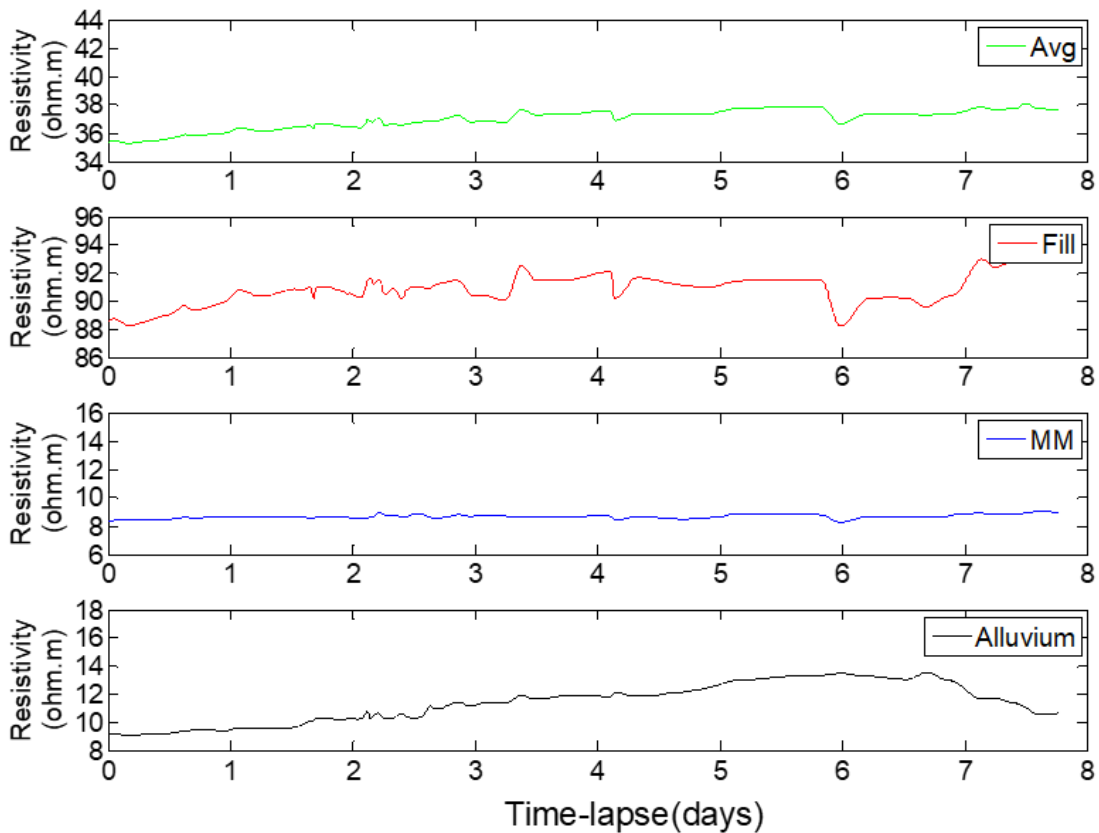
Figure G-3. Average resistivity for Line S-N in different layers in the subsurface for the deep treatment unit: all (entire image: from 0 to 12 m), Fill layer (from 0 to 3.6 m), Meadow Mat (MM) layer (from 3.6 to 7.65 m), Alluvium layer (from 7.65 to 11.1 m).

The Figures G-3 and G-4 show that most of the changes in resistivity is concentrated in the Fill and the Alluvium, with the MM layer keeping a steady resistivity. The increase in resistivity in the Fill layer is possibly due to the VEPs collecting the smouldering gases. The MM is expected to have little changes as it is an intermediate clayed layer, where possible little gas in passing through. The most increases in resistivity is seen in the Alluvium, which was expected, not only because the resistivity ratios show a general increase in resistivity in the Alluvium, but also because it is where the treatment is located. The changes in the Alluvium begins after CO_2 data shows an increase, showing a good correlation. The resolution of the deep treatment unit is insufficient for the same kind of focused analysis as performed at the shallow treatment unit.
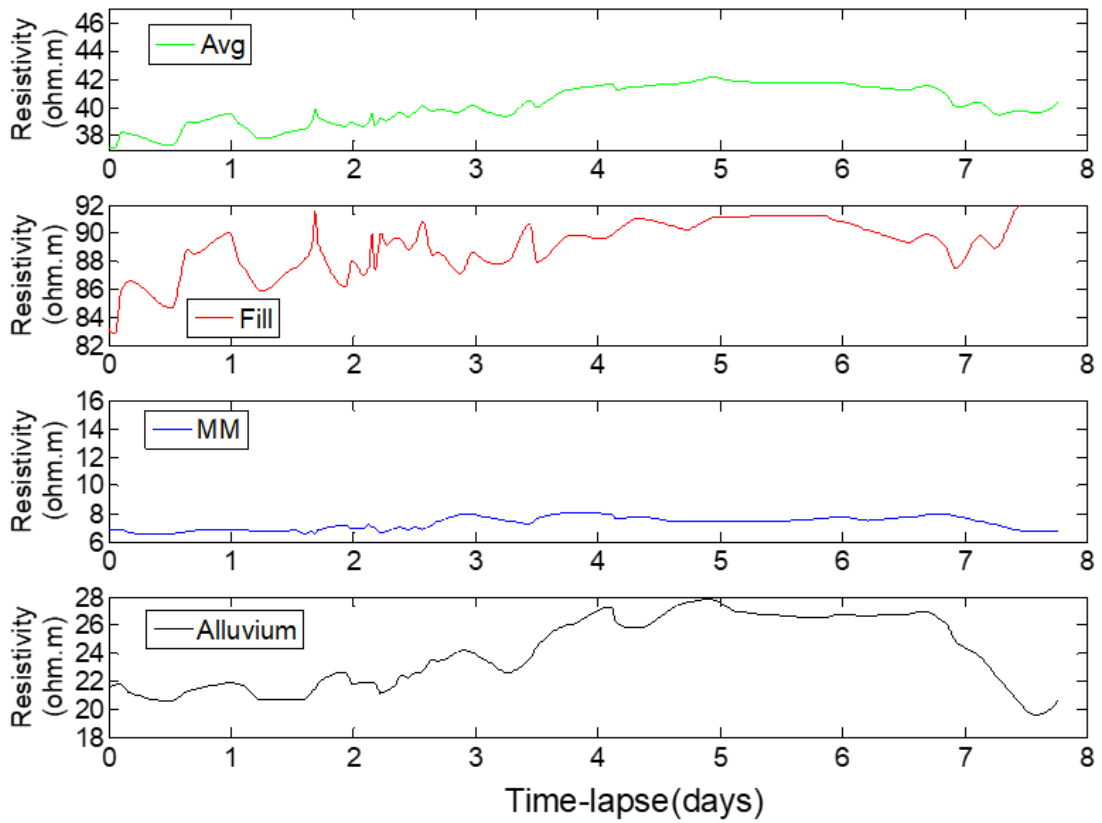
Figure G-4. Average resistivity for Line W-E in different layers in the subsurface for the deep treatment unit: all (entire image: from 0 to 12 m), Fill layer (from 0 to 3.6 m), Meadow Mat (MM) layer (from 3.6 to 7.65 m), Alluvium layer (from 7.65 to 11.1 m).

APPENDIX H. Re-infiltration images for shallow and deep cell

The re-infiltration analysis was conducted to evaluate the hypothesis that the water is re-infiltrating the treated soil after treatment. Ratio images for both shallow and deep cell were generated between the end of treatment (representing likely maximum extent of the dry treatment zones, volume of air injection and volume of combustion gases generated) and one day after treatment shutdown and air pressure release at the IPs. The figures below (Figure H-1 to H4) shows the resulting ratio images for lines S-N and W-E in the shallow and the deep cell. And shows all the images that were taken in the period after system shutdown. The images show an overall decrease in resistivity in the expected/focused treated region and where we expected to have trapped gases for the shallow cell and in the regions below the MM where it was expected that combustion gases were trapped. For the deep cell, these images suggest that re-infiltration dominated in the Alluvium where water saturation was lowest and where the resistivity increase during treatment was greatest

Shallow cell re-infiltration ratio images

The images for line S-N (Figure H-1) and W-E (Figure H-2) are shown below. They represent all the images collected between the between end of treatment for the shallow cell (last image before cell shutdown – August 21, 2016 at 7:25PM) and last image taken at the location (August 22, 2016 at 07:00AM).

Deep cell re-infiltration ratio images

The images for line S-N (Figure H-3) and W-E (Figure H-4) are shown below. They represent all the images collected between the between end of treatment for the deep cell (last image before cell shutdown – September 02, 2016 at 10:20AM) and last image taken at the location (September 03, 2016 at 09:40AM).
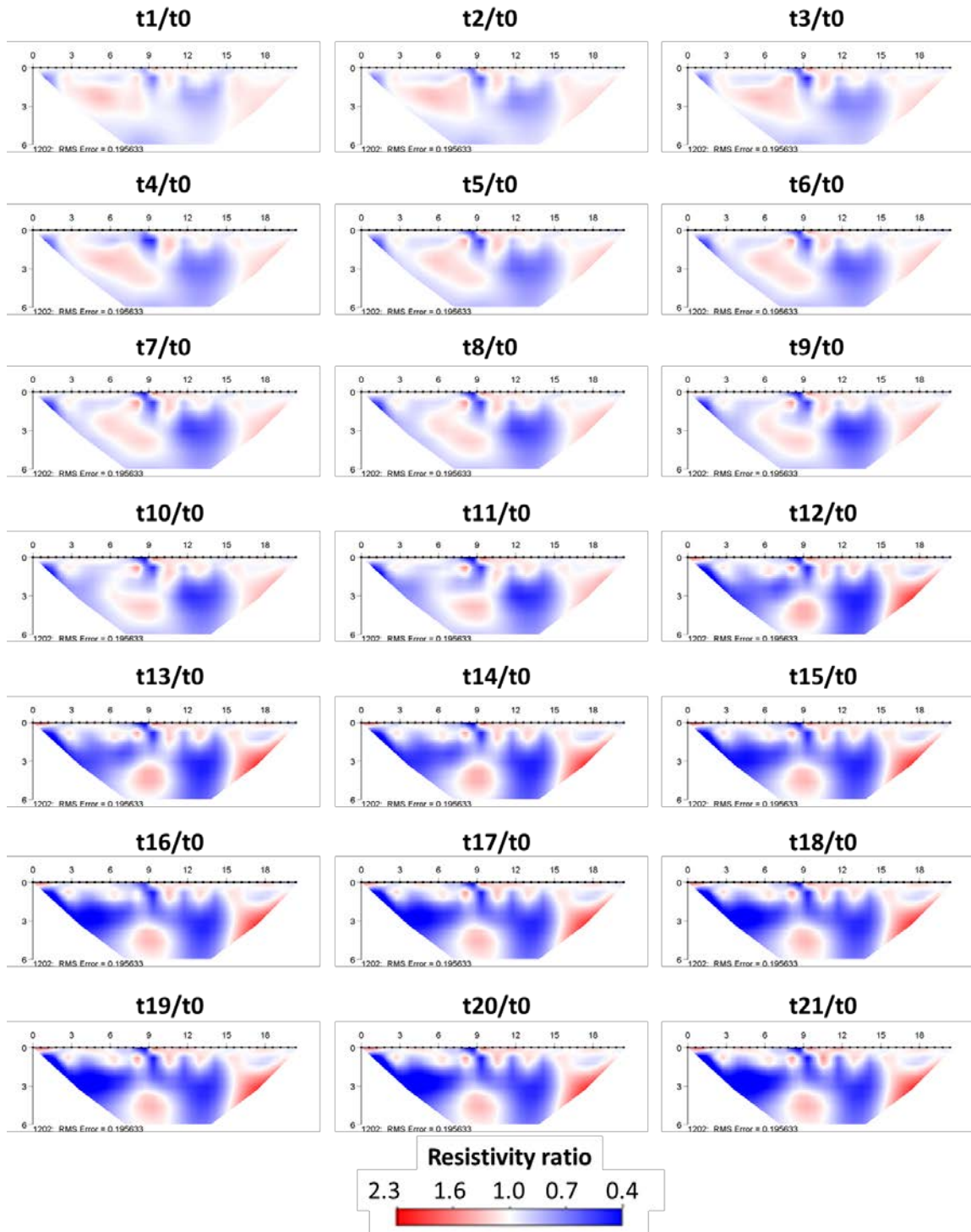
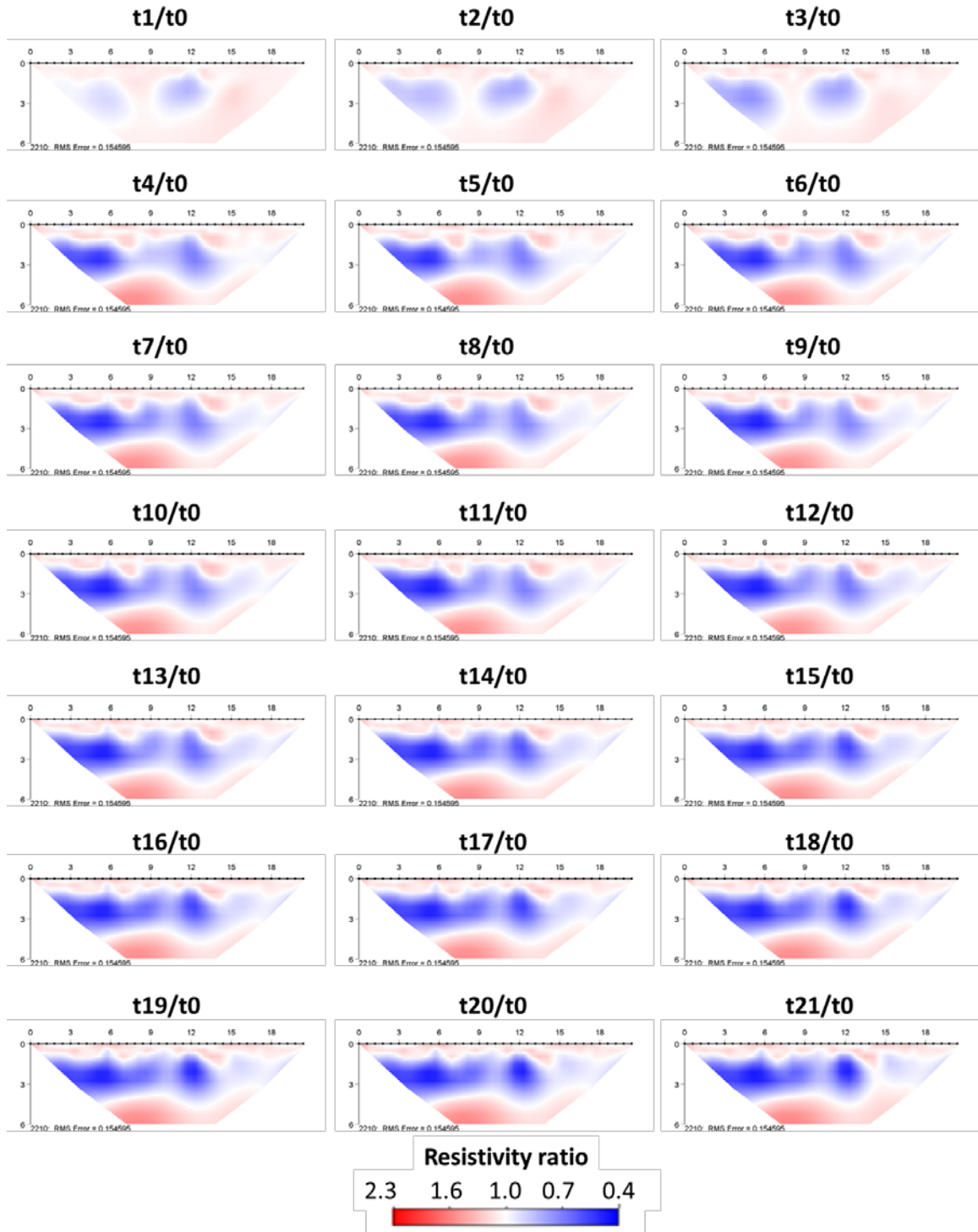**Figure H-1.** Shallow cell S-N groundwater re-infiltration analysis.

Figure H-2. Shallow cell W-E groundwater re-infiltration analysis.
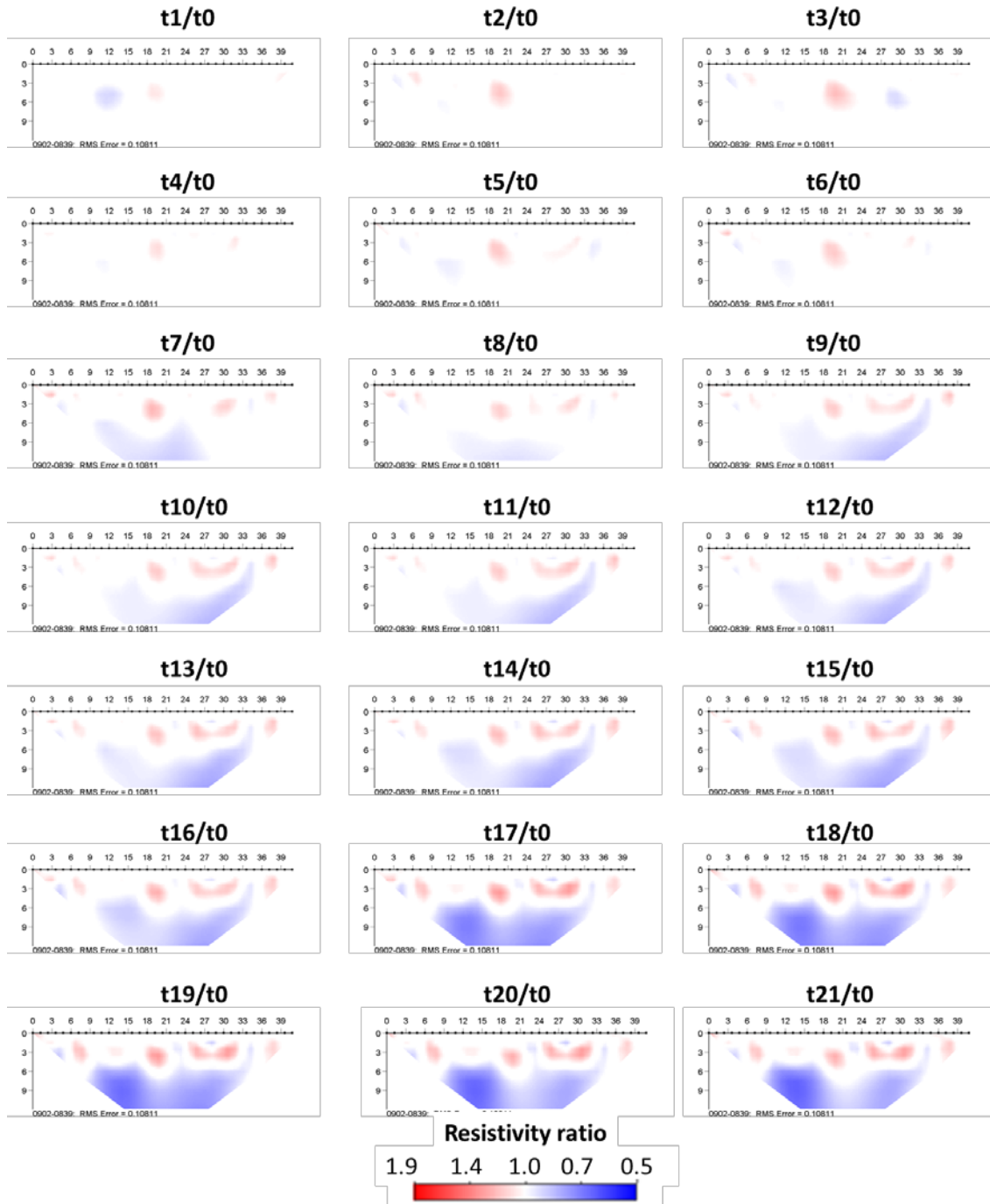
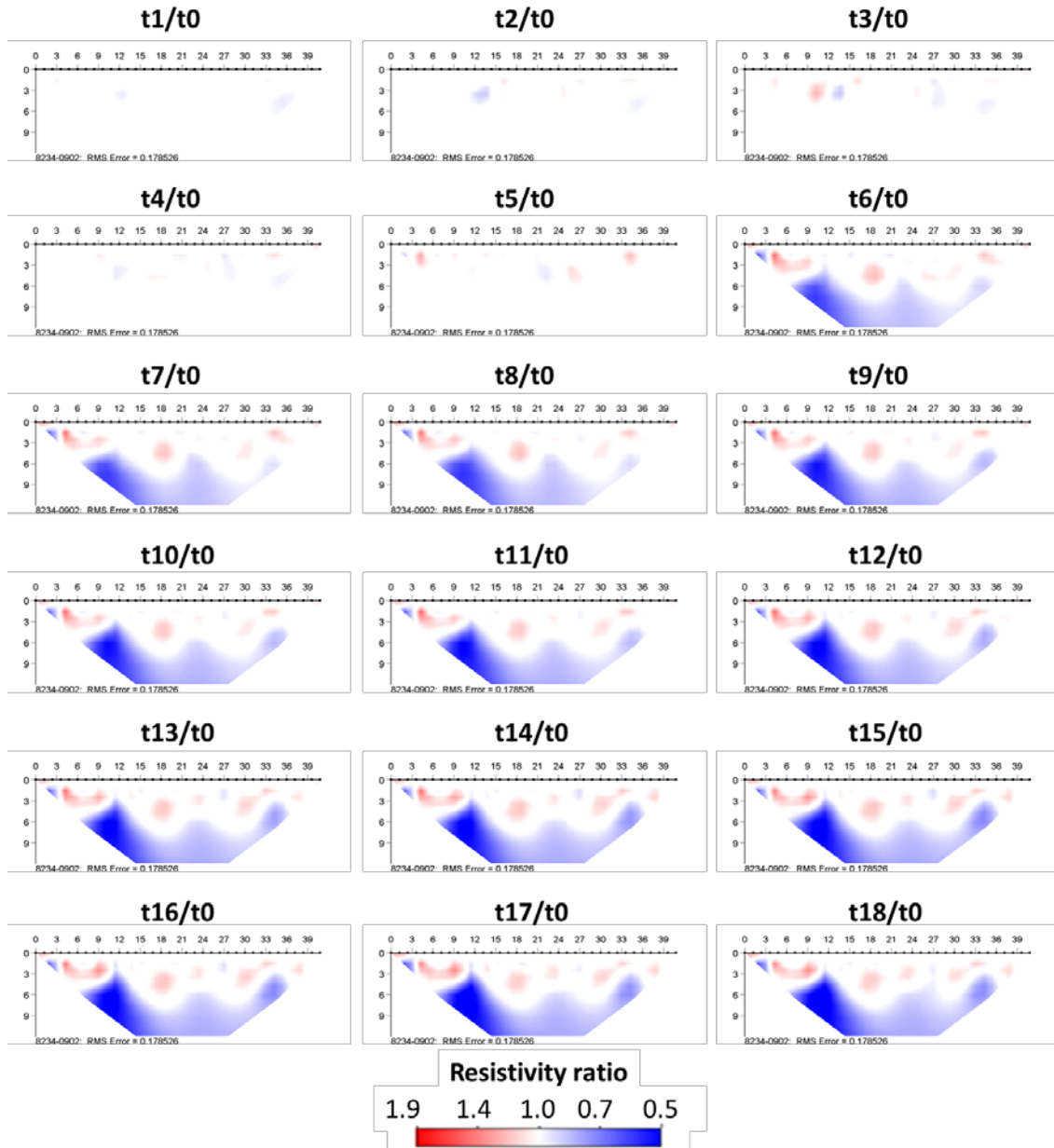**Figure H-3.** Deep cell S-N groundwater re-infiltration analysis.

Figure H-4. Deep cell W-E groundwater re-infiltration analysis.

Curriculum Vitae

Name: Lais Muchatte Trento

Post-secondary Education and Degrees:
Universidade Estadual Paulista (UNESP)
Sorocaba, Sao Paulo, Brazil
2008-2012 B. E. Sc.

The University of Western Ontario
London, Ontario, Canada
2015-2017 M. E. Sc.

Honours and Awards:
John Booker Award
2016

Natural Sciences Engineering Research Council of Canada
Industrial
Postgraduate Scholarship
(2015-2017)

Related Work Experience
Teaching Assistant
The University of Western Ontario
2015-2017